ISSN: 2331-1959 Volume 8, Number 3, July 2020

Scientific Research Publishing

Archaeological Discovery

ISSN: 2331-1959
9 772331 195007 03

https://www.scirp.org/journal/ad

Journal Editorial Board

ISSN Print: 2331-1959 ISSN Online: 2331-1967
https://www.scirp.org/journal/ad

Archaeological Discovery, 2020, 8, 199-294
https://www.scirp.org/journal/ad
ISSN Online: 2331-1967
ISSN Print: 2331-1959

Table of Contents

Volume 8 Number 3 July 2020

Archaeological Discovery (AD)
Journal Information

SUBSCRIPTIONS

The *Archaeological Discovery* (Online at Scientific Research Publishing, https://www.scirp.org/) is published quarterly by Scientific Research Publishing, Inc., USA.

Subscription rates:
Print: $39 per issue.
To subscribe, please contact Journals Subscriptions Department, E-mail: sub@scirp.org

SERVICES

Advertisements
Advertisement Sales Department, E-mail: service@scirp.org

Reprints (minimum quantity 100 copies)
Reprints Co-ordinator, Scientific Research Publishing, Inc., USA.
E-mail: sub@scirp.org

COPYRIGHT

PRODUCTION INFORMATION

For manuscripts that have been accepted for publication, please contact:
E-mail: ad@scirp.org

Archaeological Discovery, 2020, 8, 199-206
https://www.scirp.org/journal/ad
ISSN Online: 2331-1967
ISSN Print: 2331-1959

Archaeometallurgical Analysis of Bronze Artifacts: A Magnetometer Approach

Lucas Braddock Chen

Foundation for the Advancement of Anthropology & History, Menlo Park, CA, USA
Email: Braddock9955@gmail.com

How to cite this paper: Chen, L. B. (2020). Archaeometallurgical Analysis of Bronze Artifacts: A Magnetometer Approach. *Archaeological Discovery, 8,* 199-206.
https://doi.org/10.4236/ad.2020.83011

Received: April 21, 2020
Accepted: May 12, 2020
Published: May 15, 2020

Abstract

Bronze has been utilized by human civilization for the past five millennia, and societies across the globe have mined, extracted, and purified copper and tin to create bronze alloys. Due to the different mineral composition of ores and the varying techniques involved with metal smelting, bronze artifacts from around the world often have very different chemical compositions. The determination of chemical composition is often invasive and expensive, and is usually conducted in laboratories. We previously developed an inexpensive and mobile test to identify metal alloys based on their magnetic signatures. We demonstrated that metals of different compositions would exhibit different electrical conductivity, and thus different magnetic field strengths when evoked by different levels of electric current. In this manuscript, we now detail the experiment protocol to produce evoked dynamic electromagnetic signals from bronze alloys, and the capture of signals with the smartphone magnetometer.

Keywords

Archaeometallurgy, Metallurgy, Bronze, Ancient, Magnetism, Magnetometer

1. Introduction

Copper was the first metal widely utilized across the ancient world. Its prevalence, shiny luster, and natural existence as native copper allowed this metal to be noticed and collected. Mesopotamian metalsmiths were able to cold hammer native copper into pins and awls around 6500 - 5500 BC (Gale et al., 1985). However, the supply of native copper was limited. Copper only became widely available after man learned to harvest copper through smelting ores, from which pure copper could be isolated after a series of heating and reduction-oxidation reactions using forced air and charcoal (Muhly, 1985). Copper, however, was soft and had limited durability as tools and weapons (Curry, 2020). In addition,

its high melting temperature of 1084-degrees Celsius also rendered the metal laborious to cast using a conventional open fire pit (Bennett, 2020). The development of bronze thus represented a major technological advance in 3300 BC when mankind discovered that the tin and copper alloy is stronger, more resistant to corrosion, and more malleable (Lopez, 2009; Raymond, 1984).

These ancient bronzewares, however, were often of very different chemical composition and properties, as they were smelted from distinct copper ores containing varying minerals, depending on the geology of the ore origin. In addition, copper is often composed of different molecules, such as oxides, carbonate, and sulphide compounds (Muhly, 1976). Copper oxides include cuprite Cu_2O and melaconite CuO; copper carbonate includes malachite $Cu_2(OH)_2CO_3$ and azurite $Cu_3(OH)_2(CO3)_2$; and copper sulfide includes chalcocite Cu_2S and covellite CuS. Copper isolated from these compounds have different levels of purity, and the associated minerals were invariably also extracted during the smelting process: this resulted in unique chemical signatures for the smelted copper. Similarly, tin extracted from ores were also of unpredictable purity levels, containing minerals based on the ore geology. Consequently, when bronze was created, the mixture of copper and tin invariably created a final alloy of unique chemical signatures.

As a result, the identification and classification of ancient bronze artifacts can be challenging, as artifacts of similar shapes and appearance may nevertheless consist of completely different chemical compositions, and thus, chemical signatures. It nevertheless presents an opportunity to uniquely identify each bronze artifact and possibly understand its history and origin. The study of archaeometallurgy has employed various techniques in an attempt to better characterize bronzeware. Several different noninvasive tests have been developed. For example, a streak test can assess metal hardness by scratching the surface, but this is an unreliable method to identify metal content. Energy spectrometry projects an X-ray beam to the metal's surface and examines the emitted secondary x-ray signal, which can help provide characteristics of the metal. However, this technique can only detect the metal on the surface and is not usable if the antique is painted or plated with a different metal (Raymond, 1984).

Some invasive methods have also been utilized. A spot analysis dissolves a small piece of metal in a chemical mix to determine metal composition, but the process is destructive and can only sample a small portion of the metal artifact. Neutron activation analysis places a metal sample in a nuclear reactor and examines the emitted gamma-ray from bombarding neutron beams. This metal identification process, however, is expensive, destructive, and can only analyze a small sample. Moreover, it has been shown that copper and tin often do not mix uniformly as they have different melting points; thus, bronze artifacts have different metal compositions throughout their structure (Logan, 2007). Consequently, taking a small sample of the bronze for atomic or chemical analysis may provide misleading information (Scott, 1991). Taking larger or more samples, while providing more data, would severely damage or destroy the valuable artifact.

None of the above methods of bronze identification are ideal, and some of the techniques require expensive laboratories. As a result, these methods are not readily available nor practical for archaeologists examining an excavated bronze artifact at a dig site. We now report a noninvasive and mobile method of rapid bronze analysis using the magnetometer on a smartphone to determine dynamic magnetic property.

We previously patented a rapid method of steel blade identification based on magnetic properties (Chen, 2019). Steel blades of different grades and qualities are constructed of different ratios of iron, nickel, carbon, and other elements; thus, each blade grade has its own electric conductivity pattern. Since a magnetic field is generated while the blade conducts electricity, each blade grade will have its own induced magnetic field property. Moreover, since magnetic properties can change at different levels of electrical current, each blade class will demonstrate a unique magnetic profile at different levels of electricity (dynamic magnetic property). By measuring the dynamic magnetic profile at different electric conduction levels, one can readily identify the composition of the blade.

Furthermore, we previously reported that the magnetic field can be readily detected using a smartphone (Chen, 2019). All modern smartphones possess a magnetometer as part of their internal compass (Baldini, 2017; Odenwald, 2019), and these magnetometers can be utilized to capture the blade's magnetic profile—both the static magnetic profile (before electricity is applied) and the dynamic profile (determined at different levels of electricity; Arribas, 2015). The protocol of identifying steel composition using a smartphone magnetometer was recently published (Chen, 2020a). In addition, we showed that the dynamic magnetic signatures corresponded to the chemical composition of the steel blade and its Vickers microhardness (Vickers Hardness Test, 2020; Chen, 2020b).

We recently patented a method of identifying bronze artifacts using a similar technology (Chen, 2020c). As stated above, bronzeware from each region and civilization is composed of different levels of copper and tin since the local metal ores are different. Since copper and tin have different electrical conductivity (with tin only having 15% of copper's electrical conductivity; Metal Supermarkets, 2015), bronzeware of different copper-tin ratios will have different electrical conductivities, and thus, different dynamic electromagnetic profiles. In addition, as much of ancient bronzeware invariably contains various combinations of arsenic, lead, phosphorus, aluminum, manganese and silicon from local ores, bronze made in different parts of the world have very different magnetic profiles. In this article we now present the experimental protocol necessary for obtaining electromagnetic signatures of bronze artifacts using a smartphone magnetometer.

2. Material and Methods

A smartphone can be used to scan bronzeware and detect the dynamic magnetic profile at different levels of electric current to construct its unique magnetic signature. The protocol for magnetic signature extraction requires the following

parts: a test material holder, a smartphone with a magnetometer, a stabilizing platform for the smartphone, an app for measuring electromagnetic profiles, a source of electricity, and wires to conduct electricity from the electric source to the test material.

1) *Test material platform*: A holder is used to stabilize the test material during the test. The holder needs to be constructed of electrical insulating material so as not to interfere with the electromagnetic measurement during the test. Small artifacts can be held by the Everbilt Small 2-7/8 in. Rubber Grip Wall Mount Holder (Home Depot, Atlanta, GA). As for more delicate materials, the Web clamp is used (DeWalt, Baltimore, MD). Heavy objects would be better stabilized by the robust plastics jaw clamp (Home Depot, Atlanta, GA). For the current study, the Multifunctional Welding LED Magnifier Helping Hand Soldering Iron Stand (Amazon, Seattle, WA) was used (**Figure 1**).

2) *Smartphone with magnetometer and software*: Most smartphones now contain a magnetometer as a part of their internal compass. An iPhone XS Max, Apple (Cupertino, CA) running iOS 12.4 was used in the current study. Magnetscape 2.0 (Toon, Osaka, Japan) was used as the magnetometer software to record electromagnetic signatures.

3) *Smartphone stabilizer*: A rubber-insulated holder was used to hold and stabilize the smartphone during the study. For the iPhone used in the study, Aduro Solid-Grip Phone Holder for Desk—Adjustable Universal Gooseneck Smartphone Stand, with Durable Rubberized Mount, was used as the stabilizer (Amazon, Seattle, WA).

4) *Electric source*: In order to obtain magnetic signatures at different energy levels, a variable energy source was used: Tekpower TP3016M Portable Handheld Variable DC Power Supply with USB Port, 0.3 V - 12 V @ 0 - 3.75 A or 0.3 V - 30 V @ 1.6 A with VC and CC Control, Upgraded TP3005D, HY3005 (Tekpower, Montclair, CA; **Figure 2(a)**).

5) *Resistor*: In order to accommodate the variable currents needed for the extraction of magnetic signatures, a Resistance Substitution Box Model RS-400 (Elenco Electronics, Wheeling, IL) was used (**Figure 2(b)**).

6) *Connecting cables*: Alligator Clip with Pigtail (Amazon, Seattle, WA) connecting cables was used to establish the circuit with the test material.

7) *Standardization copper and bronze disks*: In order to obtain baseline electromagnetic signatures, standardization copper and bronze metal disks were used: Metal 1" Disc Sample Pack: bronze, copper (K & S Engineering, Highland IN; **Figure 2(c)**).

3. Results

Copper and bronze metal disks were mounted onto the platform and the smartphone was stabilized above the specimen for magnetic field detection. Measurements were taken to acquire baseline magnetic signatures. Electric charges were then applied to the metal disks at 6 volts to induce an electromagnetic field (**Figure 3**).

Electromagnetic signatures were measured in MicroTesla (μT), with results recorded in Table 1. Five different measurements were taken at each point and the averages were presented. At baseline, the copper disk demonstrated 33.26 μT, while bronze (which contains significant amounts of tin) demonstrated 32.15 μT. When both disks were placed in the 6-volt electric circuit, the evoked dynamic electromagnetic strength of copper was 34.06 μT, a net increase of 0.8 μT. The evoked electromagnetic strength of bronze was 32.62 μT with the input of 6-volt electric circuit, with a net increase of 0.47 μT.

(a) (b)

Figure 1. Experimental platform: (a) Multifunctional Welding LED Magnifier Helping Hand Soldering Iron Stand was used as the stabilizing platform for the test material; (b) Aduro Solid-Grip Phone Holder for Desk—Adjustable Universal Gooseneck Smartphone Stand, with Durable Rubberized Mount, was used as the smartphone holder.

(a) (b) (c)

Figure 2. Variable power source and variable resistor: (a) Tekpower TP3016M Portable Handheld Variable DC Power Supply with USB Port, 0.3 V - 12 V @ 0 - 3.75 A or 0.3 V - 30 V @ 1.6 A with VC and CC Control, Upgraded TP3005D, HY3005; (b) Resistance Substitution Box Model RS-400; (c) Calibration metal disks (Metal 1" Disc Sample Pack: bronze, copper).

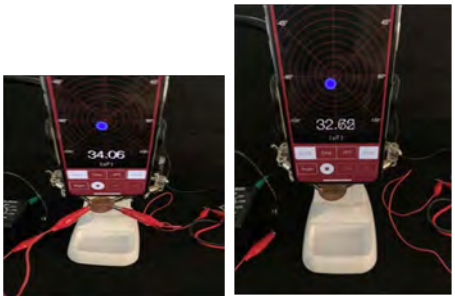

(a) (b)

Figure 3. Magnetic field measurements for (a) copper and (b) bronze at 6 V.

Table 1. Electromagnetic field measurements of copper and bronze at baseline and in dynamic 6-volt circuit.

	Copper	*Bronze*
Magnetism in MicroTesla (μT)		
Baseline Magnetism	33.26	32.15
Electromagnetism	34.06	32.62
Differential Magnetic Signatures	**0.8**	**0.47**

4. Discussion

Bronze artifacts are valued for their luster and durability and have been continuously produced across the world since the dawn of the Bronze Age in 3300 BC. Copper and tin ores were harvested from different mines across the world, and their local geography often dictated the types of minerals that were commingled with copper and tin as they were purified and extracted. In addition, since these ancient alloys were forged before the creation of the Periodic Table and knowledge of chemical reactivities and properties, there was considerable variability as to the purity and relative ratio of different elements within each bronze artifact. Bronze alloys created via such techniques would thus have unique chemical signatures and may provide a method to uniquely identify bronze produced from different regions of the world.

The ability to chemically analyze bronze is often expensive and destructive and invariably involves expensive equipment in large laboratories. We previously developed a technique to identify different steel alloys based on their differing magnetic signatures due to different chemical compositions (Chen, 2019), and we demonstrated that the technique can be used also to analyze bronze alloys (Vickers Hardness Test, 2020). In the current article we detail the experimental protocol for conducting such an extraction of dynamic magnetic signatures.

The current technique is possible due to the wide availability of smartphones, which provide a portable and inexpensive yet powerful magnetometer. In the current study we observed different electromagnetic measurements and differentials between copper and bronze specimens. The higher electromagnetic level observed with copper was most likely due to the higher electroconductivity of copper versus bronze. In addition, copper not only showed a higher electromagnetic field at baseline, it also showed a higher spike of evoked electromagnetic level when stimulated by an electric circuit, as compared to bronze.

In conclusion, there had not been a simple, inexpensive, and portable method of assessing the metal composition of an alloy and, indirectly, its identity. The current method of utilizing dynamic electrodynamic signatures as a method of differentiating copper and bronze artifacts represents a novel method to identify bronze objects of different compositions. The next step of research would need to establish a standardization table of electromagnetic signatures of bronze alloys containing different copper-to-tin ratios. In addition, such a table would need to

be repeated at different electric currents in order to document the evoked dynamic electromagnetic signatures. Having such a database of measurements would help researchers compare any new bronze artifact to the set of known electromagnetic signatures, and may help to estimate the chemical composition of the query bronze material.

Conflicts of Interest

The author declares no conflicts of interest regarding the publication of this paper.

References

Arribas, E. (2015). Measurement of the Magnetic Field of Small Magnets with a Smartphone: A Very Economical Laboratory Practice for Introductory Physics Courses. *European Journal of Physics, 36,* 11. https://doi.org/10.1088/0143-0807/36/6/065002

Baldini, G. B. (2017). Identification of Mobile Phones Using the Built-In Magnetometers Stimulated by Motion Patterns. *Sensors, 17,* 783. https://doi.org/10.3390/s17040783

Bennett, D. R. (2020). *Stages of Wood Burning Combustion.* http://www.flameandcomfort.com/archives/blog/311

Chen, L. (2020a). Differentiation of Fencing Blade Alloys Using iPhone Magnetometer. *Journal of Experimental Techniques and Instrumentation.* (In Press)

Chen, L. B. (2019). *Determining Fencing Blade Quality Using Dynamic Magnetic Field Measurements.* United States Patent and Trademark Office.

Chen, L. B. (2020b). Rapid Identification of Saber Steel Flexibility, Microhardness, and Chemical Composition by Analyzing Electromagnetic Signatures. *American Journal of Sports Science, 8,* 29-32.

Chen, L. B. (2020c). *Determining Composition of Metal Artifacts Using Dynamic Electromagnetic Profile Managements.* United States Patent and Trademark Office.

Curry, A. (2020). *Sword-Wielding Scientists Show How Ancient Fighting Techniques Spread across Bronze Age Europe.* Science News. https://doi.org/10.1126/science.abc2715

Gale, N. H., Stos-Gale, Z. A., & Gilmore, G. R. (1985). Alloy Types and Copper Sources of Anatolian Copper Alloy Artifacts. *Anatolian Studies, 35,* 143-173. https://www.jstor.org/stable/3642880 https://doi.org/10.2307/3642880

Logan, J. (2007). *Identifying Archaeological Metal-Canadian Conservation Institute (CCI) Notes 4/1.* Government of Canada. https://www.canada.ca/en/conservation-institute/services/conservation-preservation-publications/canadian-conservation-institute-notes/identifying-archaeological-metal.html

Lopez, A. M. (2009). *Metalworking through History: An Encyclopedia.* Westport, CT: Greenwood.

Metal Supermarkets (2015). *Which Metals Conduct Electricity?* https://www.metalsupermarkets.com/which-metals-conduct-electricity/

Muhly, J. D. (1976). *Copper and Tin: The Distribution of Mineral Resources and the Nature of the Metal Trade in the Bronze Age.* Hamden: Archon.

Muhly, J. D. (1985). Sources of Tin and the Beginnings of Bronze Metallurgy. *American Journal of Archaeology, 89,* 275-291. https://www.jstor.org/stable/504330

https://doi.org/10.2307/504330

Odenwald, S. (2019). Smartphone Sensors for Citizen Science Applications: Radioactivity and Magnetism. *Citizen Science: Theory and Practice, 4,* 18. https://doi.org/10.5334/cstp.158

Raymond, R. (1984). *Out of the Fiery Furnace: The Impact of Metals on the History of Mankind.* University Park, PA: Penn State University.

Scott, D. A. (1991). *Metallography and Microstructure of Ancient and Historic Metals.* Marina del Rey, CA: Getty Conservation Institute in Association with Archetype Books. http://hdl.handle.net/10020/gci_pubs/metallography_microstructure

Vickers Hardness Test (2020). https://www.gordonengland.co.uk/hardness/vickers.htm

Archaeological Discovery, 2020, 8, 207-227
https://www.scirp.org/journal/ad
ISSN Online: 2331-1967
ISSN Print: 2331-1959

The Sandstone Quarries of the Angkor Monuments in the Southeastern Foothills of Kulen Mountain

Etsuo Uchida[1], Ryota Watanabe[1], Motoki Murasugi[1], Yuichiro Sakurai[1], Ichita Shimoda[2]

[1]Department of Resources and Environmental Engineering, Faculty of Science and Engineering, Waseda University, Tokyo, Japan
[2]World Heritage Studies, Graduate School of Comprehensive Human Sciences, University of Tsukuba, Ibaraki, Japan
Email: weuchida@waseda.jp

How to cite this paper: Uchida, E., Watanabe, R., Murasugi, M., Sakurai, Y., & Shimoda, I. (2020). The Sandstone Quarries of the Angkor Monuments in the Southeastern Foothills of Kulen Mountain. *Archaeological Discovery, 8,* 207-227.
https://doi.org/10.4236/ad.2020.83012

Received: April 19, 2020
Accepted: May 12, 2020
Published: May 15, 2020

Abstract

The Angkor monuments in Cambodia were designated as a UNESCO World Heritage Cultural Site and consist of Buddhist or Hindu temples built mainly of sandstone and laterite. We surveyed the area around a 2 km east-west bank in Kulen Mountain's southeastern foothills for Angkor's sandstone quarries and confirmed 145 locations. Because the magnetic susceptibilities and size of sandstone blocks at Angkor changed systematically over time, we measured these aspects at each quarry. Based on this data, we identified seven Angkor quarrying areas (Areas A to G). The results clarified that in the Angkor period, sandstone block quarrying began near the bank's eastern end, then moved counterclockwise to the north side of the bank. Because quarries are important Angkor period heritage sites, they should be designated as conservation areas for their protection.

Keywords

Angkor Monument, Sandstone, Quarry, Kulen Mountain, Cambodia

1. Introduction

As one of the world's largest pre-industrial cities, Angkor is among Cambodia's most important archaeological sites. Located in the current Siem Reap Province, it consists of monuments constructed between the 9th and 15th centuries AD (hereafter, assume all dates are AD). Studying the temples' construction materials has led to several key findings. While some 9th to 10th century Angkor temples contained bricks, sandstone and laterite were the primary construction materials used. The Angkor monuments contain three types of sandstone: gray-yellowish

brown sandstone (feldspathic arenite), red sandstone (quartz arenite), and greenish graywacke (feldspathic wacke) (Uchida et al., 1998).

Different usage of the three sandstones suggests various levels of importance. The Banteay Srei temple, for example, was built mainly of red sandstone; few red sandstone blocks were found among gray-yellowish brown sandstone blocks at late Bayon period or later temples (the 13th century). Greenish graywacke was only utilized in five sanctuaries on the top of the Ta Keo temple (Uchida et al., 1998) but was frequently used for statues and Hindu Linga-Yoni sculptures. This suggests that despite the infrequent usage, greenish graywacke was an important stone for the Angkor monuments. Meanwhile, gray-yellowish brown sandstone was present in every temple, used even in the Banteay Srei temple in its entrance, window frames, and lattice windows; therefore, this sandstone was the most important found in the Angkor monuments.

Gray-yellowish brown sandstone is widely distributed in eastern but not western Cambodia; it can also be found in Vietnam, Laos, and around the Khorat Plateau in Thailand (Tien et al., 1990; Mantajat & Hinthong, 1990). It was commonly used in large-scale temples, such as the Angkor, Beng Mealea, Koh Ker, Preah Khan of Kompong Svay, and Banteay Chhmar temples in Cambodia as well as the Wat Phu temple in Laos (Uchida et al., 2010, 2013, 2014). In Cambodia, this material is produced from the Terrain Rouge Formation (ESCAP, 1993); in Thailand, it is called the Phu Kradung Formation (Meesook et al., 2002). The formation has recently been classified as of the Late Jurassic to Early Cretaceous (Meesook, 2011).

The chemical and mineral composition of the gray-yellowish brown sandstone is homogenous throughout the Angkor temples (Uchida et al., 1998). However, the sandstone's magnetic susceptibility varies depending on the construction period (Uchida et al., 1998, 2003, 2007). Based on the Angkor blocks' magnetic susceptibilities, Uchida et al. (1998, 2007) predicted that there were seven quarries (quarrying areas) used during the Angkor period. The gray-yellowish brown sandstone production area closest to the Angkor monuments is located in Kulen Mountain's southeastern foothills, about 30 km northeast of the Angkor area. Garnier (1873) and Delaporte (1880) first reported on these quarries while Delvert (1963) and Boulbet (1979) presented a rough distribution of sandstone quarries. Carò and Im (2012) and Uchida and Shimoda (2013) recently conducted detailed surveys.

Uchida and Shimoda (2013) revealed 56 quarries' locations. They estimated the period when the sandstone blocks were removed based on their magnetic susceptibilities and the step heights of the sandstone quarries. Upon examining Areas A to G deduced by Uchida et al. (1998, 2007), Uchida and Shimoda (2013) indicated that quarrying Areas C to G had moved over time. Additionally, they revealed the transportation route for the sandstone blocks from Kulen Mountain. Evans (2016) determined the sandstone quarries' distribution using airborne laser scanning of Kulen Mountain's southeastern foothills but has not

presented detailed data. We expected to identify additional quarries and continued investigating them to clarify the distribution area and quarrying period. We report the results here.

2. Methods

Uchida and Shimoda (2013) utilized Google Earth to reveal the existence of a 2 km bank along Kulen Mountain's southeastern foothills. They speculated that the bank is related to the transportation of sandstone blocks due to a canal connecting the quarrying area to the Angkor area along the southwest side of the bank. Thus, this research focused there. We conducted surveys mainly in February and March due to the vegetation and climate at that time of year. In addition, dead grasses are burned then, improving visibility. An air survey was also attempted using a drone (DJI Phantom 3 Pro), but it proved difficult to locate quarries unless they were large and highly visible. We recorded the location of quarries discovered during this survey using GPS, photographed them, and non-destructively measured the sandstone's magnetic susceptibility on site at up to 30 points (ZH instruments SM30, Brno, Czech Republic). Measuring magnetic susceptibility is easy and rapid (a few second per point), with high accuracy (1×10^{-6} SI units). Uchida et al. (1998) first succeeded in classifying the Angkor monument sandstone using magnetic susceptibility. Additionally, we measured step height at up to 20 points because the Angkor monument sandstone blocks thinned over time.

3. Results

3.1. Distribution and Shape of the Quarries

In this survey, we confirmed 89 sandstone quarries beyond the 56 previously identified (Uchida and Shimoda, 2013), bringing the total to 145 (**Figure 1**). Photographs of all of the quarries are presented in **Appendix 1** (**Figure A**). In addition, the location of each quarry is shown in **Figure 2** and **Table 1**.

Most quarries are concentrated in the east and north sides of the bank and distributed on the foothills' slopes (approximately 90 - 100 m asl) and tops (approximately 120 - 130 m asl). The sandstone quarries' distribution depicted in **Figure 2** coincides with data obtained through airborne laser scanning (Evans, 2016). Although the planar spread is not always clear, many quarries are on the order of 10 - 30 m. Quarries are generally less than 2 m high but occasionally reach 6 m. Their traces are generally in the form of steps, but sometimes the quarries are found in flat areas as well. The step height is often 30 - 50 cm, but occasionally exceeds 60 cm; the average step height is 41 cm. Oblique quarrying traces were observed on the quarries' stone surfaces, which may suggest the use of pickaxes (**Figure 1(D)**).

3.2. Magnetic Susceptibility

The average magnetic susceptibility in each quarry is 0.33×10^{-3} SI units (quarry

no. 43) at a minimum and 5.82×10^{-3} SI units (quarry no. 70) at a maximum (Table 1). The total average value is 2.02×10^{-3} SI units. The sandstone quarries with high magnetic susceptibilities are concentrated near the bank's eastern end and about 1 km north of the eastern end. In the latter case, the step height tends to be higher.

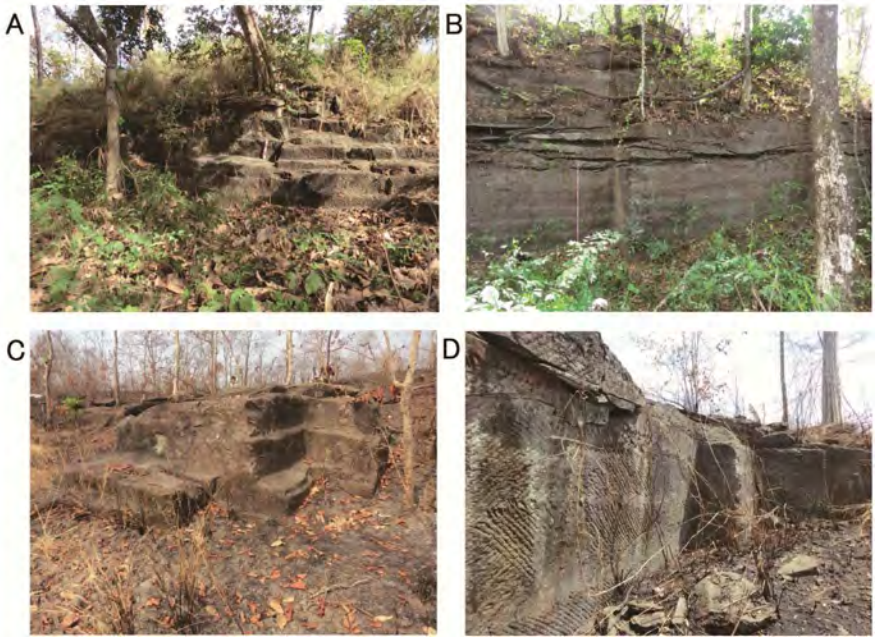

Figure 1. Photographs of representative sandstone quarries in Kulen Mountain's southeastern foothills. Photographs of all sandstone quarries are presented in **Appendix 1** (Figure A). Quarries no. (A) 62, (B) 66, (C) 84, and (D) 123.

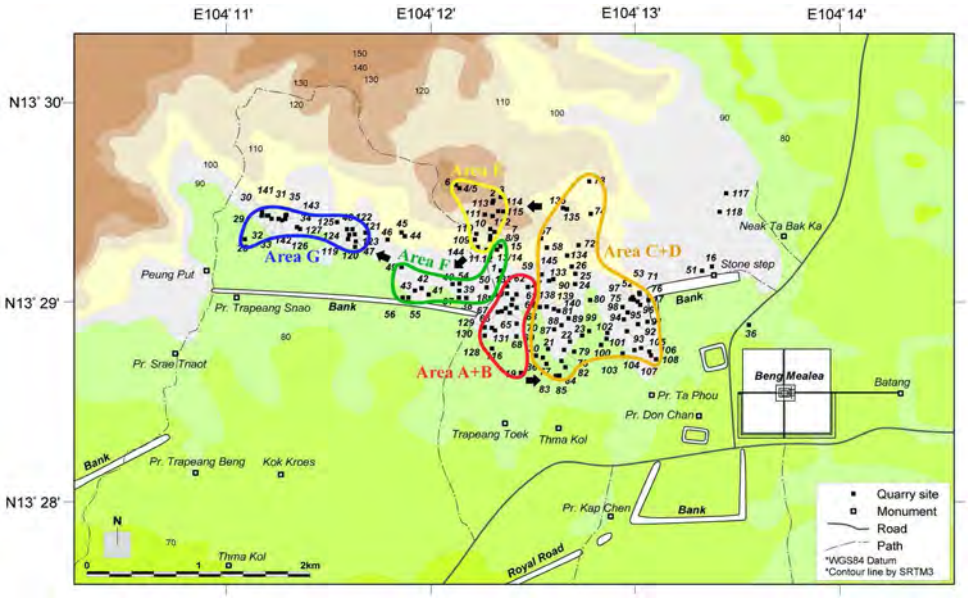

Figure 2. Distribution of sandstone quarries used during the Angkor period in Kulen Mountain's southeastern foothills.

Table 1. Location, average magnetic susceptibilities, and average step heights of confirmed sandstone quarries.

Quarry No.	Latitude	Longitude	av. S.H.**	av. M.S.*	Quarry No.	Latitude	Longitude	av. S.H.**	av. M.S.*
1	13˚29'09.32"N	104˚12'19.53"E	41.7	0.68	74	13˚29'25.20"N	104˚12'45.90"E	44.9	1.6
2	13˚29'29.46"N	104˚12'18.80"E	65.5	1.28	75	13˚29'00.50"N	104˚12'57.60"E	46	0.33
3	13˚29'30.26"N	104˚12'19.56"E	57.3	2.70	76	13˚28'59.70"N	104˚12'59.90"E	33.8	0.46
4	13˚29'33.54"N	104˚12'08.89"E	N/A	2.67	77	13˚28'41.40"N	104˚12'34.90"E	43.9	2.80
5	13˚29'32.80"N	104˚12'07.86"E	47.3	2.82	78	13˚28'45.50"N	104˚12'40.00"E	40.8	1.80
6	13˚29'33.93"N	104˚12'07.24"E	56.4	4.53	79	13˚28'45.20"N	104˚12'43.00"E	N/A	2.05
7	13˚29'20.95"N	104˚12'16.45"E	46.9	2.09	80	13˚29'00.00"N	104˚12'47.70"E	N/A	0.97
8	13˚29'20.10"N	104˚12'18.05"E	47.5	3.31	81	13˚28'56.80"N	104˚12'38.50"E	40.1	1.62
9	13˚29'19.36"N	104˚12'18.42"E	39.2	2.99	82	13˚28'42.20"N	104˚12'39.30"E	39.7	1.12
10	13˚29'18.58"N	104˚12'17.06"E	43.4	3.57	83	13˚28'37.90"N	104˚12'38.60"E	N/A	1.49
11	13˚29'18.08"N	104˚12'17.86"E	49.2	3.38	84	13˚28'40.40"N	104˚12'40.30"E	41.5	1.42
12	13˚29'15.40"N	104˚12'16.76"E	N/A	3.50	85	13˚28'38.10"N	104˚12'37.50"E	37	1.54
13	13˚29'14.93"N	104˚12'18.39"E	44.8	1.05	86	13˚28'43.30"N	104˚12'33.70"E	44.3	2.21
14	13˚29'15.25"N	104˚12'19.39"E	41.5	1.98	87	13˚28'51.50"N	104˚12'37.30"E	40.5	2.05
15	13˚29'14.48"N	104˚12'18.34"E	55.3	1.15	88	13˚28'52.70"N	104˚12'39.50"E	N/A	1.51
16	13˚29'09.50"N	104˚13'21.50"E	N/A	1.99	89	13˚28'54.60"N	104˚12'41.40"E	43.2	1.58
17	13˚29'00.30"N	104˚13'04.50"E	53.3	2.46	90	13˚29'05.40"N	104˚12'35.90"E	N/A	0.91
18	13˚29'01.20"N	104˚12'17.40"E	47.8	0.97	91	13˚28'53.60"N	104˚13'04.20"E	44.3	1.52
19	13˚28'39.00"N	104˚12'25.75"E	44.4	2.49	92	13˚28'53.00"N	104˚13'01.40"E	46.5	1.82
20	13˚28'43.61"N	104˚12'31.80"E	42.5	1.61	93	13˚28'51.00"N	104˚12'58.30"E	44.5	2.32
21	13˚28'46.14"N	104˚12'33.44"E	41.5	1.92	94	13˚28'54.40"N	104˚12'57.50"E	43.2	3.26
22	13˚28'48.03"N	104˚12'41.82"E	53.1	2.14	95	13˚28'56.40"N	104˚12'58.50"E	47	1.53
23	13˚28'50.19"N	104˚12'43.86"E	34.8	2.62	96	13˚28'58.60"N	104˚13'02.10"E	44.4	2.59
24	13˚29'04.63"N	104˚12'42.55"E	43.3	1.90	97	13˚29'00.10"N	104˚13'00.40"E	42.7	1.66
25	13˚29'07.86"N	104˚12'42.55"E	43.1	2.21	98	13˚28'57.90"N	104˚12'57.10"E	44.5	0.86
26	13˚29'09.35"N	104˚12'41.04"E	37.9	4.26	99	13˚28'51.00"N	104˚12'47.40"E	45.4	0.64
27	13˚29'03.79"N	104˚12'27.66"E	63.4	3.64	100	13˚28'46.90"N	104˚12'50.70"E	44.7	3.97
28	13˚29'17.83"N	104˚11'05.23"E	32.8	1.70	101	13˚28'48.70"N	104˚12'52.50"E	50.8	1.97
29	13˚29'25.21"N	104˚11'09.24"E	31.8	2.08	102	13˚28'50.50"N	104˚12'52.70"E	38.3	1.7
30	13˚29'26.14"N	104˚11'09.68"E	31.3	2.01	103	13˚28'44.60"N	104˚12'57.10"E	N/A	0.91
31	13˚29'25.50"N	104˚11'11.94"E	31.9	2.00	104	13˚28'45.50"N	104˚13'00.50"E	44.3	2.52
32	13˚29'24.04"N	104˚11'13.38"E	29.3	1.76	105	13˚28'46.10"N	104˚13'02.40"E	N/A	1.87
33	13˚29'23.55"N	104˚11'14.77"E	34.1	1.63	106	13˚28'45.10"N	104˚13'04.70"E	N/A	0.54
34	13˚29'23.83"N	104˚11'16.71"E	30.3	1.68	107	13˚28'44.30"N	104˚13'05.40"E	42.4	0.97
35	13˚29'24.55"N	104˚11'16.75"E	31.3	2.05	108	13˚28'42.80"N	104˚13'06.80"E	N/A	0.38
36	13˚28'52.70"N	104˚13'33.00"E	33.2	0.77	109	13˚29'17.50"N	104˚12'14.30"E	39	2.23

Continued

37	13˚29'00.63"N	104˚12'07.77"E	31.2	1.44	110	13˚29'19.00"N	104˚12'14.80"E	39	2.13
38	13˚29'01.72"N	104˚12'10.33"E	40.9	1.43	111	13˚29'24.40"N	104˚12'17.50"E	46.2	2.97
39	13˚29'02.77"N	104˚12'08.18"E	27.3	0.75	112	13˚29'24.00"N	104˚12'19.70"E	35	1.51
40	13˚29'04.57"N	104˚12'06.35"E	N/A	0.49	113	13˚29'27.90"N	104˚12'19.70"E	45.3	1.73
41	13˚29'02.44"N	104˚11'58.62"E	42.2	0.80	114	13˚29'25.50"N	104˚12'21.40"E	40	1.05
42	13˚29'03.49"N	104˚11'57.54"E	28.6	1.09	115	13˚29'25.40"N	104˚12'22.70"E	43.3	1.92
43	13˚29'02.70"N	104˚11'55.06"E	36.3	0.33	116	13˚28'45.9"N	104˚12'18.2"E	40.5	1.54
44	13˚29'19.20"N	104˚11'52.17"E	36.2	0.77	117	13˚29'31.9"N	104˚13'27.8"E	N/A	1.52
45	13˚29'20.17"N	104˚11'51.42"E	32.8	0.99	118	13˚29'26.5"N	104˚13'25.9"E	N/A	1.09
46	13˚29'18.17"N	104˚11'46.78"E	N/A	0.54	119	13˚29'18.4"N	104˚11'35.2"E	45.7	3.15
47	13˚29'17.14"N	104˚11'37.99"E	46.1	2.09	120	13˚29'16.5"N	104˚11'37.6"E	53.3	2.53
48	13˚29'20.35"N	104˚11'35.15"E	31.5	1.79	121	13˚29'20.3"N	104˚11'40.4"E	36.2	2.05
49	13˚29'09.82"N	104˚11'50.83"E	N/A	0.88	122	13˚29'21.3"N	104˚11'36.7"E	42	2.81
50	13˚29'03.63"N	104˚12'16.13"E	43.3	0.71	123	13˚29'19.7"N	104˚11'37.3"E	49.8	2.71
51	13˚29'09.20"N	104˚13'18.50"E	N/A	-	124	13˚29'19.6"N	104˚11'35.6"E	39.3	1.41
52	13˚29'02.50"N	104˚12'57.90"E	67.0	1.9	125	13˚29'23.5"N	104˚11'32.0"E	44	2.12
53	13˚29'05.20"N	104˚12'59.90"E	N/A	-	126	13˚29'21.4"N	104˚11'21.2"E	44	1.15
54	13˚29'04.71"N	104˚12'06.97"E	35.5	-	127	13˚29'21.9"N	104˚11'20.2"E	40.3	1.48
55	13˚29'00.99"N	104˚11'54.57"E	N/A	-	128	13˚28'49.8"N	104˚12'16.0"E	38.5	3.35
56	13˚29'01.99"N	104˚11'53.27"E	N/A	-	129	13˚28'52.2"N	104˚12'15.9"E	39	0.52
57	13˚29'18.10"N	104˚12'31.60"E	46.7	2.29	130	13˚28'52.0"N	104˚12'18.2"E	38.3	3.72
58	13˚29'15.30"N	104˚12'33.20"E	41.7	3.12	131	13˚28'51.3"N	104˚12'19.0"E	39.5	4.16
59	13˚29'07.60"N	104˚12'31.10"E	47.2	0.61	132	13˚29'4.4"N	104˚12'22.6"E	31.3	2.99
60	13˚29'02.00"N	104˚12'21.70"E	54.3	2.91	133	13˚29'6.5"N	104˚12'36.4"E	41.1	0.59
61	13˚29'00.40"N	104˚12'23.30"E	30.4	2.81	134	13˚29'13.5"N	104˚12'40.5"E	43.4	2.23
62	13˚29'01.70"N	104˚12'24.50"E	40.4	3.61	135	13˚29'27.2"N	104˚12'40.4"E	41.7	2.72
63	13˚28'57.90"N	104˚12'24.50"E	58.3	1.73	136	13˚29'27.6"N	104˚12'39.3"E	44	1.70
64	13˚28'58.60"N	104˚12'23.10"E	29.8	1.25	137	13˚29'4.2"N	104˚12'29.2"E	45.4	3.03
65	13˚28'57.80"N	104˚12'21.30"E	31.5	1.96	138	13˚28'58.2"N	104˚12'32.5"E	42.2	1.74
66	13˚28'56.90"N	104˚12'20.20"E	34.5	1.56	139	13˚28'58.4"N	104˚12'34.5"E	52	1.92
67	13˚28'56.70"N	104˚12'19.10"E	37.9	2.51	140	13˚28'57.7"N	104˚12'35.6"E	44.7	1.33
68	13˚28'49.50"N	104˚12'24.40"E	51.4	2.5	141	13˚29'25.0"N	104˚11'11.2"E	32.6	1.97
69	13˚28'53.30"N	104˚12'24.60"E	41.0	4.13	142	13˚29'23.6"N	104˚11'15.8"E	31.4	1.85
70	13˚28'56.40"N	104˚12'22.50"E	37.7	5.82	143	13˚29'24.8"N	104˚11'17.0"E	31.8	1.68
71	13˚29'01.70"N	104˚13'00.20"E	N/A	0.54	144	13˚29'15.8"N	104˚12'13.3"E	45.9	1.32
72	13˚29'16.10"N	104˚12'42.50"E	N/A	1.71	145	13°29'07.7"N	104°12'31.9"E	45.0	0.88
73	13˚29'34.60"N	104˚12'45.60"E	N/A	1.23					

* Average step height (cm), ** average magnetic susceptibility ($\times 10^{-3}$ SI unit).

4. Discussion

Uchida et al. (2003, 2007) measured the magnetic susceptibility of Angkor's gray-yellowish brown sandstone and classified the temple construction into 13 phases (Phases I to VIIIb) (**Figure 3(A)**, **Figure 3(B)**). Judging from the frequency histogram of the magnetic susceptibility of gray-yellowish brown sandstone at each phase, they inferred that there were seven quarrying areas (Areas A to G) of gray-yellowish brown sandstone in the Angkor period (**Figure 3(C)**). Area A's sandstone has a relatively low magnetic susceptibility, with the average ranging from 1.1 to 2.3 × 10^{-3} SI units. Area B's sandstone has a very wide range of magnetic susceptibility (0.9 to 9.1 × 10^{-3} SI units), and the magnetic susceptibility tends to be high at the early stage and low later. Area C's magnetic susceptibility is somewhat high at 2.3 to 3.0 × 10^{-3} SI units. Area D's magnetic susceptibility has a similar range to that of Area A. The magnetic susceptibility of Area E's sandstone is high (2.8 to 4.3 × 10^{-3} SI units). Area F's sandstone's magnetic susceptibility is the lowest (0.7 to 1.4 × 10^{-3} SI units). Area G's sandstone's magnetic susceptibility is somewhat high at 1.9 to 3.1 × 10^{-3} SI units. The step height is comparatively low in Areas F and G.

According to Uchida et al. (2005), the stone blocks' cross sections, including laterite blocks from the Preah Ko period to the Baphuon period (the late 9th century to middle 11th century), are nearly square, and the side length is about 45 cm, excepting some buildings constructed in the Preah Ko and Bakheng periods (the late 9th century to early 10th century). In the case of the Angkor Wat period (the late 11th century to middle 12th century), some stone blocks have a square cross section, but many are rectangular. Their widths are approximately 45 cm but tend to gradually thin. Larger stones are used exceptionally in the Angkor Wat and Wat Athvea temples.

Combining the quarry distribution map (**Figure 2**) and sandstone blocks' magnetic susceptibility and step height reveal that the quarries on the north side of the eastern half of the bank averaged a magnetic susceptibility as low as 0.96 × 10^{-3} SI units and have a slightly low step height (39.4 cm). These quarries' characteristics coincide with those in Area F of Phase VII (average magnetic susceptibility: 1.07 × 10^{-3} SI units); the quarries are inferred to have been used in the middle to later Bayon period (the late 12th century to early 13th century). The average magnetic susceptibility of the sandstone quarries distributed on the north of the western half of the bank is higher (2.05 × 10^{-3} SI units) than on the north of the eastern half of the bank, and the step height is low (37.3 cm). It is thus speculated that the sandstone quarries on the north of the western half of the bank correspond to Area G (average magnetic susceptibility: 2.28 × 10^{-3} SI units), which dates to the end of the Bayon period through the post-Bayon period (the 13th century).

Many sandstone quarries with high magnetic susceptibilities (2.58 × 10^{-3} SI units in average) occur about 1 km north of the eastern end of the bank and have high steps (average height: 45.7 cm). It is thus deduced that these quarries cor-

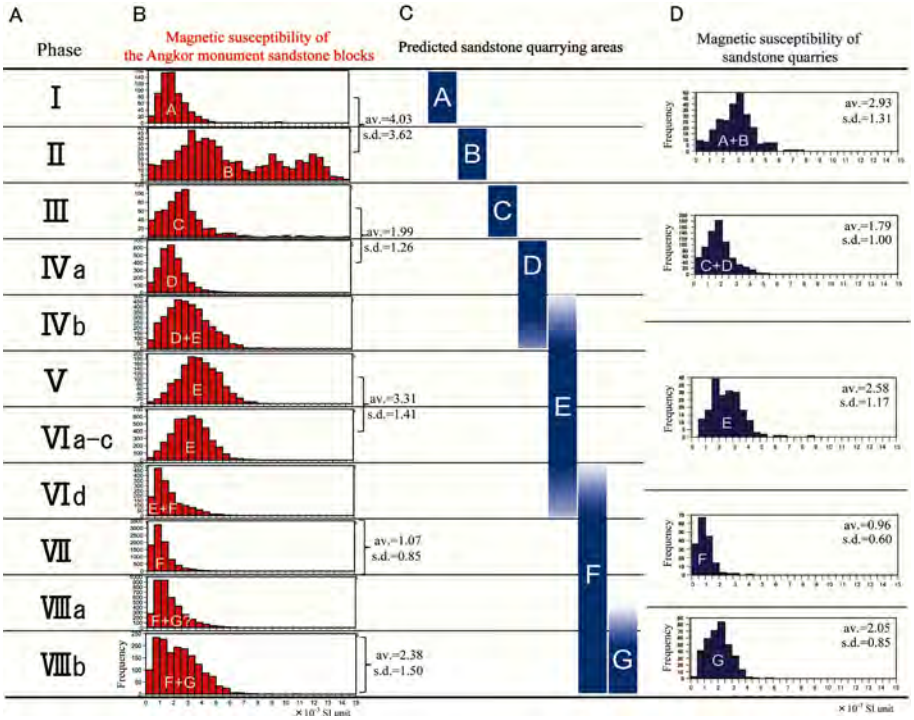

Figure 3. Frequency histograms of magnetic susceptibilities of sandstone in the quarrying Areas A + B, C + D, E, F, and G (**Figure 2**). (A) Construction phases based on the blocks' magnetic susceptibilities; (B) frequency histograms of sandstone's magnetic susceptibilities by construction phase, (C) predicted sandstone quarrying areas (Uchida et al., 2007); and (D) frequency histograms of sandstone in the deduced quarrying Areas A + B to G, which seem to agree with those for sandstone blocks used during each phase.

respond to Area E (average magnetic susceptibility: 3.31×10^{-3} SI units) from the Angkor Wat period through the early Bayon period (the late 11th century to late 12th century) (Phases V to VIc).

Areas A to D cannot be clearly classified. Area A + B (**Figure 2**) contains sandstones with low to high magnetic susceptibility (0.52 to 5.82×10^{-3} SI units, averaging 2.93×10^{-3} SI units), and the step height varies greatly from 29.8 to 63.4 cm (averaging 41.4 cm). Although Areas A and B cannot be distinctly classified, the features of both Areas A and B appear in Area A + B (average magnetic susceptibility: 4.03×10^{-3} SI units). In Area C + D, the variation is smaller than Area A + B's and the magnetic susceptibility ranges from 0.33 to 4.26×10^{-3} SI units (averaging 1.79×10^{-3} SI units). Furthermore, because the step height is close to the characteristic step height of the transition period through the Baphuon period (the early 10th century to middle 11th century) (34.8 to 67.0 cm, averaging 45.7 cm), Area C + D corresponds to Areas C and D (average magnetic susceptibility: 1.99×10^{-3} SI units).

Compared to the magnetic susceptibility of the sandstone blocks used in the temples, the magnetic susceptibility of sandstone in the quarrying sites tends to below. This is probably due to the deterioration of sandstone surface from plant growth and the uneven surface of the sandstone in the quarrying sites.

Figure 3(D) is a frequency histogram of magnetic susceptibilities in inferred quarrying Areas A to G. Area A + B has less sandstone with a magnetic susceptibility of 6×10^{-3} SI units or more when compared with the frequency histogram by Uchida et al. (2007), and there is very little sandstone with a magnetic susceptibility above 6×10^{-3} SI units in other areas. The other areas (Areas C to G) display a trend similar to that obtained by Uchida et al. (2007). Assuming that the estimated quarrying period is correct, the quarrying of sandstone blocks in the Angkor period began near the eastern end of the bank and then moved eastward. In the Angkor Wat period (the late 11th century to middle 12th century), the quarrying moved to the north side of the eastern end of the bank. In the Bayon period, quarrying shifted from the north side of the eastern half of the bank to the north side of the western half of the bank. It is therefore inferred that the quarrying site moved in an overall counterclockwise pattern during the Angkor period. Although there was no difference in sandstone chemical composition among the Angkor temples' blocks, changes in magnetic susceptibility and size over time played an important role in identifying quarries' usage period. Additionally, they clarified the movement of quarrying areas over time. These methods may be applicable to other Khmer monuments.

No evidence of artificial destruction has been found in the quarries investigated so far. Because quarries are also important Angkor period heritage sites, they should be designated as conservation areas for their protection. Many countries are involved in these monuments' restoration. Sandstone blocks from a site near ancient quarry no. 16 are used for restoration. It is desirable that the APSARA National Authority, which manages the archaeological sites in the Angkor area, protect the ancient quarries from destruction.

5. Conclusion

It has long been known that gray-yellowish brown sandstone quarries, which were used for the construction of the Angkor monuments, are located on the southeastern foothills of Kulen Mountain (Garnier, 1873; Delaporte, 1880; Delvert, 1963; Boulbet, 1979). Recently sandstone quarries were investigated by Carò and Im (2012) and Uchida and Shimoda (2013). Uchida and Shimoda (2013) tried to identify the quarrying period of the discovered sandstone quarries. They concluded that quarries used in the early Angkor period have not been discovered. Therefore, in this study, we continued the investigation of quarries on the southeastern foothills of Kulen Mountain. In particular, we surveyed quarries around a 2 km east-west bank. As a result, sandstone quarries have been confirmed at 145 locations in total so far. At each quarry, we measured the magnetic susceptibility and step height. On the basis of these results, we deduced the locations of the seven quarrying Areas A + B, C + D, E, F and G predicted by Uchida et al. (1998, 2007). These results clarify that sandstone quarrying started around the eastern end of the bank and quarrying then moved counterclockwise from the east side to the north side of the bank.

Acknowledgements

This research was financially supported in part by Grants-in-Aid for Scientific Research of the Japan Society for the Promotion of Science (Uchida: no. 23401001) and Waseda University Grants for Special Research Projects (Uchida: no. 2016B-137). We wish to thank members of the Japanese government team for safeguarding Angkor and for their kind help during this research. We would like to thank Editage for the English language editing.

Conflicts of Interest

The authors declare no conflicts of interest regarding the publication of this paper.

References

Boulbet, J. (1979). *Le Phnom Kulen et sa région. Collection de Textes et Documents sur l'Indochine, École Franç.* d'Extrême-Orient.

Carò, F., & Im, S. (2012). Khmer Sandstone Quarries of Kulen Mountain and Koh Ker: A Petrographic and Geochemical Study. *Journal of Archaeological Science, 39,* 1445-1454. https://doi.org/10.1016/j.jas.2012.01.007

Delaporte, L. (1880). *Voyage au Cambodge. L'architecture khmer.* Delagange.

Delvert, L. J. (1963). Recherches sur l'érosion des grès des monuments d'Angkor. *Bulletin de l'Ecole française d'Extrême-Orient, 51,* 453-534. https://doi.org/10.1016/j.jas.2012.01.007

ESCAP (1993). *Atlas of Mineral Resources of the ESCAP Region: Geological Map of Cambodia; Mineral Resources Map of Cambodia* (Vol. 10). United Nations.

Evans, D. (2016). Airborne Laser Scanning as a Method for Exploring Long-Term Socio-Ecological Dynamics in Cambodia. *Journal of Archaeological Science, 74,* 164-175. https://doi.org/10.1016/j.jas.2016.05.009

Garnier, F. (1873). *Voyage d'exploration en Indochine: effectué pendant les année 1866, 1867 et 1868, Hachette.*

Mantajat, N., & Hinthong, C. (1990). *Geological Map of Thailand, Scale 1:2,500,000.* Geological Survey Division, Department of Mineral Resources.

Meesook, A. (2011). Cretaceous. In M. F. Ridd et al. (Eds.), *The Geology of Thailand* (pp. 169-184). New York: Geological Society. https://doi.org/10.1144/GOTH.8

Meesook, A., Suteethorn, V., Chaodumrong, P., Teerarungsigul, N., Sardsud, A., & Wongprayoon, T. (2002). *Mesozoic Rocks of Thailand: A Summary* (pp. 82-94). Proceedings of the Symposium on Geology of Thailand.

Tien, P. C., An, L. D., Bach, L. D., Bac, D. D., Vongdara, B., Phengthavongsa, B., Danh, T., Dy, N. D., Dung, H. T., Hai, T. Q., Khuc, V., Kun, S. C., Long, P. D., Ly, M. N., My, N. Q., Ngan, P. K., Ngoc, N., Ratanavong, N., Quoc, N. K., Quyen, N. V., Aphaymani, S. D., Thanh, T. D., Tri, T. V., Truyen, M. T., & Xay, T. S. (1990). *Geology of Cambodia, Laos and Vietnam. Explanatory Note to the Geological Map of Cambodia, Laos and Vietnam at 1:1,000,000 Scale.* The Geological Survey of Vietnam.

Uchida, E., & Shimoda, I. (2013). Quarries and Transportation Routes of Angkor Monument Sandstone Blocks. *Journal of Archaeological Science, 40,* 1158-1164. https://doi.org/10.1016/j.jas.2012.09.036

Uchida, E., Cunin, O., Shimoda, I., Suda, C., & Nakagawa, T. (2003). The Construction

Process of the Angkor Monuments Elucidated by the Magnetic Susceptibility of Sandstone. *Archaeometry, 45,* 221-232. https://doi.org/10.1111/1475-4754.00105

Uchida, E., Cunin, O., Suda, C., Ueno, A., & Nakagawa, T. (2007). Consideration on the Process and the Sandstone Quarries during the Angkor Period Based on the Magnetic Susceptibility. *Journal of Archaeological Science, 34,* 924-935. https://doi.org/10.1016/j.jas.2006.09.015

Uchida, E., Ito, K., & Shimizu, N. (2010). Provenance of the Sandstone Used in the Construction of the Khmer Monuments in Thailand. *Archaeometry, 52,* 550-574. https://doi.org/10.1111/j.1475-4754.2009.00505.x

Uchida, E., Ogawa, Y., & Nakagawa, T. (1998). The Stone Materials of the Angkor Monuments, Cambodia: The Magnetic Susceptibility and the Orientation of the Bedding Plane of the Sandstone. *Journal of Mineralogy, Petrology and Economic Geology, 93,* 411-426. https://doi.org/10.2465/ganko.93.411

Uchida, E., Shimoda, I., & Shimoda, M. (2013). Consideration of the Construction Period of the Khmer Temples along the East Royal Road to Preah Khan of Kompong Svay and the Provenance of Sandstone Blocks Based on Their Magnetic Susceptibility. *Archaeological Discovery, 1,* 37-48. https://doi.org/10.4236/ad.2013.12004

Uchida, E., Suda, C., Ueno, A., Shimoda, I., & Nakagawa, T. (2005). Estimation of the Construction Period of Prasat Suor Prat in the Angkor Monuments, Cambodia, Based on the Characteristics of Its Stone Materials and the Radioactive Carbon Age of Charcoal Fragments. *Journal of Archaeological Science, 32,* 1339-1345. https://doi.org/10.1016/j.jas.2005.03.011

Uchida, E., Tsuda, K., & Shimoda, I. (2014). Construction Sequence of the Koh Ker Monuments in Cambodia Deduced from Chemical Composition and Magnetic Susceptibility of Its Laterites. *Heritage Science, 2,* 1-11. https://doi.org/10.1186/2050-7445-2-10

Appendix 1


Quarry no.1


Quarry no.2


Quarry no.3


Quarry no.4


Quarry no.5


Quarry no.6


Quarry no.7


Quarry no.8


Quarry no.9


Quarry no.10


Quarry no.11


Quarry no.12


Quarry no.13


Quarry no.14


Quarry no.15

Quarry no.16

Quarry no.17

Quarry no.18

Quarry no.19

Quarry no.20

Quarry no.21

Quarry no.22

Quarry no.23

Quarry no.24

Quarry no.25

Quarry no.26

Quarry no.27

Quarry no.28

Quarry no.29

Quarry no.30

Quarry no.31

Quarry no.32

Quarry no.33

Quarry no.34

Quarry no.35

Quarry no.36

Quarry no.37

Quarry no.38

Quarry no.39

Quarry no.40

Quarry no.41

Quarry no.42

Quarry no.43

Quarry no.44

Quarry no.45

Quarry no.46

Quarry no.47

Quarry no.48

Quarry no.49

Quarry no.50

Quarry no.51

Quarry no.52

Quarry no.53

Quarry no.54

Quarry no.55

Quarry no.56

Quarry no.57

Quarry no.58

Quarry no.59

Quarry no.60

Quarry no.61

Quarry no.62

Quarry no.63

Quarry no.64

Quarry no.65

Quarry no.66

Quarry no.67

Quarry no.68

Quarry no.69

Quarry no.70

Quarry no.71

Quarry no.72

Quarry no.73

Quarry no.74

Quarry no.75


Quarry no.76


Quarry no.77


Quarry no.78


Quarry no.79


Quarry no.80


Quarry no.81


Quarry no.82


Quarry no.83


Quarry no.84


Quarry no.85


Quarry no.86


Quarry no.87


Quarry no.88


Quarry no.89


Quarry no.90


Quarry no.91


Quarry no.92


Quarry no.93


Quarry no.94


Quarry no.95


Quarry no.96


Quarry no.97


Quarry no.98


Quarry no.99


Quarry no.100


Quarry no.101


Quarry no.102


Quarry no.103


Quarry no.104


Quarry no.105


Quarry no.106


Quarry no.107


Quarry no.108


Quarry no.109


Quarry no.110


Quarry no.111


Quarry no.112


Quarry no.113


Quarry no.114


Quarry no.115


Quarry no.116


Quarry no.117


Quarry no.118


Quarry no.119


Quarry no.120

Quarry no.121

Quarry no.122

Quarry no.123

Quarry no.124

Quarry no.125

Quarry no.126

Quarry no.127

Quarry no.128

Quarry no.129

Quarry no.130

Quarry no.131

Quarry no.132

Quarry no.133

Quarry no.134

Quarry no.135

Figure A. Photographs indicating the 145 ancient sandstone quarries confirmed in this research.

Archaeological Discovery, 2020, 8, 228-244
https://www.scirp.org/journal/ad
ISSN Online: 2331-1967
ISSN Print: 2331-1959

The *Stp* Kermorvan (Le Conquet—FR)

Giancarlo T. Tomezzoli

Etno-Archaeological Observatory, Munich, Germany
Email: gt21949@gmx.de

How to cite this paper: Tomezzoli, G. T. (2020). The *Stp* Kermorvan (Le Conquet—FR). *Archaeological Discovery, 8,* 228-244.
https://doi.org/10.4236/ad.2020.83013

Received: May 7, 2020
Accepted: June 6, 2020
Published: June 9, 2020

Abstract

The segments of the Atlantic Wall in different countries have been the subject of many publications of various authors. Examples of remains of Atlantic Wall segments, at about seventy years from the WWII end, in the Finistère (FR) at the Keremma dunes, Audierne Bay, Goulven Bay, Aber Wrach, Camaret sur Mer, Cleus Foz, Saint-Pabu and other places have already been proposed to the attention of the readers. The *Stp* Kermorvan, subject of this article, represents a further interesting example of them, which in addition illustrates its interactions with very ancient structures and pre-existing defensive structures. It did not use said ancient structures, but destroyed some of them for its defense exigencies, and did not adapt existing defensive structures to its new defense requirements but re-use them mainly for logistics and personnel lodgment.

Keywords

Atlantic Wall, *Stp*, Kermorvan, Le Conquet, Finistère, France, Megaliths, Fortifications, Bunkers

1. Introduction

In past publications, Atlantic Wall segments, at seventy years from the WWII end, in the Finistère at the Keremma dunes (Tomezzoli, 2006), Audierne Bay (Tomezzoli & Marzin, 2015), Goulven Bay (Tomezzoli, 2016), Aber Wrach (Tomezzoli, 2017a), Camaret sur Mer (Tomezzoli, 2017b), Cleus Foz (Tomezzoli, 2017c), Saint-Pabu (Tomezzoli & Colliou, 2017) and other places have been analysed in details. The *Stp* Kermorvan represents a further interesting example of them.

2. Archaeological Environment

Very many publications dealt with the Kermorvan megaliths. A publication (Sparfel & Pailler, 2010) reported on the Peninsula: six menhirs, five lying

stones, one cromlech, three tumulus or cairns, two dolmens with corridor, two covered alleys and one dolmen (**Figure 1**). Another publication (du Chatellier, 1903a) mentions one megalithic enclosure north to the Porz Pabu isthmus and two parallel megalithic enclosures south of the isthmus. A small Bronze Age necropolis was at the north of the Blanc Sablons isthmus, a funerary case near the menhirs at Fort de Kermorvan and a tumulus was over a small Celtic tomb. Other publications (du Chatellier, 1903b) (Devoir, 1913) (Devoir, 1920) (de Freminville, 1832) report different numbers of megaliths (**Figure 1**, **Figure 2**). Over the centuries and during the WWII, some of them were degraded or destroyed (Sparfel & Pailler, 2010). Nowadays, many of them are covered by vegetation and no longer identifiable, only the menhir near the cromlech and few other megaliths remain visible (**Figure 1**, **Figure 2**).

During the XVII - XIX cen., the defense of Le Conquet area was sustained by coastal batteries, entrenchments, redoubts, crenellated guardhouses (**Figure 1**) and mobile troops. The Fort (Redoute 1849) and Batterie de Quinze were at the north side of Blanc Sablons beach. Five batteries were positioned along Blanc Sablons together with Fort St. Louis (Redoute Vaubain) (48˚22'9.87"N, 4˚45'34.76"W, height 29.3 m), Redoute Interme-diare (48˚21'58.22"N, 4˚45'46.35"W, h. 34.43 m) and Redoute Blanc Sablons with Batterie de Treize (48˚21'54.89"N, 4˚46'3.42"W, h. 21.39). Two batteries were at Fort de Kermorvan and two other at Fort de l'Îlette (**Figure 1**, **Figure 2**). The batteries were formed by eight guns in barbette, i.e. on a platform behind a mound or parapet. The personnel were lodged in the redoubts and/or guardhouses nearby. The redoubts were built at the end of the XVII cen. and modernized in the XIX cen. The Fort

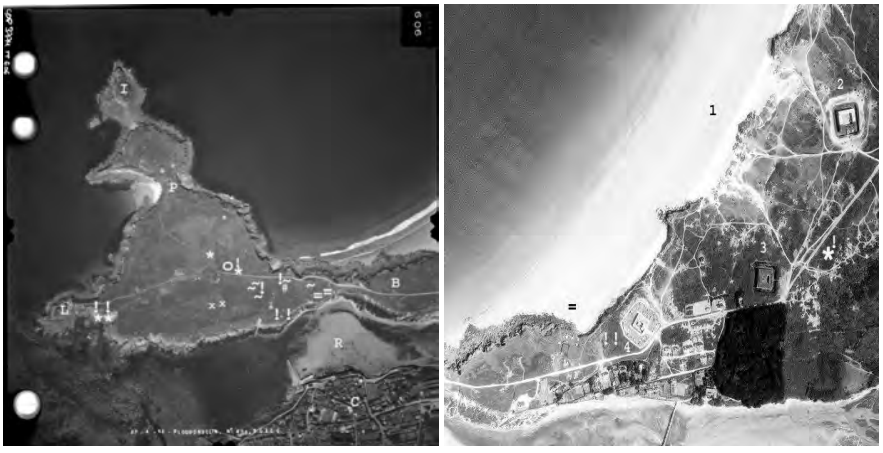

(a) (b)

Figure 1. Archaeological environment: (a) Kermorvan Peninsula: ! menhir; ~ lying stone; o cromlech; * tumulus, cairn; x dolmen with corridor; = covered alley; # dolmen; B Blanc Sablons beach and isthmus; C Le Conquet; L Fort de Kermorvan; I Fort de l'Îlette; P Porz Pabu isthmus; R Ria. C0317-0321_1952_CDP3774_0606, n˚606, 1/5169, Argentique, 27/04/1952; (b) Blanc Sablons: ! menhir; * tumulus; = covered alley; 1 beach; 2 Fort St. Louis (Redoute Vaubain); 3 Redoute intermediare; 4 Redoute Blanc Sablons and Batterie de Treize. C0417-0081_1969_F0317-0417_0016, n˚16, 1/24793, Argentique, 16/07/1969.

(a) (b)

(c) (d)

(e) (f)

Figure 2. Archaeological Environment—(a) menhir near the cromlech; (b) menhir near the access road; (c) Fort St. Louis, front view; (d) Fort St. Louis, rear view; (e) Redoute de Blanc Sablons, on the left main entrance, on the right barrack entrances; (f) Redoute de Blanc Sablons—rear view.

and Batterie de Quinze were built in 1849. The Fort de l'Îlette crenellated guardhouse was a 2nd type, mod. 1846 for 40 soldiers with two brattices per side, commissioned in 1847. Its two batteries supported the fire of the batteries at Blanc Sablons and Fort de Kermorvan. The Fort de Kermorvan crenellated guardhouse was a 3rd type, mod. 1846 with two brattices per side commissioned in 1849 together with the lighthouse. Its two batteries defended Le Conquet and supported the fire of Fort de l'Îlette. Fort St. Louis was built in 1850 for 60 soldiers (Lécuillier, 2004a) (Lécuillier, 2004b). The Fort de Kermorvan and Fort de l'Îlette crenelated guardhouses were built as part of the 1846-1862 French coastal protection program as the Petit Gouin 2nd type, mod. 1846 crenelated guard-

house of 1859 (Tomezzoli, 2017b). Nowadays, all the batteries of Blanc Sablons are no longer identifiable, but the redoubts are in good preservation state and the forts de Kermorvan and de l'Îlette preserve their crenelated guardhouses and battery platforms.

3. History

The support point (*Stützpunkt-Stp*) Kermorvan superposed itself on the variety of structures described above. The *Organization Todt* (OT), from 1942, was in charge of its construction. It was part of the defensive group St. Renan and was formed by the resistance nests (*Widerstandnest-Wn*) Re104 - Re119 composed in total by 16 bunkers operated by infantry and artillery companies (Floch, 2012).

The German 257th Infantry Division back from the east front was at rest in the Finistère from September 1942 to April 1943. The headquarter of the 1st Battalion (unit 30 241A) of its 477th Infantry Regiment, commanded by major Glaser, arrived at Conquet on December 1942 together with the 3rd Company (unit 30 241D), both from Lannion. The Company commander assumed the direction of the Conquet *Kommandantur*. The 1st Battalion moved in reserve to St. Renan on 4th February 1943 replaced, on the same day, by the 2nd Battalion. The headquarters of the 2nd Battalion (unit 34 616A) and the 5th Company (unit 34 616B) of lieutenant Baumann were at Conquet up to April 1943. The headquarter of the 4th Group (unit 38 503A) of its 257th Artillery Regiment was at Conquet from January to April 1943. Its three Group batteries were in the sectors of Plouarzel and Plouzané.

The 113th Infantry Division, annihilated at Stalingrad in February 1943, was reconstituted in the Finistère. The headquarters of the 1st Battalion (unit 32 244A) and the 1st Company (unit 32 244B) of its 268th Infantry Regiment were at Conquet up to June 1943, before to leave for Plounéour-Menez. The headquarter of the 2nd Group (unit 38 909A) of its 87th Artillery Regiment was at Conquet. Its three Group batteries were in the sectors of Ploumoguer and Plouzané.

The 343th Infantry Division, formed on 1st October 1942 as coastal surveillance division for the North Britain, on June 1943 was charged of the sector from Plouescat to Telgruc. The headquarter of the 3rd Battalion (unit 47 943A) of its 852nd Infantry Regiment was at the Beauséjour summer camp in Conquet. One section of the Battalion held the resistance nest *Wn*59 at Pors Liogan near Lochrist. The 4th battery (unit 44 276B) of its 343rd Artillery Regiment, coming from Ploumoguer, was at Conquet from 22 January to July 1944, before to leave for Portzic. The 9th Company (unit 44 276B) and the 3rd Company (unit 06 460S) of the 1st Battalion of the 25th Fortress Troops (*Festungs-Stamm-Truppen*), subordinate to the Brest Defence Command, were present up to the Conquet liberation.

General Ramcke, commander of the *Festung* Brest, entrusted colonel Fürst,

commander of the 899th Regiment of the 266th Division, of the defence of the Conquet pocket. The Regiment was attacked and partially destroyed on 7th-8th August 1944 by the US Army in the sector of Pluvien. Colonel Fürst and an unknown number of German soldiers succeeded in joining the German lines and participated in the Conquet defense. The joint action of the US Army and the FFI (Forces Françaises de l'Interieur) of St. Renan on 9th September 1944 contributed to the rendition of colonel Fürst at his Kerveur en Plougonvelin headquarter near Pointe St. Mathieu.

The 10th September 1944, three hundred German soldiers of *Stp* Kermorvan and one hundred of Pointe d'Ilien laid down their weapons. The same day Le Conquet was liberated.

Sixteen German soldiers were killed at Conquet during the Occupation, of which four in August and four in September 1944 during the Liberation combats (Floch, 2012).

The German Prisoners of War (*POW*s) life conditions were miserable. Inspectors from 1945-1946 noticed flagrant breaches of the Geneva Convention. After his inspection on 16th August 1946, Mr. Courvoisier of the Red Cross International Committee denounced in his report the deplorable treatment of the *POW*s: food was insufficient and the clothes ragged. *POW*s starved, lacked hygiene and the work time lasted from 7h to 18h. Infirmaries were often absent and the mortality rate elevated. The *POW*s were assigned and often exchanged among different camps and commands. On August 1946, the Conquet command comprised 45 *POW*s employed in demining operations and four of them died during demining (Floch, 2009) (Floch, 2012).

4. The Visits

The *Stp* Kermorvan structures positions are shown in **Figure 3**.

A study (Lécuillier, 2004c) identified the following bunkers: 2 × R505 (anti-tank gun bunker), 1 × R515 (machine gun bunker with forward apron), 2 × R601 (anti-tank bunker with roof canopy), 1 × R622 (two groups bunker), 3 × R628 (one group bunker with forward apron), 1 × R635 (two groups bunker with forward apron), 1 × R634 (six embrasures turret bunker), 1 × R638 (small dressing bunker) and 2 × R648 (single embrasure turret bunker).

Another study (Atlantic Wall CO UK, 2018), with images of 03 December 2009, identifies the following Kermorvan *Wn*s, their bunkers and armament:

Re104 nord est—1 × R505. 1 × 3.7 cm Pak 35/36.

Re105 nord est—1 × R634. 1 × Unterstand. 1 × Vf58c.

Re106 nord ouest—1 × R628. 1 × Vf58c. 1 × Stolen.

Re107 nord—2 × R601. 2 × 7.5 cm Pak 97(f).

Re108 nord—1 × R648.

Re109 nord—1 × Vf58c. 1 × Unterstand.

Re110 nord, fortin de L'llette—1 × Casernment.

Re111—1 × R515. 1 × Vf58c.

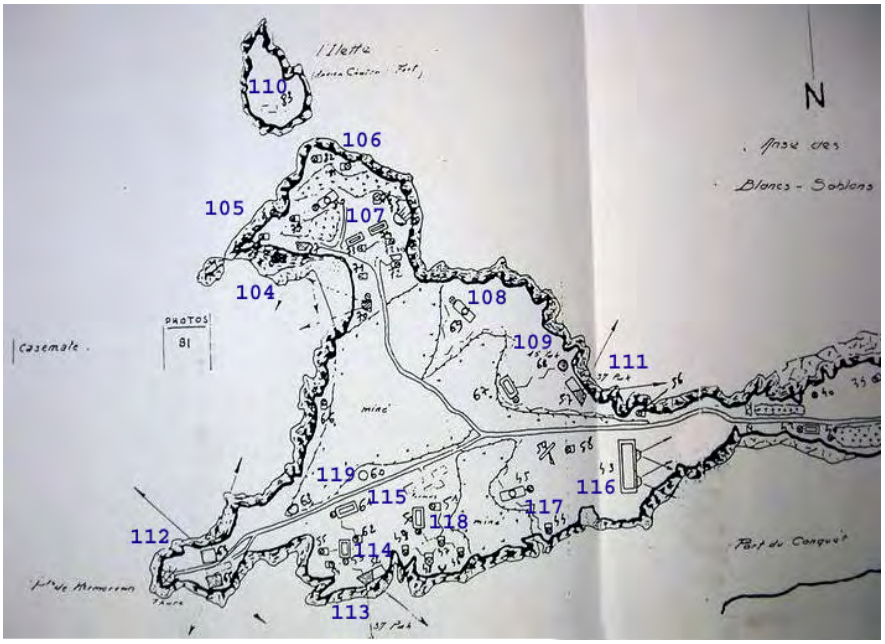

Figure 3. *Stp* Kermorvan—bunkers, mine fields (Pinczon du Sel, 1947-1948) and approximate locations of *Wn* Re104 - Re119.

Re112 ouest Werk "Koln"—2 × SK/Schartenstand. 2 × 7.5 cm K.M.97(f). 1 × Stolen.

Re113 sud—1 × R505. 1 × unterstand. 1 × Vf58c. 1 × 3.7 cm Pak 35/36.

Re114 sud—SK/MG Schartenstand. 1 × R628. 1 × Vf58c.

Re115 sud-est—1 × R634. 1 × Vf58c.

Re116 est—1 SK/Doppel M.G. Schartenstand. 1 × R635. 1 × Stolen.

Re117 centre—1 × R621. 2 × Vf58c.

Re118 centre—1 × 638.

Re119 centre—1 × R628. 2 × Vf58c. 1 × Stolen.

This study permitted to roughly estimate the position of the Kermorvan *Wn*s (**Figure 3**).

The visits took place on 02 January 2012 and 15 May 2017. The *Stp* Kermorvan identified components were the following.

A bunker (48˚21'49.92"N, 4˚46'37.39"W, height 19.31 m) (43) (**Figure 4**) completely covered by vegetation and crossed by the Kermorvan coastal road. The southern-part let only visible an entrance room, obstructed by recent concrete bricks. The room ceiling and walls preserved the original formwork boards imprints, typical of the German masonry, the original white painting disfigured by contemporary graffiti and rusted hammered supports. Because of the vegetation coverage, its type and preservation state remained unknown. The northern part was completely covered by vegetation and no feature was recognizable.

An R505 (48˚21'41.94"N, 4˚47'6.15"W, h. 10.94 m) (52) (**Figure 5**) for PAK gun in the cliff. Its façade was rather damaged by heavy projectile impacts and disfigured by contemporary graffiti. The Ero Vili pebbles (Tomezzoli & Marzin,

2015) were clearly visible on the damaged parts. The front side 485P2 metal plate and the rear side 447P01 armoured door of the combat room were removed. The combat room preserved a semicircular concrete support having a semi-circular and a semi-cylindrical recess, and a severely rusted arched bar. The combat room was damaged by the removal of the 485P2 but preserved its original white painting with graffiti. The covered entrance preserved the close combat room embrasure with splinter guards and its original orange painting. The entrances were closed by recent metallic gates letting visible the good preservation state of corridors and internal rooms preserving their original white painting and rusted ceilings.

The Fort de Kermorvan, Re 112 (48˚21'44.53"N, 4˚47'20.11"W, h. 20.12 m) or Köln Werke, in a military area and consequently not accessible (**Figure 6**). However, it was possible to recognize that to the existing well preserved structures, a southern bunker (48˚21'45.72"N, 4˚47'18.91"W, h. 13.54 m) (65) and a northern bunker (48˚21'44.23"N, 4˚47'18.85"W, h. 10.87 m) (64) were added. The southern bunker was in good preservation state with minor concrete failures on the façade and the splinter guards of the combat room front opening, letting visible rusted concrete reinforced rods. The northern bunker was in good preservation state and the façade let visible the successive concrete pours. An electric distribution cabin, built in local stones, comprising three circular apertures, similar to that of Camp Todt at Tréguennec (Tomezzoli & Marzin, 2015), stood on the northern façade of the crenellated guardhouse.

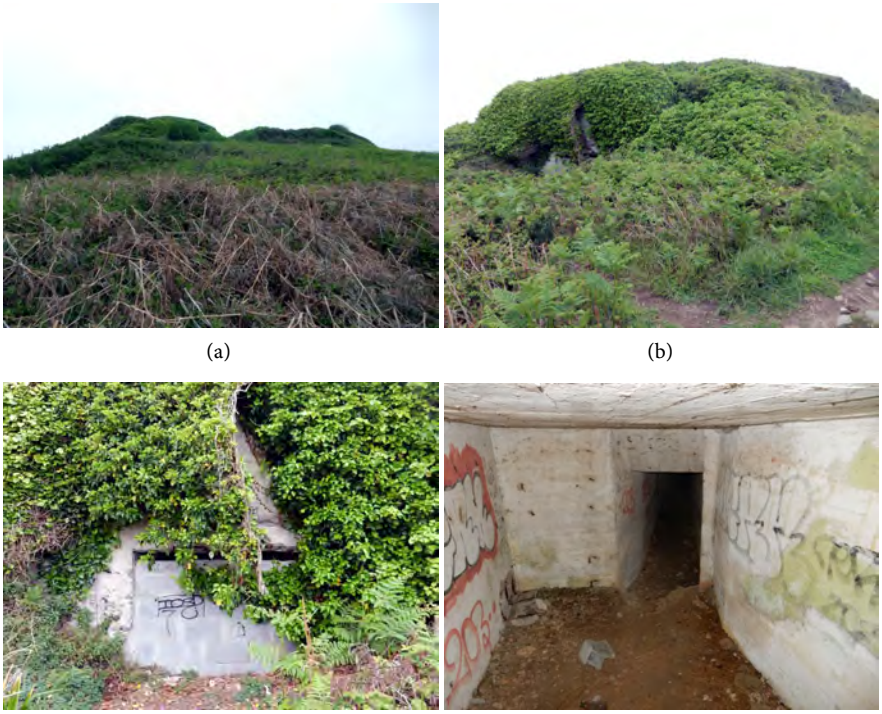

(a) (b)

(c) (d)

Figure 4. Bunker (43)—(a) general view; (b) southern part covered by vegetation; (c) entrance obstructed by concrete bricks; (d) entrance room.

A trench (48˚21'39.38"N, 4˚47'7.32"W, h. 27.49 m) (Figure 7) partially covered by vegetation, connecting a R628 bunker (53), a Vf58c tobruk (62) and a concrete corridor to a 2nd bunker (61). The R628 entrance was closed by a recent metallic gate letting visible a descent ladder and the original white wall painting. The 2nd bunker entrance was closed by a wall and a recent metallic gate, so that the interior was not visible. The tobruk was accessible. Its weapon room was slightly damaged by minor concrete failures letting visible rusted concrete reinforced rods. It preserved two shelves and its original wall white painting. The floor plat

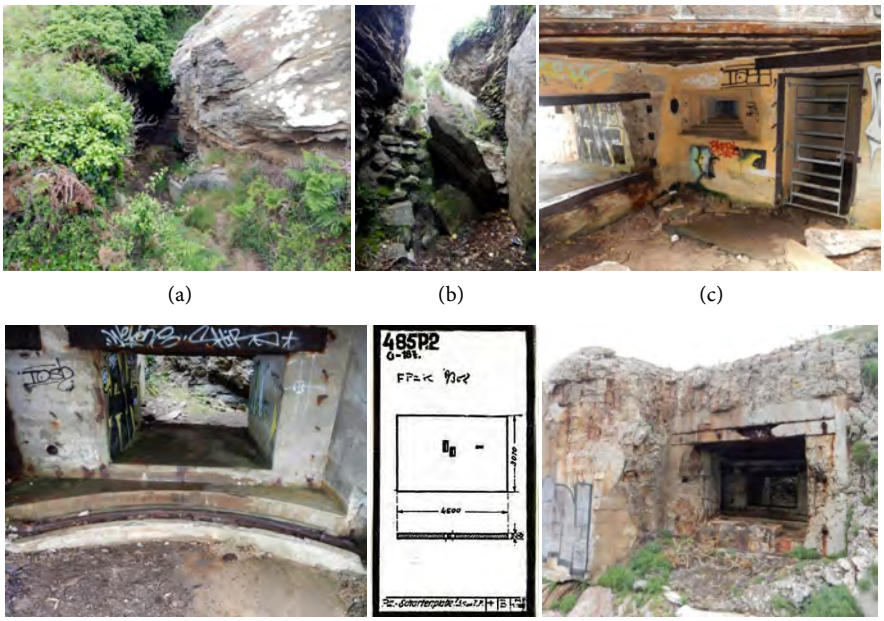

(a) (b) (c)

(d) (e) (f)

Figure 5. R505 (52)—(a) access; (b) access ladder; (c) covered entrance, on the left rear opening of the combat room with supports for the armored door 447P01, in the middle embrasure of the close combat room with splinter guards, on the right entrance, on the top the rusted ceiling; (d) rusted arched bar in the combat room; (e) 485P2 plate, in the middle rectangular openings, on the right rectangular slit; (f) damaged façade, front opening of the combat room with PAK 36 concrete support, and rusted support bolts for 485P2 plate.

(a) (b)

Figure 6. Fort de Kermorvan, Re112—(a) southern side view, 3rd type, mod. 1846 crenellated guardhouse, southern bunker (65), lighthouse; (b) northern side view, crenellated guardhouse with leaning electric distribution cabin, northern bunker (64), lighthouse.

form for elevating the soldier outside its circular opening was removed and the opening was closed by a metallic, beige painted cover having minutes joints irregularly distributed and a 30 cm circular opening closed by a cover with a joint.

A western R601 (48˚22'1.02"N, 4˚47'5.77"W, h. 18.78 m) (Figure 8, Figure 9) for PAK gun. The rectangular PAK gun garage was accessible. Its west side was covered by vegetation. Its front side was in good preservation state letting visible the niche for the PAK gun mouth. Its east side was in good preservation state letting visible at its top four rusted support bolts for the removed 7P7 coverage plate/s. Its floor, covered by terrain, let visible, near the east side, the access manhole to the ammunition room covered by a recent concrete slab. The entrance was closed by a recent metallic gate letting visible a descent ladder, an embrasure of a close combat room, the original wall white and orange painting and the rusted ceiling. The rest of the western R601 and the concrete gun firing place in front of it were covered by grass and vegetation.

An eastern R601 (48˚22'1.74"N, 4˚47'3.96"W, h. 18.76 m) (Figures 8-10) for PAK gun. The rectangular PAK gun garage was accessible. Its west and front sides were covered by vegetation. Its east side was in good preservation state letting visible at its top four rusted support bolts for the removed 7P7 coverage plate/s. Its floor, covered by terrain, let visible, near the east side, the access manhole to the ammunition room covered by a recent concrete slab. The entrance was closed by a recent metallic gate letting visible a descent ladder, an embrasure of a close combat room, the original white and orange painting of the walls and the rusted ceiling. The nice conical shape of the observation post was visible. The rest of the western R601 and the concrete gun firing place in front of it were covered by grass and vegetation.

(a) (b) (c)

(d) (e) (f)

Figure 7. trench—(a) access; (b) R628 (53) entrance; (c) entrance of the 2nd bunker (61); (d) tobruk (62) access; (e) tobruk weapon room; (f) trench exit corridor.

Figure 8. Porz Pabu isthmus—western R601on the left, eastern R601on the right.

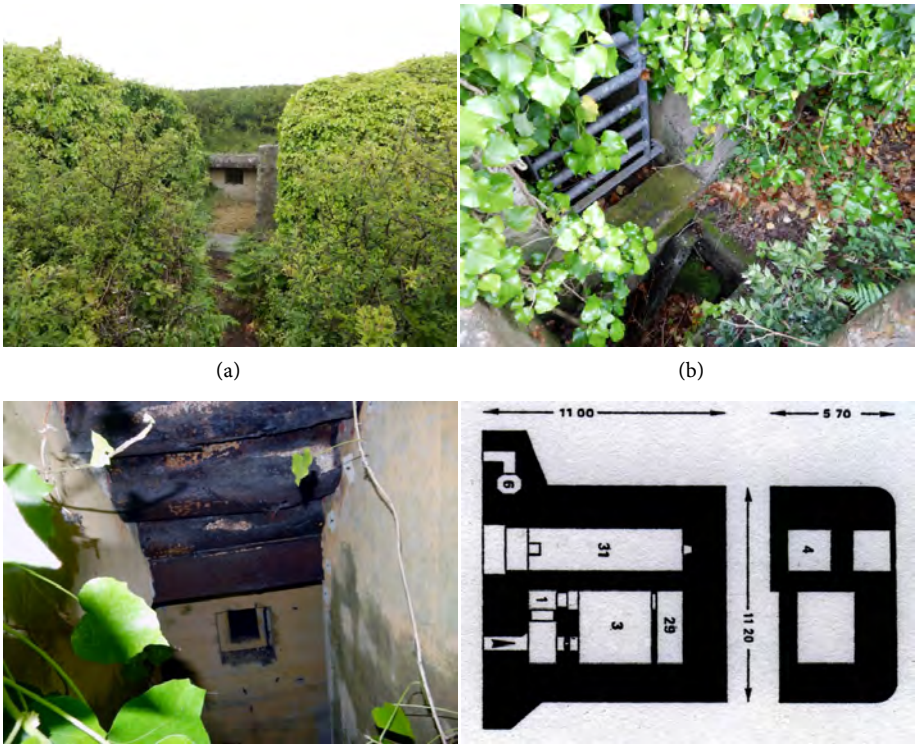

(a) (b)

(c) (d)

Figure 9. Western R601—(a) PAK garage; (b) entrance; (c) close combat room embrasure; (d) R601 plan: 1 gaslock, 3 crew room, 4 ammunition room, 6 observation post, 29 store room, 31 PAK garage (Rudi, 1988).

A one room house (48˚22'1.44"N, 4˚47'11.82"W, h. 14.76 m) (Figure 11) 3 × 6.5 m on the side of a pathway, oriented east-west and leaning against the rocks. The walls were formed externally by superposed local stones tied together by concrete. The original formwork board imprints on the room walls, typical of the German masonry, were clearly visible. The entrance was on the South wall and a small window 60 × 40 cm was on the east wall. The ceiling and the entrance door disappeared. A concrete hut, about 1.5 m high, having an entrance and a cylindrical hole stood against the west wall.

(a) (b)

(c) (d) (e) (f)

Figure 10. Eastern R601—(a) coverage and observation post, upper left Blanc Sablons; (b) PAK garage with covered access manhole to the ammunition room; (c) close combat embrasure; (d) access to the observation post; (e) observation post; (f) obstructed opening.

An R515 (48˚22'0.97"N, 4˚47'12.62"W, h. 13.51 m) (52) (**Figure 12**) for machine gun in the cliff near the one room house and the tobruk. Its whole façade was damaged by heavy projectile impacts. The Ero Vili pebbles (Tomezzoli & Marzin, 2015) were clearly visible on the whole façade. The combat room was damaged by the removal of the front plate but preserved its original white painting and contemporary graffiti. The entrances were closed by recent metallic gates letting visible the good preservation state of corridors and internal rooms, which preserved their original white painting and rusted ceilings. The metallic collar of the periscope hole was visible on the coverage and a trench from R515 to the tobruk was still visible.

The Fort de l'Îlette, Re110 (48˚22'9.33"N, 4˚47'14.2"W, h. 18.43 m) (83) (**Figure 13**) which did not hosted bunkers. Its crenellated guardhouse, walls and battery platforms were in good preservation state.

A tobruk (48˚22'5.23"N, 4˚47'9.34"W, h. 20.75 m) (82) covered by the vegetation (**Figure 14**). The aperture of the weapon room appeared in good preservation state.

A tobruk (48˚21'59.79"N, 4˚47'3.07"W, h. 14.43 m) (71) covered by the vegetation (**Figure 14**). The aperture of the weapon room appeared in good preservation state.

(a) (b) (c)

Figure 11. tobruk Vf58c—(a) west side; (b) weapon room; (c) east side.

(a) (b) (c)

(d) (e) (f)

Figure 12. (a) one room house; (b) R515 and tobruk; (c) R515 plan: 3 crew room, 4 ammunition room; 5 machine gun combat room; (d) access ladder; (e) combat room front opening, (f) combat room rear side and entrance.

Figure 13. Fort de l'Îlette (83), Re110 on the foreground crenellated guardhouse, on the background Blanc Sablons.

(a) (b)

Figure 14. (a) tobruk (82), in the foreground Fort de l'Îlette; (b) tobruk (71) in the foreground western and eastern R601.

5. Discussion

The quite high concentration of megaliths at Kermorvan and Blanc Sablons suggest that here, in the antiquity, for some reason, was a ceremonial and burial center. The cromlech identifies the ceremonial, assembly place and the dolmens the burial places. The meaning and the location purposes of the menhirs remain a mystery. The precise datation of said megaliths is unknown, although it is normally assumed that, in general, they were manufactured in the period 5000 - 4000 BC or 3000 - 1800 BC.

The enlargement of **Figure 1(a)** reveals remains of walls with possible turrets following some paths and crossing the Kermorvan Peninsula. They were not observed because of their degradation and coverage of vegetation. Their manufacturers and datation are unknown.

The forts, redoubts and batteries at Kermorvan Peninsula and Blanc Sablons had not only the purpose of protecting Le Conquet and interdict the access to the Ria, but also to bar the way to Brest and its military port to an army landed at Blanc Sablons.

The *Stp* Kermorvan with its *Wn*s reveals the similar concept of protecting the *Festung* Brest, its *U-Boote* submarine base and military port against an allied army landed at Blanc Sablons.

The Fort de l'Îlette and Fort de Kermorvan crenellated guardhouses hosted the personnel in service at Re 110 and Re 112, ammunitions and materials, although the first was regularly separated from the Kermorvan Peninsula by tides. Other parts of the personnel were lodged in the bunkers, barracks and in Le Conquet. The Blanc Sablons redoubts hosted too personnel and materials.

The lighthouse was used as observation place.

The bunkers (43, 64 - 65) were SK (*Sonderkonstrution*) type. The entrance room (**Figure 4**) observed in bunker (43) rule out a possible R635 type reported by some publications.

The R505 (52) was facing Le Conquet for defending or bombarding it. It hosted one officer, five soldiers and one Skoda 3.7 cm PAK 36 gun placed behind the plate 485P2 of 4.5 m long, 3.01 m wide and 20 cm thick. The gun ammunitions were stored in a room inside the R505. The carriage wheels, the frontal

protection and the gun barrel were disassembled from the gun carriage. The gun barrel and the gun carriage were introduced in the combat room through the rear side 447P01 armoured door. The carriage was secured to a metallic support mounted on the semi-circular and semi-cylindrical recesses of the concrete support and the carriage legs were extended and secured to the arched bar. The gun barrel was introduced in the lower opening of the rectangular 485P2 openings and secured to the carriage. The gun field fire was 60˚ in azimuth and ±10˚ in height. The gun servants controlled the surroundings and aimed the gun using the other 485P2 opening and through the rectangular slit. It is also possible that the servants received aiming instructions from observers outside the R505.

The bunkers connected by the trench were personnel lodgements but might be used also as protected relay commandment place in case of attack. The beige cover of the tobruk had an unknown purpose.

The Fort de Kermorvan southern (65) and a northern (64) bunker were SK type. Because of their large combat room front aperture, the splinter guards and the absence of support bolts for a protective metallic plate, as in the R505, each hosted a bigger 7.5 PAK 97/38 (Atlantic Wall CO UK, 2018). Their combat rooms were connected by an internal tunnel carved into the rock. The electric distribution cabin was probably of French construction for powering the lighthouse and the crenelated guardhouse.

The traces of the original formwork boards imprints on the room, suggest that the one room house was built contemporary with the constructions of the bunkers for lodging the personnel servicing the nearby tobruks. The small window on the east wall served as surveillance of the pathway to the R515 and the hut leaning to the house lodged one or more dogs.

The concrete gun firing places in front of the western and eastern R 601 allowed the two PAK guns to direct the fire toward troupes advancing on the Kermorvan Peninsula from the Grand Sablons isthmus and so protecting the *Wn* 104-107, 110 (**Figure 3**) in which the last resistance would have took place.

The fire of the Kermorvan *Wn*s could have been supported by the fire of the 6 km away Graf Spee battery with its four 280 mm, 20 km in range guns as in the case of the *Stps* of the Goulven Bay (Tomezzoli, 2016).

A supplementary protection was offered by the mine fields interpenetrated between the bunkers (**Figure 3**). Their large extensions explain the presence on August 1946 at Le Conquet of a command comprising 45 *POWs* employed in demining operations.

Surprisingly, no radar was installed at *Stp* Kermorvan.

An estimation of the number of officers and soldiers in service at *Stp* Kermorvan is difficult, however, taking into consideration the number of bunkers and the crenellated guard houses, it can be roughly estimated between 300 and 400.

6. Conclusion

The information collected, the ancient air reconnaissance images and the visit

allowed to clarify many aspects of *Stp* Kermorvan. Only 11 of the total of 16 bunkers have been identified mainly because of the grass and vegetation that covered the other five. Only two of the identified bunkers showed relevant damages due to combats, the other was in good preservation state. The Protected Natural Site of the Kermorvan Peninsula ensures for the moment and in the near future the protection of the *Stp* Kermorvan structures against the risk of Le Conquet urbanization expansion. However, it is regrettable that no initiative has been taken to valorise this part of the historical Finistère heritage.

Acknowledgements

I am grateful to Mr. Fleuridas P. for the discussions concerning the R505 technical features and his consent to publish the R505 plan of the **Appendix**.

Conflicts of Interest

The author declares no conflicts of interest regarding the publication of this paper.

References

Atlantic Wall CO UK (2018). *StP Kermorvan. StP Re104 to Re119, K.V. Gruppe Saint-Renan, Brittany*. http://www.atlantikwall.co.uk/atlantikwall/fbre_stp_kermorvan.php

de Freminville, C.-P. (1832). *Antiquités de Bretagne*, *Finistère*. Lefournier et Deperiers librairies. Brest.

Devoir, A. (1913). Première Contribution à l'Inventaire des Monuments Mégalithiques du Finistère. *BSAF, 40,* 43-46.

Devoir, A. (1920). Notes d'Archéologie Préhistorique. *La Pensée Bretonne, No. 39*.

du Chatellier, P. (1903a). La pointe de Kermorvan en Ploumoguer, ses Monuments, Pierres à Cupole. *BSAF, 30, 90-95*.

du Chatellier, P. (1903b). Les Monuments Mégalithiques de la pointe de Kermorvan en Ploumoguer. *Bulletin Monumental Année, 67,* 232-239. https://doi.org/10.3406/bulmo.1903.11346

Floch, A. (2009). *L'Occupation Allemande dans le Finistère et dans une partie du Morbihan et des Côtes-D'Armor (1940-1944)*. Localisation et Poste aux Armées. Cloitre Imprimeurs. St. Thonan. Finistère.

Floch, A. (2012). *L'Occupation Allemande dans les 162 Communes du Nord Finistère (1940-1944)*. Cloitre Imprimeurs. St. Thonan. Finistère.

Lécuillier, G. (2004a). *Défense des côtes bretonnes: Fortifications du Conquet et de l'anse des Blancs Sablons*. Association Pour l'Inventaire de Bretagne. https://fortifications-neuf-brisach.blogspot.com/2018/01/defense-des-cotes-bretonnes.html

Lécuillier, G. (2004b). *Redoute, année "1850" dit "Fort St.-Louis" (Le Conquet)*. Association Pour l'Inventaire de Bretagne. Dossier IA29001761. http://patrimoine.bzh/gertrude-diffusion/dossier/redoute-annee-1850-dit-fort-St.-louis-le-conquet/5b60ad99-9466-46ee-970e-1361a1f36010

Lécuillier, G. (2004c). *Ensemble fortifié (Stützpunkt "Kermorvan") (Re 104-119), Presqu'île de Kermorvan (Le Conquet)*. Association Pour l'Inventaire de Bretagne. Dossier

IA29001761.
http://patrimoine.bzh/gertrude-diffusion/dossier/ensemble-fortifie-stutzpunkt-kermorvan-re-104-119/5c4a6fdb-f216-4846-9f01-34eb46632c39

Pinczon du Sel (1947-1948). *Rapport. Le Mur de l'Atlantique la Cote de la Manche et de l'Atlantique du Mont Saint-Michel à Laita* (Livre IV, Plan_no. 105). Brest: Service Historique de la Marine.

Rudi, R. (1988). *Typologie du Mur de l'Atlantique*. Amsterdam: Beetsterzwaag. NUGI 923.

Sparfel, Y., & Pailler, Y. (2010). *Les Mégalithes de l'Arrondissment de Brest. Inventaire et Essay de Synthese*. Centre Regional d'Archéologie d'Alet. Institut Culturel de Bretagne. Skol Uhel Ar Vro.

Tomezzoli, G., & Marzin, Y. (2015). The Ero Vili and the Atlantic Wall. *Advances in Anthropology, 5,* 183-204. https://doi.org/10.4236/aa.2015.54018

Tomezzoli, G. (2006). Die deutschen Befestingungen in den Dünen von Kéréma/Ker Emma. *DAWA Nachrichten, 48, 56-66*.

Tomezzoli, G. T., & Colliou, S. (2017). The WW II Saint-Pabu German Radar Camp and the Stützpunkte Re 03, Re 04. *Archaeological Discovery, 5,* 142-162.
https://doi.org/10.4236/ad.2017.53009

Tomezzoli, G. T. (2016). The German Defence System of the Grève de Goulven (Finistère FR) during the World War II. *Archaeological Discovery, 4,* 170-199.
https://doi.org/10.4236/ad.2016.44012

Tomezzoli, G. T. (2017a). The German Radar Surveillance around the Aber Wrach during the WW II. *Archaeological Discovery, 5,* 22-41.
https://doi.org/10.4236/ad.2017.51002

Tomezzoli, G. T. (2017b). The WW II German Coastal Artillery Battery H.K.B. 1274/StP C 342 at Camaret sur Mer (Finistère FR). *Archaeological Discovery, 5,* 116-141.
https://doi.org/10.4236/ad.2017.53008

Tomezzoli, G. T. (2017c). The WWII German Heavy Artillery Battery AV 67 of CleusFoz (Finistère FR). *Archaeological Discovery, 5,* 61-78.
https://doi.org/10.4236/ad.2017.52004

Appendix. R505 Bunker Plan (Courtesy Fleuridas P.)

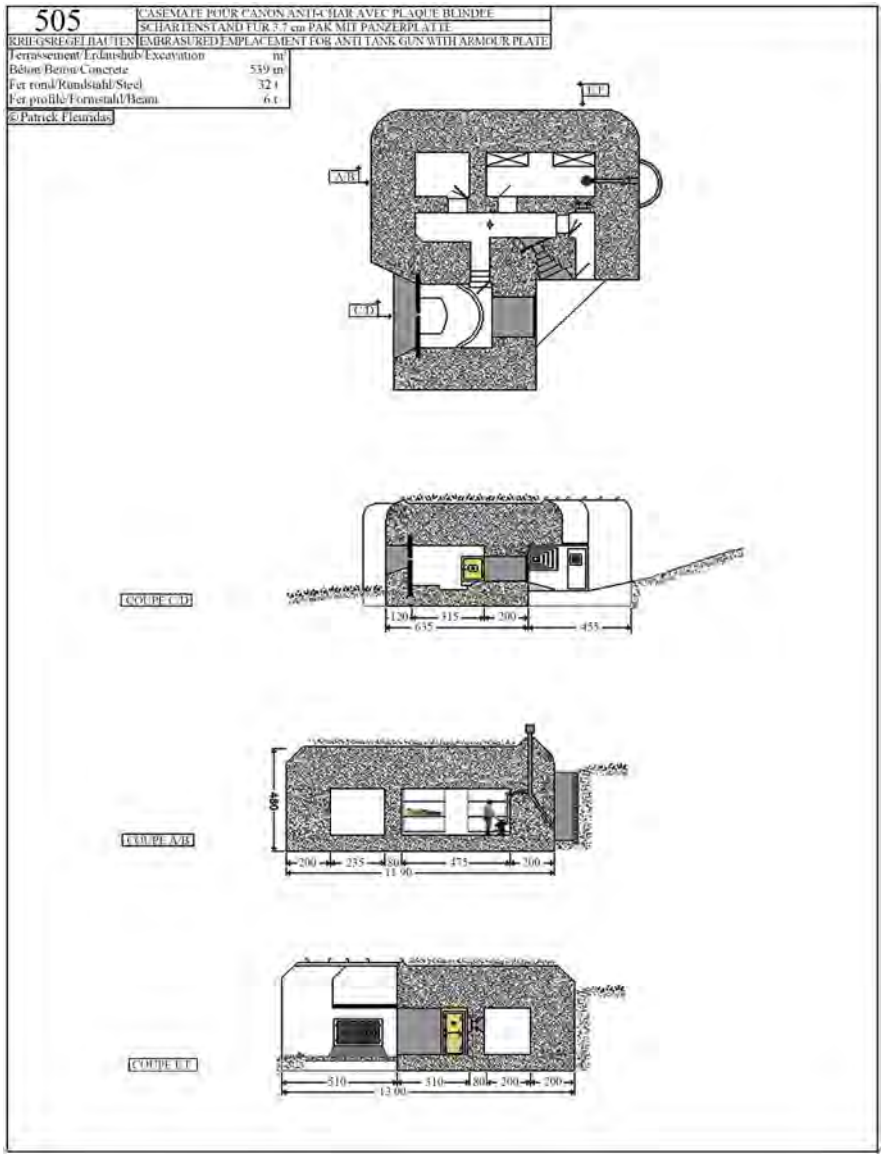

Archaeological Discovery, 2020, 8, 245-259
https://www.scirp.org/journal/ad
ISSN Online: 2331-1967
ISSN Print: 2331-1959

Locations of Cinnabar-Mercury Occurrences in Peru: Implications for Pre-Contact Gold Production

William E. Brooks

Geologist, Reston, VA, USA
Email: webgeology@aim.com

How to cite this paper: Brooks, W. E. (2020). Locations of Cinnabar-Mercury Occurrences in Peru: Implications for Pre-Contact Gold Production. *Archaeological Discovery, 8,* 245-259.
https://doi.org/10.4236/ad.2020.83014

Received: May 28, 2020
Accepted: June 26, 2020
Published: June 29, 2020

Abstract

The Huancavelica cinnabar-mercury occurrence is the most well-known, but not the only, cinnabar-mercury occurrence in Peru. Therefore, a compilation of the approximately 20 other cinnabar-mercury occurrences is important in assessing the regional availability of this important mineral and its industrial uses in pre-contact Peru. These include: 1) cinnabar use as an ancient red pigment and, 2) more importantly, retorting cinnabar was an important source of mercury that was used for pre-contact alluvial gold amalgamation and, later Colonial silver amalgamation. Geochemical sampling of the lesser-known Chonta occurrence also indicates Ag, Pb-Zn, or Au exploration targets. Retorting cinnabar has been widely documented and dates to 8000 years ago in ancient Turkey; during Roman time; in ancient Mexico; medieval Europe; the western US; and Indonesia. Using only cinnabar, clay for the ceramic retorts, and charcoal, coal, or other fuels, this artisanal process provided the mercury that was essential to the small-scale gold mining technology that produced tons of gold from alluvial sources before the arrival of the Spanish explorers in ancient South America. In present-day Peru, mercury is used to produce tons of gold from small-scale mines, and by analogy, the tons of gold produced in pre-contact Peru are hard evidence that is consistent with small-scale gold mining and mercury amalgamation in the past.

Keywords

Cinnabar, Mercury, Retort, Amalgamation, Andes

1. Introduction

Cinnabar (HgS) is an important mineral with two important uses in the ancient world: 1) it can be selectively ground and used as a versatile red pigment for use

on murals, ceramics, and gold masks (Petersen, 1970/2010; Brooks et al., 2008) or, 2) it can be retorted to produce mercury (Cabrera la Rosa, 1954; Craddock, 1995; Brooks, 2012). Retorting cinnabar to obtain mercury has been documented more than 8000 years ago in ancient Turkey (Barnes & Bailey, 1972; Brooks et al., 2017); during Roman time (Pliny the Elder, 77AD); the Middle East (al-Hassan & Hill, 1986), in ancient Mexico (Langenscheidt, 1986); medieval Europe (Agricola, 1556/1912); and California in the 1840s (Bailey & Everhart, 1964).

The primary present-day use of mercury worldwide is for alluvial gold mining; however, other modern uses include: auto switches, batteries, chlor-alkali production, dental amalgam, and fluorescent lamps. Therefore, since cinnabar was mined and retorted for mercury in the past, it is logical to conclude that mercury would have been used for that same purpose in the past—alluvial gold mining.

An example of the importance of mercury in alluvial gold mining is indicated by the production of approximately 26,000,000 pounds (or 342,000 seventy-six pound flasks) of mercury from New Almaden and other California mercury mines that were used to amalgamate alluvial gold during the California Gold Rush in 1849 (Davis, 1957; Bailey & Everhart, 1964; Bailey et al., 1973; Lanyon & Bulmore, 1967; Alpers et al., 2005). Similarly, mercury produced from Alaskan cinnabar mines was essential to the Klondike Gold Rush in 1896 (National Park Service, 2019). Mercury is used widely today to produce gold in Colombia, Ecuador, Ghana, Peru, Venezuela, Indonesia, and many other countries. Alluvial gold was the main source of gold for ancient man and provided two-thirds of the gold ever produced (Boyle, 1979).

2. Gold Production

Gold is produced in only two ways, the oldest of which is small-scale mining of alluvial or placer gold deposits using gravity separation combined with mercury. In Peru, alluvial gold deposits are widespread and the most well-known are Marañon in northeastern Peru; Rio Huallaga in east-central Peru; and Madre de Dios in southeastern Peru (Noble & Vidal, 1994; Atlas, 1999). The sparse nuggets found in streams could easily be removed by hand; however, the ages-old method of amalgamation uses gravity separation by washing the gold-bearing sediment in a pan to produce an initial separate of black sand that includes mm-sized gold flakes (*chispitas*), magnetite, apatite, and other heavy minerals. Then mercury is added to this heavy-mineral concentrate to selectively remove, or amalgamate, only the gold. Next, the gold-mercury amalgam is burned (*refogado*) to volatilize most of the mercury leaving an anthropogenic sponge-like gold nugget that could be worked for artifact production.

Cyanide is the second method used to extract gold; however, this method only dates to the 1880s. Gold and other precious metals are removed in solution from the pulverized ore from large-scale, hard-rock porphyry (Au-Cu-Ag) mines. In

pre-contact Peru, porphyry ores would have provided a gold-copper-silver alloy (*tumbaga*), which through depletion gilding would have resulted in enhanced surficial gold (Petersen, 1970/2010).

3. Availability and Use of Mercury in the Andes

In South America, cinnabar-mercury occurrences are known in Bolivia (Ahlfeld & Schneider-Scherbina, 1964), Chile (McAllister et al., 1950), Colombia (Wilson, 1941; Lozano, 1987; Brooks, 2014), Ecuador (Truhan et al., 2005), and Peru (Arana, 1901; Garbín, 1904; Yates et al., 1955; Petersen, 1970/2010; Giles, undated). The most well-known occurrences include Huancavelica, Peru (Arana, 1901); Aranzazu (Nueva Esperanza) and El Cinabrio, Colombia (Singewald, 1950; Buitrago & Buenaventura, 1975; Brooks, 2014); and Azogues, Ecuador (Brooks, 2018).

Regarding gold production and the use of mercury in pre-contact Peru, Garcilaso de la Vega commented that "Gold was gathered by the Incas from the streams … no idea of the virtues of quicksilver" (Prescott, 1847/2005). While it is true that the gold came from alluvial sources, his conclusion regarding mercury is not supported.

Given, the wealth of gold produced in pre-contact Peru and the geological availability of cinnabar-mercury occurrences, Posnansky (1945/1957) was the first to propose the use of cinnabar as a source of mercury (*azogue*) for small-scale alluvial gold mining in the ancient Andes. Cabrera la Rosa (1954) concluded that: "*Asimismo es posible suponer que los peruanos de aquellas tierras conocián, ya en épocas remotas, el método de la amalgamación, empleando para ello el azogue que lograban obtener del cinabrio cuyas menas existián en Buldibuyo*". Larco Hoyle (2001) also concluded that "…*el beneficio de oro es todavía primitivo … incluyendo el empleo del azogue, que fue usado desde muy remota antigüedad*". Ravines (1978) refined Cabrera la Rosa's Buldibuyo location and indicated that "…*azogue se encuentra en Buldibuyo al pie del gran nevado de Pelagatos*". Petersen (1970/2010) said that "…data suggest that mercury was retorted from cinnabar". And, by using modern analytical methods, Brooks et al. (2013) showed that comparable low levels of mercury in ICP (Inductively Coupled Plasma) analyses of pre-contact gold artifacts and modern *refogado* gold, where mercury is used, are consistent with mercury amalgamation of alluvial gold in the past.

The tons of gold produced in pre-contact Peru is hard evidence that is consistent with these assertions, and even today, Peru produces approximately 1.5 tons of gold per month from small-scale alluvial gold mines that use the same, ages-old rudimentary technique of mercury amalgamation of mm-sized alluvial gold (Cánepa, 2005; Brooks et al., 2007; Chauvin, 2018). During 2007-2011, Peru produced 16 - 22 tons of gold from small-scale alluvial gold mines, mainly in Madre de Dios, using mercury (Gurmendi, 2012).

Retorting and the use of mercury in ancient Peru may also be inferred from

warnings regarding the toxic fumes released during the *refogado* process and effects on human health (Larco Hoyle, 2001), as well as the Quechua word *llimpi* which means mercury (Petersen, 1970/2010). In ancient through-to-modern time in Peru and elsewhere, the primary use of mercury is for small-scale alluvial gold mining.

4. Map Compilation

Huancavelica is the most well-known cinnabar-mercury occurrence in Peru (Arana, 1901; Whitaker, 1941; Yates et al., 1955; Brown, 2001) followed by the lesser-known Chonta-Queropalca occurrences (Garbín, 1904; Deustua, 2010). Therefore, a map showing these and other occurrences is basic to understanding the regional availability of this mineral resource, whether used for pigments or as a source of cinnabar for retorting mercury. Peruvian mineral resource maps were available for gold, copper, silver, and lead-zinc occurrences, but not cinnabar-mercury (Atlas, 1999); however, approximately 20 occurrences are given in Petersen (1970/2010). Many of these occurrences might be called districts because they include numerous mines and workings, such as the 10 mines at Chonta and the 15 mines at Queropalca (Garbín, 1904). And, in most cases, since only geographic names were given, and not latitude and longitude, the locations of these occurrences are approximate. These locations were compiled along with data from additional reports, some unpublished, and maps (Vercelli et al., 1977; Cobbing et al., 1996) from the Instituto Geológico Minero y Metalúrgico (INGEMMET) library in Lima (**Figure 1**).

The term "occurrence" is used herein to broadly indicate any geochemical anomaly of the mineral and includes mines as well. Many of the occurrences may indeed have been ancient mines for pigments or mercury but they have been obscured or overprinted by modern mining. There is no present-day primary mercury production in Peru from the occurrences given in **Figure 1**. However, mercury is produced as a byproduct from porphyry copper-gold mines such as Pierina and Yanacocha and, because of environmental considerations, this byproduct mercury is exported for treatment and retirement (Brooks et al., 2007).

Buldibuyo/Pelagatos/Pampas (2) site visit—Cabrera la Rosa (1954) indicated a cinnabar occurrence near Buldibuyo. Examination of the geologic report for the area did not list a mercury occurrence (Balarezo, undated); however, the report by Ravines (1978) did include "Buldibuyo" as being near Pelagatos in central Peru, and near the village of Pampas. This occurrence is important given the specific geographic reference provided by both Cabrera la Rosa (1954) and Ravines (1978). Additionally, it is near Pataz where pre-Inca and Inca alluvial gold production has been documented (Zarate, 2006). In **Figure 1**, this occurrence is indicated as Buldibuyo/Pelagatos/Pampas.

After leaving Pampas along a road paralleling Lago Pelagatos, cinnabar samples were taken at a fault with abundant rusty water and pyrite. An outcrop with cinnabar was found along this northwest-trending fault that extended for several

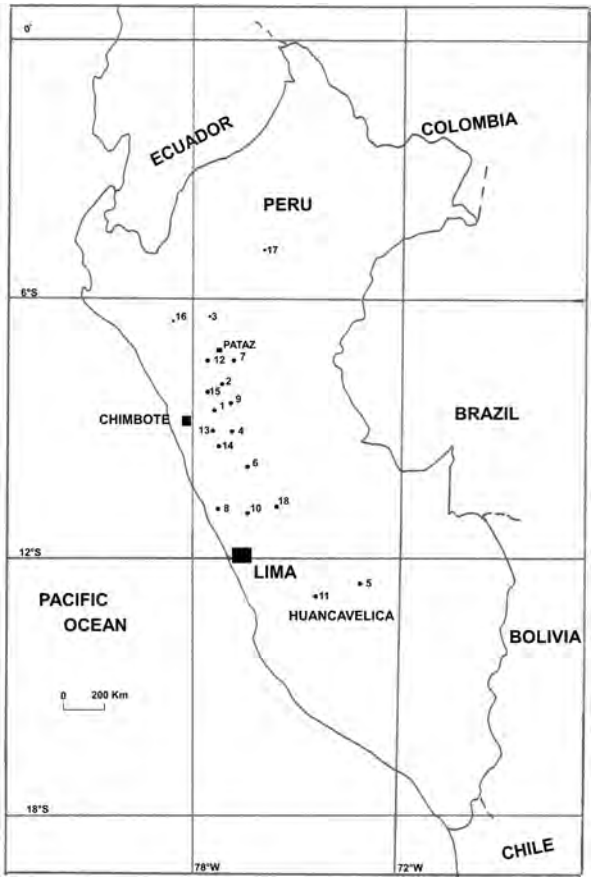

Figure 1. Approximate* locations of cinnabar-mercury occurrences in Peru. 1) Baños de Jesus (Baños Termales de Monterrey?), 9˚32'S/77˚32'W (Ravines, 1978); 2) Buldibuyo/Pelagatos/Pampas, 8˚07'S/77˚23'W (Cabrera La Rosa, 1954; Ravines, 1978); 3) Chachapoyas (Sonche?), 6˚13'S/77˚52'W (Bolétin, 1900; Petersen, 1970/2010; Ravines, 1978; Deustua, 2010). "*Pinturas rupestre de Pollurua … color rojo ocre*" may indicate the use of cinnabar pigment; 4) Chonta/Huallaca/Queropalca, 12˚38'S/74˚26'W (Petersen 1970/2010; more than 15 named mines are noted at Queropalca by Garbín, 1904; Giles, undated); 5) Chuschi, 13˚35'S/74˚21'W (Petersen, 1970/2010); 6) Cuipan/Cuypan/Quipan, 10˚30'S/76˚29'W (INGEMMET, 1999; cinnabar was taken from "*bocaminas y socavones antiguos*" at Cuipan which is ~30 km northwest from Cerro de Pasco, Garbín, 1904; Giles, undated); 7) Huacrachuco, 8˚30'S/77˚04'W (Petersen, 1970/2010); 8) Huara, 11˚06'S/77˚36'W (Giles, undated); 9) Huaraz, 9˚31'S/77˚31'W (Petersen, 1970/2010); 10) Huarochiri, 11˚50'S/76˚22'W (Petersen, 1970/2010); 11) Huancavelica/Villa Rica de Oropesa/Santa Barbara, 12˚47'S/74˚54'W (Arana, 1901; Yates et al., 1955; Petersen, 1970/2010; Brown, 2001; locations and descriptions of other mines and prospects in the region that include: Camarada, Excelsior, Carniceria, Azulcocha, Chaqa Oreco/Ventanilla 7, Huajoto, Torres Orgo, San Antonio, and Pequeña are given in INGEMMET, 1999); 12) Paccha, 7˚59'S/77˚42'W (Petersen, 1970/2010); 13) Pampas, 9˚40'S/77˚49'W (Petersen, 1970/2010); 14) Punabamba, 9˚31'S/77˚31'W (Petersen, 1970/2010); 15) Santa, 9˚04'S/78˚35'W (Petersen, 1970/2010); 16) Santa Apolonia, 7˚09'S/78˚31'W (Petersen, 1970/2010); 17) Santa Cruz, 5˚33'S/75˚48'W (Petersen, 1970/2010); 18) Yauli, 11˚40'S/76˚05'W (Petersen, 1970/2010); The following occurrences are not shown on the map: 19) Azoguine, 15˚45'S/70˚01'W (INGEMMET, 1999); 20) Carachugo/Cajamarca, 7˚09'S/78˚30'W (INGEMMET, 1999); 21) Cangallo/Minascucho/Chauschi, 13˚37'S/74˚08'W (INGEMMET, 1999). *All locations are approximate and are based on information given in the references cited.

kilometers (Figure 2). The fault was iron-stained and rusty water drained from the fault. Pyrite was also found along the fault and decomposition of the pyrite is the likely source of the rusty water. Two samples contained 24 - 82 ppm mercury (Table 1) and are well above the crustal average of <0.08 ppm for mercury (Turekian & Wedepohl, 1961). Tungsten and other large-scale mining in the area limited further access and likely eliminated or overprinted any traces of ancient mines.

Table 1. ICP data for reconnaisance of Pelagatos and Chonta cinnabar-mercury occurrences, Peru.

	PE181	PE182	PE191	PE192	PE193	PE194	PE196	PE197
Au (0.003)	0.008	0.007	0.01	0.004	0.006	0.018	0.072	0.010
Ag (0.2)	<0.2	<0.2	7.6	24.9	10	18.8	24.6	199
As (2.0)	27	7	2002	2178	87	84	824	6391
Ca (100.0)	3948	13165	199	263	<100	<100	446	<100
Cd (0.5)	<0.5	<0.5	0.9	0.7	<0.5	<0.5	0.6	<109.8
Cr (1.0)	563	237	16	14	11	16	21	4
Cu (1.0)	11	14	34	28	20	23	44	97
Fe (100)	14,306	6029	175,434	76,827	350,000	114,282	37,609	335,325
Hg (0.5)	82.9	24.9	13.1	11.9	10.7	>1000	>1000	93.6
La (10)	<10	<10	<10	<10	<10	<10	<10	<10
Mg (100.0)	2759	3483	154	116	<100	102	232	<100
Mn (5.0)	108	51	56	89	43	109	102	24
Mo (1.0)	4	1	2	3	<1	2	2	<1
Ni (1.0)	15	20	5	8	5	9	12	6
P (10)	295	105	565	216	22	25	76	17
Pb (3.0)	37	5	4016	6394	665	370	134	15,535
S (100)	904	244	6928	7619	>100,000	>100,000	31,977	>100,000
Sb (3.0)	6	3	174	248	77	23	21	367
Se (5.0)	<5	<5	<5	<5	<5	<5	<5	199
Th (10.0)	<10	<10	<10	<10	<10	<10	<10	<10
Tl (5.0)	<5	<5	<5	<5	<5	<5	<5	<5
U (8.0)	<8	<8	<8	<8	20	<8	<8	17
V (1.0)	<1	7	73	47	1	2	2	<1
W (3.0)	<3	<3	<3	<3	<3	<3	<3	<3
Zn (1.0)	5	5	339	201	36	31	72	9503

Multi-element ICP analyses in parts per million (detection limit given to right of element, in parentheses, Au-fire-assay); American Assay, Sparks, NV [ICP-2A024-Pelagatos SP0124038; ChontaSP0130401]. Sample Descriptions: PE181 [0192625/9095652 UTM] Pelagatos, dark fg quartzite, spot sample along road parallel to lake, cinnabar exposed along N 30˚E fault in roadcut, abundant pyrite and Fe-stained water; PE182 [0192625/9095652 UTM] Pelagatos, dark fg quartzite, area sample along road parallel to lake, cinnabar exposed along N 30˚ fault in roadcut, abundant pyrite and Fe-stained water; PE191 [298130/8883304 UTM] Chonta, altered, quartzite, clay, along road at first main adit, area sample of 20 m wide breccia zone, altered with Fe stain; PE192 [298130/8883304 UTM] Chonta, at adit, area sample, vuggy, Fe stain; PE193 [298130/8883304 UTM] Chonta, at adit, float sample, dark, with pyrite; PE194 [738108/4293829 UTM] Chonta, quartzite, mine waste, with cinnabar on surface; PE196 [738108/4293829 UTM] Chonta, roadside, spot sample with cinnabar and pyrite; PE197[738108/4293829 UTM] Chonta, at mine near plant, spot sample with abundant pyrite.

Figure 2. Samples of cinnabar were taken at northeast-trending fault along road that parallels Lago Pelagatos.

Chonta/Huallaca/Queropalca (4) site visit—The Chonta and Queropalca occurrences (Garbín, 1904; Giles, undated) may be accessed by a well-marked dirt road from Huallanca, to La Unión, and Baños. These occurrences were supposedly discovered upon orders from Spain in 1756 to find new sources of mercury to be used for Colonial silver amalgamation. However, it is very likely that these cinnabar-mercury occurrences were first known to pre-Inca people as a source of pigment as well as native mercury—early use of cinnabar as a red pigment by the Ohlone people in California led to the "discovery" of the New Almaden mercury mines in California by Spanish explorers (Lanyon & Bulmore, 1967; Boulland & Boudreault, 2006).

In the 1840s, there were over 2000 miners and more than 20 individual mines in the Chonta-Queropalca district (**Figure 3**). There were 11 retorts; fuels included locally available coal, peat, and a grass called *ichu*; and water for condensers came from a nearby lagoon, Chonta Cocha. The mines produced 8 - 10 flasks (one flask contains ~76 pounds of mercury) of mercury per day. "*Trabajos antiguos*" may possibly indicate pre-contact mining; however, it is unclear as to the location or how old these workings might be. Similarly "*bocaminas y socavones antiguos*" may indicate pre-contact mining at the nearby Cuipan cinnabar occurrence (Garbín, 1904; Giles, undated). Chonta closed in 1843, however, not because the ore was exhausted, but because of opportunities for miners willing to immigrate and work at the mercury mines at New Almaden, California (Garbín, 1904; Giles, undated). This New Almaden mercury would be used for the California Gold Rush.

Minerals at the mines were hosted in quartzite and sedimentary rocks and include pyrite, sphalerite, galena, cinnabar, native mercury, and silver in mainly NS structures. Even the mine waste still contained silver and mercury and the grass roofs of the buildings collected droplets of mercury lost during retorting (Garbín, 1904). Some of the buildings still remain (**Figure 4**).

Figure 3. Mine entrance at Chonta, note vertical structure to right of entry.

Figure 4. Buildings and tailings at Chonta, ground chimney and stack to right.

Samples from Chonta for this reconnaissance contained > 1000 ppm mercury; 10 - 199 ppm silver; 84 - 6391 ppm arsenic; 21 - 367 ppm antimony, and 31 - 9503 ppm zinc. Gold values are 0.01 - 0.07 ppm, but may increase with depth (**Table 1**). These elements are all above background and indicate further study focused on silver and gold in association with mercury (Turekian & Wedepohl, 1961; Noble & Vidal, 1990). Specifically, the high arsenic is a pathfinder for gold and the high mercury content is an indicator of lead-zinc-silver ore (Rose et al., 1979).

Queropalca was not visited for this study; however, numerous mercury mines were reported by Garbín (1904). Exploration drilling at Queropalca indicated several meters of gold-silver mineralization with values as high as 10 ppm gold, 1500 ppm silver, and 0.35% lead (mercury was not reported) (Candente Gold Corp., 2009). Veins and stockwork are hosted in quartzite. A hot-spring was mapped in the study area and this permits consideration of a hot-spring Au-Ag

exploration model for the district, especially given the high antimony and arsenic at Chonta (Berger, 1986; Candente Gold Corp., 2009).

Mercury was not produced at Huallanca, however, there are several large-scale mines at present-day Huallanca where mining dates to 1721. Originally production was from three veins that produced gold, silver, and copper. Pyrite, chalcopyrite, sphalerite, and copper minerals are reported from well-named mines such as Komstock and Eureka (Garbín, 1904).

5. Retorting Mercury from Cinnabar

Retorting mercury is a straightforward process and requires cinnabar ore, retorts, fuel, and a condenser to trap and cool the volatilized mercury vapors. The oldest mercury retort dates to 8000 years ago in the ancient Konya mercury district in Turkey. It consisted of a large block of marble upon which the ore was placed along with charcoal fuel. A large clay bowl over the fire cooled and condensed the mercury vapors while allowing the sulfur to escape through a chimney comprised of ceramic tubes (Barnes & Bailey, 1972). Other retorts include rows of double ceramic pots shown in Agricola's De Re Metallica (1556/1912, Book IX: p. 427) and a pre-contact double-ceramic mercury retort from Sierra Gorda, Queretaro, Mexico (Langenscheidt, 1986) where there are many ancient cinnabar mines and retorting mercury dates to the 10th century BC (Consejo de Recursos Minerales, 1992). Descriptions and sketches of a variety of mercury retorts from China, Germany, and Mexico were compiled by Craddock (1995). Ancient mercury retorts are known at Huancavelica (Rivero & Tschudi, 1853) and at Chonta, a chimney and buildings that housed retorts and condensers in the 1840s remain (**Figure 4**).

At New Almaden, California the first retorts consisted of whaling oil-try pots that were inverted over the cinnabar ore, sealed, and then fired with wood. The cinnabar inside the metal pot was heated, the mercury volatilized, the vapors cooled and condensed, resulting in mercury (Boulland & Boudreault, 2006). In Indonesia, up to a ton of mercury can be produced daily, using locally available cinnabar, from a simple, backyard wood-fired retort. This mercury is then sold directly to local small-scale gold miners or exported (Paddock, 2019).

Therefore, given the geological evidence for the regional availability of cinnabar-mercury occurrences and the widespread use of mercury for gold amalgamation in the past that continues to the present, it remains only to show how cinnabar could easily be retorted to obtain mercury using materials readily available in the ancient world. Therefore, a simple retort was modeled from the racks of double-ceramic retorts shown in Agricola's De Re Metallica (1556/1912, Book IX: p. 427) and a pre-contact double-ceramic mercury retort from Sierra Gorda, Queretaro, Mexico (Langenscheidt, 1986). This rudimentary process does not produce vermilion, only a sooty mercury-rich residue, and metallic mercury (**Figures 5-8**) that would have been collected and then used for ancient small-scale alluvial gold mining.

Figure 5. Cinnabar ore (~50 g).

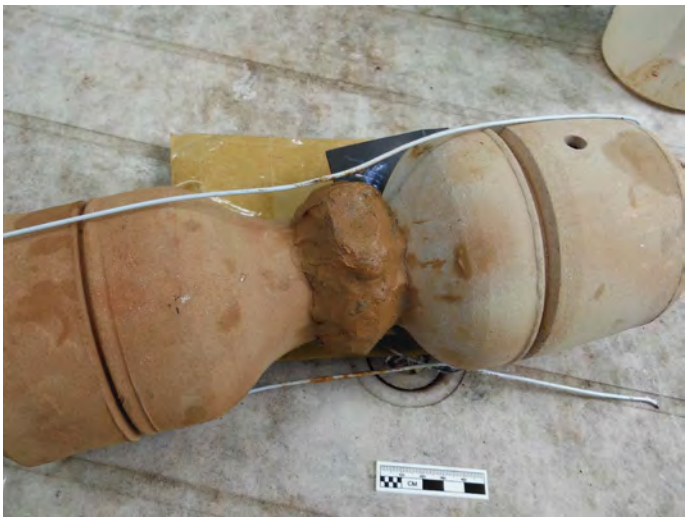

Figure 6. Double-ceramic retort with clay seal, vent to right.

Figure 7. Retort in place with charcoal fuel (~600˚F).

Figure 8. Mercury droplets in black mercury-rich residue along rim of ceramic retort. This black sooty residue in the retorts at New Almaden was scraped and removed to obtain additional mercury (Boulland & Boudreault, 2006).

6. Conclusion

This compilation of cinnabar-mercury occurrences is important to the ongoing evaluation of the use of mineral resources in the ancient Andes. Huancavelica remains the most well-known occurrence, now followed by Chonta-Queropalca. The availability of cinnabar-mercury is especially applicable to the study of cinnabar sources and their uses, specifically as a source of red pigment and as a source of ore for mercury. Of these, the use of mercury for gold amalgamation helps to explain the technology that resulted in the incredible gold production that took place in ancient Peru before the arrival of the Europeans. In addition to ancient cinnabar mining at Huancavelica, there are suggestions of ancient workings at Chonta-Queropalca and Cuipan as well as evidence for pre-Inca gold mining at Pataz.

Native mercury was available, for example at Huancavelica or Chonta; however, retorting cinnabar was a relatively simple process that dates to ancient times. In Peru, retorting would have utilized readily available materials such as cinnabar ore, clay for ceramic retorts, water for cooling, and fuel such as wood, coal, or grass. Much as mercury is used today in Peru's small-scale alluvial gold mines in Madre de Dios or Marañon, in the past, mercury would have been sourced from the numerous cinnabar occurrences in Peru, retorted, and used for pre-contact gold production.

Acknowledgements

Sincere thanks are expressed to INGEMMET and especially to Sr. Rolando Moreno, director of the INGEMMET library, in Lima for providing maps and geologic reports on mercury in Peru.

VIDEO Links

How to extract mercury from the cinnabar (singarf) para Rasmani
https://www.youtube.com/watch?v=3e9WrJSxrV4\
Rasamani Preparation Siddhar Methods Valairasam Using Lingam Pashanam
https://www.youtube.com/watch?v=L5qIMjSwkJU

Conflicts of Interest

The author declares no conflicts of interest regarding the publication of this paper.

References

Agricola (1556/1912). *De Re Metallica* (638 p.). Trans. H. C. Hoover &H. L. Hoover, NY: Kessinger Publishing.

Ahlfeld, F., & Schneider-Scherbina, A. (1964). *Los Yacimientos Minerales y De Hidrocarburos de Bolivia* (388 p). La Paz, Ministerio de Minas y Petroleo, Departamento Nacional de Geología, Boletin No. 5 (Especial).

al-Hassan, A. Y., & Hill, D. R. (1986). *Islamic Technology: An Illustrated History* (304 p). Cambridge: Cambridge University Press.

Alpers, C. N., Hunerlach, M. P., May, J. T., & Hothem, R. L. (2005). *Mercury Contamination from Historical Gold Mining in California.* U.S. Geological Survey Fact Sheet 2005-3014. https://doi.org/10.3133/fs20053014

Arana, P. P. (1901). *Las Minas de Azogue del Perú* (109 p). Lima: Imprenta El Lucero.

Atlas (1999). *Atlas of Mineria y Energía en el Peru* (111 p.). Hokama, D., Ed., Lima: Ministerio de Energía y Minas.

Bailey, E. H., & Everhart, D. L. (1964). *Geology and Quicksilver Deposits of the New Almaden District, Santa Clara County, California* (206 p). U.S. Geological Survey Professional Paper 360. https://doi.org/10.3133/pp360

Bailey, E. H., Clark, A. L., & Smith, R. H. (1973). Mercury. In D. A. Brobst, & W. P. Pratt (Eds.), *United States Mineral Resources, U.S. Geological Survey Professional Paper 820* (pp. 401-414).

Balarezo, A. (undated). *Croquis de Ubicación de Las Zonas Mineras de Parcoy y Buldibuyo.* Lima: Cooperación Minera Peruano Alemana, INGEMMET Archivo Tecnico, Codigo CG1794, scale 1:1,000,000.

Barnes, J. W., & Bailey, E. H. (1972). Turkey's Major Mercury Mine Today and How It was Mined 8000 Years Ago. *World Mining, 25,* 49-55.

Berger, B. R. (1986). *Descriptive Model of Hot Spring Au-Ag, Model 25a.* In D. P. Cox, & D. A. Singer (Eds.), *Mineral Deposit Models, U.S. Geological Survey Bulletin 1693*.

Bolétin (1900). Itinerario de los Viajes de Raimondi en el Perú. *Bolétin de la Sociedad Geográfica de Lima, 10,* 1-40.

Boulland, M., & Boudreault, A. (2006). *New Almaden* (225 p). Charleston, SC: Arcadia Publishing.

Boyle, R. W. (1979). The Geochemistry of Gold and Its Deposits. *Canadian Geological Survey Bulletin, 280,* 584 p.

Brooks, W. E., Ozturk, H., & Cansu, Z. (2017). Amalgamation and Small-Scale Gold Mining at Ancient Sardis, Turkey. *Archaeological Discovery, 5,* 42-59. https://doi.org/10.4236/ad.2017.51003

Brooks, W. E. (2012). Industrial Use of Mercury in the Ancient World, Ch. 2. In M. S. Bank (Ed.), *Mercury in the Environment: Pattern and Process* (pp. 19-24). Berkeley, CA: Harvard School of Public Health, University of California Press. https://doi.org/10.1525/california/9780520271630.003.0002

Brooks, W. E. (2014). Colombia Mercury Inventory. *Geología Colombiana, 37,* 15-50.

Brooks, W. E. (2018). ICP Analyses from the Cinnabar-Mercury Occurrence at Azogues (Loma Guashon), Ecuador: Ancient Industrial Uses and Human Health Implications. *Archaeological Discovery, 6,* 38-51. https://doi.org/10.4236/ad.2018.61003

Brooks, W. E., Piminchumo, V., Suarez, H., Jackson, J. C., & McGeehin, J. P. (2008). Mineral Pigments from Huaca Tacaynamo (Chan Chan, Peru). *Bulletin de l'Institut Francais d'Études Andines, 37,* 441-450. https://doi.org/10.4000/bifea.2957

Brooks, W. E., Sandoval, E., Yepez, M., & Howard, H. (2007). *Peru Mercury Inventory 2006.* U.S. Geological Survey Open-File Report 2007-1252. https://doi.org/10.3133/ofr20071252

Brooks, W. E., Schwörbel, G., & Castillo, L. E. (2013). Amalgamation and Small-Scale Gold Mining in the Ancient Andes, Ch. 10. In N. Tripcevich, & K. J. Vaughn (Eds.), *Mining and Quarrying in the Ancient Andes, Interdisciplinary Contributions to Archaeology* (pp. 213-229). New York: Springer Publishing. https://doi.org/10.1007/978-1-4614-5200-3_10

Brown, K. W. (2001). Workers' Health and Colonial Mercury Mining at Huancavelica, Peru. *The Americas, 57,* 467-496. https://doi.org/10.1353/tam.2001.0030

Buitrago, C. J., & Buenaventura, J. (1975). *Ocurrencias minerales en la región central del departmento del Tolima* (837 p). Bogotá: INGEOMINAS Informe 1672.

Cabrera la Rosa, A. (1954). Asimismo, es possible suponer que los peruanos de aquellas tierras conocián, ya en épocas remotas, el método de la amalgamación, empleando para ello el *azogue* que lograban obtener del cinabrio cuyas menas existián en Buldibuyo [Therefore, It Is Possible That the Peruvians from Those Areas Knew, in Ancient Time, the Method of Amalgamation, Using Azogue/Mercury That Was Obtained from Cinnabar Ores at Buldibuyo]. *Situación Actual de la Minería del Mercurio en el Perú*, Minería y Metalurgia, Madrid, 3-12.

Candente Gold Corp. (2009). *Candente Gold Corporation Presentation.* Vancouver, Canada: Candente Gold Corp. https://www.candentecopper.com/site/assets/files/5197/goldpropertiesapril2009.pdf

Cánepa, C. (2005). *Minería a pequeña escala en la Costa Sur Media del Perú* (62 p). INGEMMET Boletín 3, Lima: Instituto Geológico Minero y Metalúrgico.

Chauvin, L. (2018). *Pope Brings His Environmental Crusade to Peru.* Washington Post, 20 January, A8.

Cobbing, J., Sanchez, A., Martinez, W., & Zarate, H. (1996). *Geologia de los Quadrangulos de Huaraz, Recuay, La Union, Chiquian y Yanahuanca.* INGEMMET Boletin n. 76, Serie A, Lima: Carta Geologica Nacional.

Consejo de Recursos Minerales (1992). *Geological-Mining Monograph of the State of Queretaro* (108 p). Mexico, D.F.: Consejo de Recursos Minerales, Secretaria de Energia, Minas e Industria.

Craddock, P. T. (1995). *Early Metal Mining and Production* (363 p). Washington DC: Smithsonian Institution Press.

Davis, F. F. (1957). Mercury. In L. A. Wright (Ed.), *Mineral Commodities of California: California Division of Mines Bulletin 176* (pp. 341-356).

Deustua, J. E. (2010). Mercury (Not Always Rising) and the Social Economy of Nineteenth-

Century Peru. *Economía (Pontificia Universidad Católica del Perú. Departamento de Economía), 33,* 128-153. http://www.researchgate.net

Garbín, L. (1904). Apuntes Sobre los Minerales de Huallanca, Chonta y Queropalca. *Boletin de la Sociedad de Ingenieros, VI,* 1-17.

Giles, C. F. (undated). *Minas de Mercurio Conocidas en el Peru* (3 p). Lima, Peru: INGEMMET Archivo Tecnico, Codigo 9921.

Gurmendi, A. C. (2012). *The Mineral Industry of Peru*. U.S. Geological Survey 2012 Minerals Yearbook. https://minerals.usgs.gov/minerals/pubs/country/2012/myb3-2012-peru.pdf

INGEMMET (1999). *Mercurio*. INGEMMET Archivo Tecnico, Codigo AO993.

Langenscheidt, A. (1986). *Historia Minima de la Minería en la Sierra Gorda, Queretaro, Mexico* (pp. 24-29). *Mineroamérica*, abril, Mexico, D.F.

Lanyon, M., & Bulmore, L. (1967). *Cinnabar Hills, the Quicksilver Days of New Almaden* (128 p). Los Gatos, CA: Village Printers.

Larco Hoyle, R. (2001). *Los Mochicas, tomo II* (350 p). Lima, Perú: Museo Arqueologíco Rafael Larco Herrera, Pueblo Libre.

Lozano, H. (1987). *Minerales de Mercurio*. Publicacciones Especial de Ingeominas, No. 1, Bogota, Colombia, 275-293.

McAllister, J. F., Flores, H., & Ruiz, C. (1950). *Quicksilver Deposits of Chile* (69 p). U.S. Geological Survey Bulletin 964-E.

National Park Service (2019). *Metals of the Gold Rush*. National Park Service. https://www.nps.gov/klse/learn/nature/geology.htm

Noble, D. C., & Vidal, C. E. (1990). Association of Silver with Mercury, Arsenic, and Antimony at the Huancavelica District, Peru. *Economic Geology, 85,* 1645-1650. https://doi.org/10.2113/gsecongeo.85.7.1645

Noble, D. C., & Vidal, C. E. (1994). *Gold in Peru*. Society of Economic Geologists, SEG Newsletter, No. 17, 1-13.

Paddock, R. C. (2019). *The Hidden Cost of Gold*. New York Times, 9 November. https://www.nytimes.com/2019/11/09/world/asia/indonesia-mercury-pollution-gold-mining.html

Petersen, G. (1970/2010). *Mining and Metallurgy in Ancient Perú* (90 p). Translation by W. E. Brooks, 2010, of Minería y Metalurgia en el Antiguo Perú, Arqueologicas 12, Museo Nacional de Antropología y Arqueología, Pueblo Libre, Lima, Perú. Geological Society of America Special Paper 467.

Posnansky, A. (1945/1957). *Tiahuanaco, La Cuna del Hombre Americano*. v. 1-II, 1945, New York; v. 3-4, Ministerio de Educación, 1957, La Paz, Bolivia.

Prescott, W. H. (1847/2005). *History of the Conquest of Peru* (537 p). Mineola, NY: Dover Publications.

Ravines, R. (1978). *Tecnología Andina* (821 p). Lima, Peru: Instituto de Estudios Peruanos, Instituto de Investigación Tecnológica Industrial y de Normas Técnicas, OCLC4263659.

Rivero, M. E., & Tschudi, J. J. (1853). *Peruvian Antiquities* (225 p). New York,.

Rose, A. W., Hawkes, H. E., & Webb, J. S. (1979). *Geochemistry in Mineral Exploration* (500 p). London: Academic Press.

Singewald, Q. E. (1950). *Mineral Resources of Colombia, Geologic Investigations in the American Republics* (pp. 151-155). U.S. Geological Survey Bulletin 964-B.

Truhan, D. L., Burton, D. L., & Bruhns, K. O. (2005). El Cinabrio en el Mundo Andino.

Revista de Antropología, 18, 193-205.

Turekian, K. K., & Wedepohl, K. H. (1961). Distribution of the Elements in Some Major Units of the Earth's Crust. *Geological Society of America Bulletin, 72,* 175-192. https://doi.org/10.1130/0016-7606(1961)72[175:DOTEIS]2.0.CO;2

Vercelli, A., Paz, M., & Huaman, A. (1977). *Reservas Minerales en el Peru en Antimonio*, *Bismuto*, *Mercurio*, *Selenio*, *Tellurio*, *e Indio.* INGEMMET Archivo Tecnico, Codigo A0717.

Whitaker, A. P. (1941). *The Huancavelica Mercury Mine* (150 p). Cambridge: Harvard University Press.

Wilson, F. (1941). Colombia. *Engineering and Mining Journal, 142,* 154-155.

Yates, R. G., Kent, D. F., & Concha, J. F. (1955). *Geology of the Huancavelica Quicksilver District*, *Peru* (45 p). U.S. Geological Survey Bulletin 975-A.

Zarate, H. (2006). *Proyecto GR5-Estudio Geológico del Batolito de Balsas-Pataz-Buldibuyo, Ocurrencias de la Mineralización en el Area de Estudio* (110 p). INGEMMET Informe A5727, Lima, Peru.

Archaeological Discovery, 2020, 8, 260-287
https://www.scirp.org/journal/ad
ISSN Online: 2331-1967
ISSN Print: 2331-1959

Petrochemistry of Sediment and Organic Materials Sampled from Ossuaries and Two Nails from the Tomb of the Family of the High Priest Caiaphas, Jerusalem

Aryeh E. Shimron[1], Yoetz Deutsch[1], Werner H. Schoch[2], Vitaly Gutkin[3]

[1]Geological Survey of Israel (Ret.), Jerusalem, Israel
[2]Labor Fur Quartere Holtzer, Langnau, Switzerland
[3]The Center for Nanoscience and Nanotechnology, The Hebrew University of Jerusalem, Jerusalem, Israel
Email: aeshimron@gmail.com

How to cite this paper: Shimron, A. E., Deutsch, Y., Schoch, W. H., & Gutkin, V. (2020). Petrochemistry of Sediment and Organic Materials Sampled from Ossuaries and Two Nails from the Tomb of the Family of the High Priest Caiaphas, Jerusalem. *Archaeological Discovery, 8,* 260-287.
https://doi.org/10.4236/ad.2020.83015

Received: June 16, 2020
Accepted: July 10, 2020
Published: July 13, 2020

Abstract

We have studied the petrochemistry of degraded bones and sediment from the interior of four ossuaries (burial boxes) discovered in what is (arguably) believed to be the 1st century CE family tomb of the high priest Caiaphas (herewith Cft) in Jerusalem. During the course of the 1990 excavation, among other artifacts (e.g., a coin found in a skull) two iron nails were discovered. One of the nails was inside an ossuary, the other on the floor of one of the nearby "kokhim" (burial niches) which contained Ossuaries 5 and 6. According to the Israel Antiquities Authority (IAA) everything in the burial cave can be accounted for today except the iron nails "*which have been misplaced*", this without being properly recorded or photographed. Investigative journalist Simcha Jacobovici believes that he has located the nails in the artifacts collection of the Anthropology laboratory at Tel Aviv University. The IAA, however, has stated that the lost nails from the Cft have nothing to do with the nails found at the university and the latter nails must have a different provenance. Wherever lies the truth, the presence of two nails in the Cft is of profound interest because in the New Testament the high priest Caiaphas was responsible for passing Jesus to the Romans who then sent him to the cross. The possibility that the nails were used in a crucifixion on the one hand and can be connected to Caiaphas the high priest on the other is, to say the least, interesting and potentially monumental. Aware of the controversy but also of the importance of the two unprovenanced nails we have investigated the materials which have invaded the interiors of the Cft ossuaries and in a similar manner materials that have adhered to the two unprovenanced nails. Em-

ploying geochemical and petrochemical Scanning Electron Microscope (SEM-EDX), X-ray diffraction (XRD) and $\delta^{18}O$ and $\delta^{13}C$ isotope analyses we have found that the organic and inorganic materials flushed into the interior of the Cft but also those that have adhered to the two unprovenanced nails possess and display many identical, and what can also be termed unique chemical and physical characteristics. *Based on the collective evidence we conclude, with considerable confidence, that the unprovenanced nails are the lost nails excavated from the Caiaphas family tomb in* 1990 *and furthermore that these nails were used in a crucifixion.*

Keywords

Jerusalem, Caiaphas Tomb Ossuaries, Crucifixion Nails, Accreted Cedar Wood, Tracheids, Microbial Infestation, Bone Degradation, Lepidocrocite, Goethite, Magnetite, Botryoids, Accretion Rims, Fungal Sporangium, Spores, Hyphae, Bone Microfabric, Yeast Cells, Trabeculae, Bacterial Biofilm, Hellenistic Period Aqueduct, SEM, XRD and $\delta^{18}O$ $\delta^{13}C$ Isotopes

1. Introduction

"*There is no proof whatsoever that those nails came from the cave of Caiaphas. There is no proof that the nails are connected to any bones, or that there is any bone residue attached to the nails. There is no proof from textual data that Caiaphas had the nails from the crucifixion with him after the crucifixion took place and after Jesus was taken down from the cross.*

(Prof. Gaby Barkai, Telegraph, UK, 12 April, 2011)."

Such lofty declarations and academic disputes pertaining to the Caiaphas family tomb and two (arguably) crucifixion nails found therein have in major part been confined to the media and scholars in the fields of archaeology, anthropology and divinity. Besides the excavators few, if any, have examined or studied the ossuaries from the Cft (Caiaphas family tomb) and certainly not the nails above, was of adequate merit to inspire the scientific efforts below. Although the route following the present endeavours is rather lengthy we trust that what we here view as an original contribution not only to scientific thought of artifacts discovered in ancient ossuaries but also to Christianity at its very earliest, do these efforts justice.

What is referred to as the Caiaphas family tomb was discovered by construction workers in 1990 in the Jerusalem neighborhood of North Talpiyot, located about halfway between ancient Jerusalem and Bethlehem (**Figure 1**). The Cft is one of three tombs located within ~200 meters and less of the Lower (Hellenistic period, 1st - 2nd century BC) aqueduct with (arguably) all displaying some evidence of early Christianity (Tabor and Jacobovici, 2012; Shimron et al., 2020). The Cft was broken into by tomb robbers, probably during the Byzantine period. Except for Ossuaries 5 and 6 which were found in their kokhim with their lids

on, all ossuaries were moved from their rock shelves (Greenhut, 1992, 2004) at this time. Ossuaries 1, 2, 3, and 4 were found whole whereas six additional ossuaries were found shattered but were later reconstructed by the Israel Antiquities Authority (IAA). A total of 12 ossuaries were removed from the tomb during the archaeological excavation. The exterior walls of five ossuaries are inscribed, and six are decorated with floral motifs, Ossuary 6 magnificently so (Greenhut, 1992, **Figure 2(b)**). The name "Caiapha" is inscribed on the latter and also on Ossuary 3. A coin of Herod Agripa 1 from the year 42 - 43 CE was discovered in the scull inside Ossuary 8, besides precisely dating the tomb it also points to the pagan custom of placing a coin between the teeth of the deceased as payment to Charon, the ferryman in Greek mythology (Toynbee, 1971) thus pointing to the usage of this pagan custom in Jewish Jerusalem during this period (Hachlili & Killebrew, 1983; Tabor & Jacobovici, 2012). Most scholars agree with the excavators that the inscribed names refer to the family of the 1st century CE Jewish high priest Kaiapha, transliterated "Caiaphas" in the New Testament.

Two iron nails were discovered during excavation of the tomb (Greenhut, 1992), one on the floor of the southern loculus (kokh IV) in which ossuaries 5 and 6 were contained, the other, according to the head excavator (Greenhut, 2004) inside Ossuary 1. Regarding the function of the nails, Rahmani (1961) suggested that nails found in tombs were used for fixing ossuary lids or for scratching the name of the deceased on an ossuary's side. This interpretation remains prevalent and is thus far the only opinion expressed in academic circles. Consequently, the official IAA statement that the nails uncovered in the tomb during its excavation were misplaced or transferred to some unknown location did not cause any clamour.

About 20 years ago, Prof. I. Hershkovitz of the Sackler School of Medicine and Anthropology laboratory at Tel Aviv University received from the IAA two small boxes. One box was clearly marked as originating from the laboratory of the late Prof. Nicu Hass; the other box, which held two nails, was unmarked and the provenance of the nails that it contained was not specified. The two boxes were stored in the laboratory's safe. A few years ago Prof. Israel Hershkovitz showed them to journalist Simcha Jacobovici who, based on his investigation of the Caiaphas family tomb finds, hypothesized that the two unprovenanced nails in the unmarked box were the missing nails from the Cft (Jacobovici, 2014). He further surmised that, given their morphology, these nails may have been used in a crucifixion and furthermore, in view of their archaeological context (tomb of the high priest Caiaphas) the crucifixion may have been that of Jesus of Nazareth. Thus far the only unambiguous physical evidence of nails used in a crucifixion is the 11.5 cm long Heel Bone nail from the crucifixion of Yehohanan Ben Hagaol discovered in a Jerusalem tomb in 1968. The gravity of these implications have led us to carry out the present in-depth scientific investigation of materials in the Caiaphas tomb ossuaries and also of the two unprovenanced nails from Prof. Hershkovitz's laboratory. Such a geochemical-petrochemical study of

provenancing materials excavated from tomb ossuaries has, to the best of our knowledge, only one precedent—our recently published study on the ossuaries and materials from the nearby Talpiot—"Jesus family" tomb (Shimron et al., 2020, and **Figure 1**).

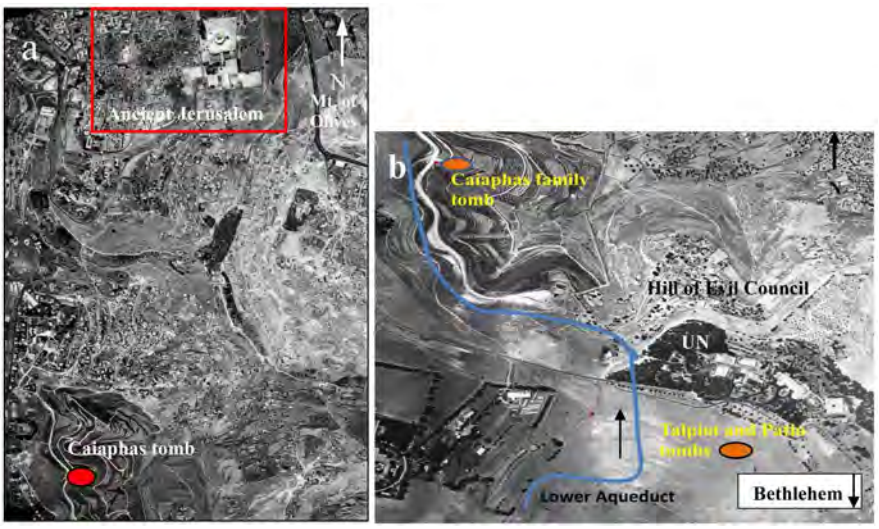

Figure 1. (a) 1970 aerial photographs showing the setting of the Caiaphas family tomb. (b) East Talpiot quarter and the biblical Hill of Evil Council (now the UN compound) neighborhood in SE Jerusalem. The Lower (Hellenistic period) aqueduct is in blue, the arrow points from the S to N direction of water flow. Photo base: Israel Mapping Center (1971).

2. Sampling and Analytical Procedures

Sampling of sediment flushed into the Caiaphas tomb ossuaries was carried out by technician Oded Reviv of the IAA. A few grams (about 1 - 2 teaspoonfuls) of loose sediment and/or fine rubble were collected from ossuaries 1, 3, 6 and 7 (a repaired ossuary) using a stainless steel spatula. Occasionally this was not feasible, in such case, sediment was scraped off from the ossuary bottom and/or ossuary walls (laminated wall crusts) with a stainless steel scalpel. Grain mounts for the scanning electron microscope (SEM) and polished and regular thin sections for study in transmitted light optical microscope were prepared from fine materials. The two unprovenanced nails were sampled in the laboratory of the Dept. of Anthropology, Tel Aviv University. This was carried out by the senior author (AES) using a specially prepared stainless steel holder on which a small diamond bit was mounted. As sampling small artifacts is a destructive process only a small amount (maximum 1/4 teaspoonful) of rusted iron and carbonate carapace could be scrapped off from the oxidized surface of each nail. These materials were studied under the petrographic and scanning electron microscope and analyzed by SEM-EDX, X-ray diffraction (XRD) and $\delta^{18}O$ and $\delta^{13}C$ isotopic analyses. Prior to the above studies, the nails were examined and photographed intact under low power SEM magnification.

X-ray diffraction analyses were done at the geochemical laboratory of the

Israel Geological Survey using a Philips XRD diffractometer with the following equipment: 1. High tension generator—PW1830 operated at tension of 40 KV and a current of 30 mA, 2. Philips MPD control—PW 3710, 3. Philips Goniometer—PW 3020, operating with a Cu long fine focus PW—2773/00 target, 4. Slit system: divergence slit—1˚, 5. CuKBß radiation was eliminated with the aid of a Philips PW 1752/00 Monochrometer. The <200 mesh ground samples were inserted in the diffractometer in a standard Philips rectangular aluminum sample holder.

Scanning Electron Microscope (SEM-EDX) analyses were carried out at the Hebrew University Nanolaboratory (The XPS Laboratory Unit for Nanocharacterization, The Harvey M. Krueger Center for Nanoscience and Nanotechnology in Jerusalem) by Dr. Vitaly Gutkin (supervisor of the unit) and AES—the senior author. The scanning electron microscopy images were obtained using an FEI Quanta 200 ESEM in low-vacuum mode without any preliminary treatment and with a chamber pressure of 0.38 Torr and acceleration voltages of 15 - 20 kV. Elemental analyses were carried using EDX (Energy Dispersive X-Ray spectroscopy). Energy Dispersive X-Ray Spectroscopy is a chemical microanalysis technique used in conjunction with SEM. The EDX technique detects X-rays emitted from the sample during bombardment by an electron beam to characterize the elemental composition of the analyzed volume. All photos used in this manuscript, unless denoted otherwise, are SEM micrographs.

Stable isotope $\delta^{18}O$ and $\delta^{13}C$ measurements were performed using a Gas Bench system attached to a Delta Plus mass spectrometer (Thermo). All $\delta^{18}O$ and $\delta^{13}C$ values were calibrated against the international standard NBS-19, and are reported in permil (‰) relative to the VPDB standard. Analytical reproducibility of duplicates is better than 0.1‰ both for $\delta^{18}O$ and $\delta^{13}C$.

3. The Caiaphas Cave Tomb Ossaries: Microstratigraphy and Microfabric

Burial tombs are cave-like features and the ossuaries therein act like small caves within a larger one. An ossuary is a box generally constructed of local stone, in Roman period Palestine soft local chalk and limestone were the favored construction materials. Ossuaries were the final resting place of human skeletal remains containing a single or occasionally more skeletons. During burial, a body was first placed on a temporary rock ledge inside the tomb from which, after about one year, the bones were removed and placed inside an ossuary. Besides the skeletal remains, natural materials inside tomb caves are weathered and disintegraded local stone to which varying amounts of soil and organic matter were subsequently contributed by the incursion of water during seasonal winter rains. Periodically, added to this mix was aerosol—a mix of wind-carried fine particles of comminuted rock (mostly well-polished quartz micro-grains) and soil with additions of local organic materials. Soils in major part develop by weathering of local bedrock, in West Jerusalem this is Turonian age limestone, dolomite and

more rarely clayey shales producing Terra Rossa soils. In South and East Jerusalem (the hill tops and eastward toward the Rift Valley) White Rendzina soils (**Table 1**, **An. 41**) overlie Senonian age chalk and chert bedrock. The specific location of the Caiaphas tomb ~50 meters directly downslope beneath the Hellenistic period Lower aqueduct, appears to have played a significant role in the geochemical evolution of the tomb and ossuaries by periodic contributions of moisture from water overflow in the aqueduct.

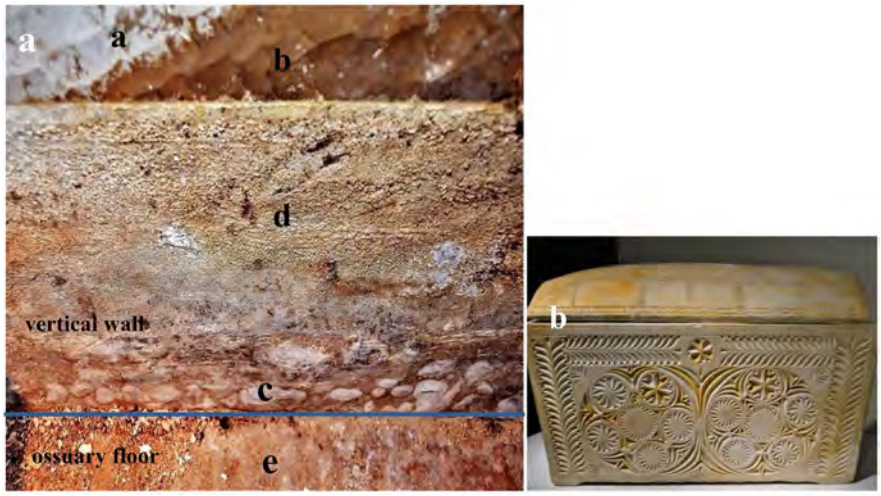

Figure 2. (a) Ossuary 6 interior vertical inner wall, showing the fine wall-parallel sedimentation laminae (a - e, details in text). (b) The inscribed and most decorated Ossuary 6, the two inscriptions—*Joseph son of Caiaphas* are on the left side and back face.

Optical microscope, and SEM examinations and eventually XRD analyses showed that much of the bone components in the ossuaries suffered degradation, micritization and recrystallization. For a climate entirely dry for about seven months of the year, more than the usual amount of moisture must have periodically entered the Cft ossuaries. This is well shown by a discreet wall and floor-parallel millimeters-thick internal lamination of fine sediment mixed with decayed bone rubble containing small amounts of other organic materials. It is particularly well manifested on the walls of Ossuary 6 (**Figure 2(a)**) as a white chalk (ossuary construction material) substratum (a) covered by a pale brown clayey soil layer (b) in turn covered by fine layers of lumpy phosphatic crusts (**c**) finally capped by a veneer of white carbonate flowstone carrying much aerosol quartzose dust (d). The vertical wall layers formed during fluctuating water level inside the ossuary and accretion onto the walls of fine sediment floating on the water interface. The ossuary floor (e) exhibits a similar horizontal micro-lamination with individual floor laminae of detritus carrying soil, micrograins of quartzose aerosol (**Figure 3(a)**), degraded bone and finally flowstone. Bone degradation was accompanied by crystallization of fluorapatite [$Ca_5(PO_4)_3F$, **Table 1**, **Figure 4**] and hydroxyapatite [$Ca_5(PO_4)_3OH$]. Small grains of anhydrite, gypsum, barite and chips of iron oxide (**Figure 3(b)**, **Table 1**, **An. 12, 16**) are also present.

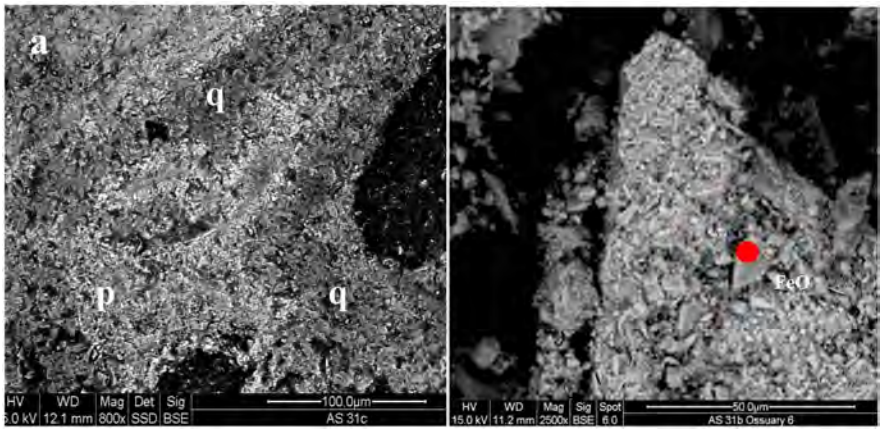

Figure 3. (a) Ossuary 6 phosphatic wall crust with quartzose lenses (dark zones—q). Light-colored internal laminae (p) are mostly degraded bone. (b) Ossuary 6 bone rubble with occasional chips of iron oxide containing up to 83.55% FeO set in a matrix of quartzose dust and decayed bone. One possible source for such FeO-rich exotic fragments is nails placed in the ossuary.

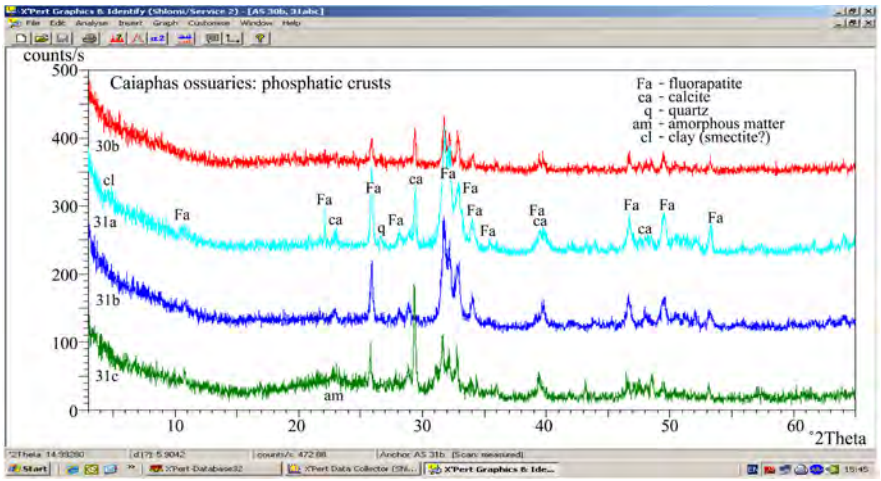

Figure 4. X-ray diffraction (XRD) mineral composition of interior wall crusts in Ossuaries 3 and 6. The phosphatic crusts laminae contain mainly fluorapatite, quartz, calcite, clay minerals and amorphous (degraded and decayed) materials.

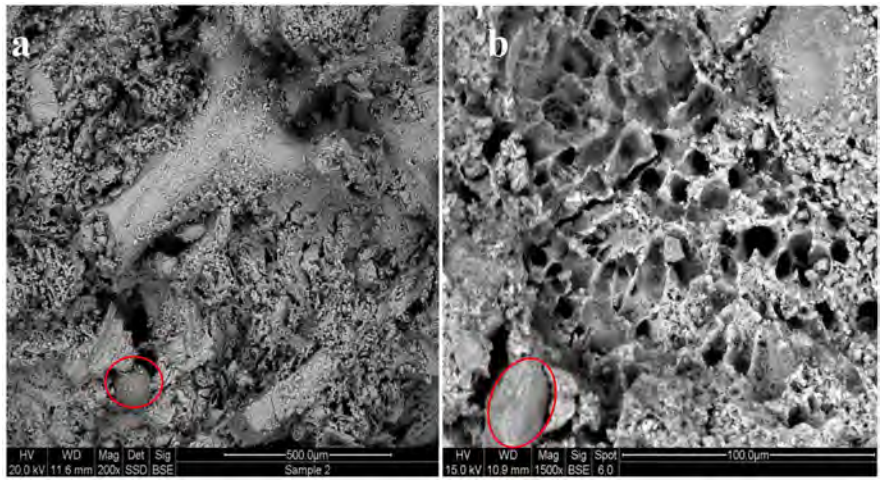

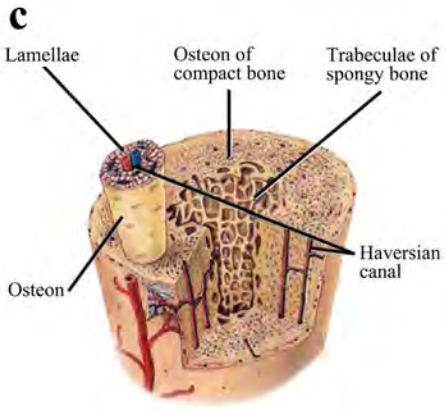

Figure 5. (a) Ossuary 6 bone rubble, the larger bone fragment is about 150 μm in diameter, it may be a tiny rod-like fragment from a trabecula. The sphere beneath (marked) seems to have a hypha opening on the top, its size (~80 μm diameter) suggests it may be a fungal sporangium (below) or fossil diatom. (b) Ossuary 1 degraded bone microstructures. The single oval grain (marked, lower left, ~50 μm long axis), is a typical aerosol quartz grain, such grains are ubiquitous in the tomb ossuaries and also adhering onto the two nails. The bone microfabric suggests this to be a fragment from a soft bone spongiosa. (c) Model of an osteon system and trabeculae of spongy bone. Source for (5c): https://training.seer.cancer.gov/anatomy/skeletal/tissue.html.

3.1. Botryoidal Microstructures

Under the optical microscope the phosphatic crusts (above) are seen as fibrous, variously degraded (optically opaque) bone tissue containing here and there discontinuous quartzose clusters and lenses (**Figure 3(a)**). The laminae are frequently packed with concentrically zoned spheres, 10 - 40 μm in diameter, seen as individuals, joined couplets or in the form of continuous films of what appear to be botryoidal forms (**Figure 6a**). The spheres consist of 3 - 4 outer concentric rings and an inner core of fibrous crystallites radiating around an opaque black carbon-rich core (**Table 1**, **An. 17, 18**). The surrounding cryptocrystalline remains of decayed bone tissue consist of fluorapatite with small amounts of fine quartz incorporated onto apatite micrograins and also as lenses and fine lamellae (**Figure 3(a)**, **Table 1**, **An. 8 - 11**). We interpret the botryoidal biofilms of adhering spheres to be the result of bone decay due to microbial infestation responsible for the chemical dissolution of bone tissue. Some bone tissue has retained its bone microfabric and osteon rings with concentric lamellae (**Figure 5(c)** and **Table 1**, **An. 10, 11**) remain well preserved.

Besides degrading bone botryoidal structures are also common of certains types of iron oxides, goethite for example frequently grows in lumpy-botryoidal forms. In this case, they form when crystals grow radially around nuclei of specks of sand or dust culminating as microscopic but up to megascopic half-spheres. Such structures are also pronounced features of carbonate flowstone. In the present case, we demonstrate their presence in Ossuary 6 but also as oxidized iron of Nails 1 and 2. The chemistry of the laminated Fe-hydroxide botryoids reveals somewhat low FeO contents but high concentrations of what may be organic carbon (**Table 1**, **An. 30 - 32**) thereby implying microbial activity (below).

Table 1. Chemical data for morphological structures in Cft Ossuaries and two Nails.

No.	Sample	Material-location	Element %							
	Ossuary 3		SiO_2	Al_2O_3	FeO	CaO	MgO	P_2O_5	F	CO_2
1	AS30b	ossuary wall (sediment. veneer)	3.76	0.38	nd	11.63	0.21	8.35	0.18	75.25
2	AS30b	ossuary wall crust	3.12	0.42	nd	27.25	0.25	19.95	0.38	48.28
3	AS30b	ossuary wall (grey-fibrous zone)	1.96	0.3	nd	23.11	0.33	16.69	0.18	57.04
4	AS30b	ossuary wall, sed. substratum-o	7.72	2.86	1.05	20.82	0.74	2.26	nd	63.61
5	AS30b	ossuary wall, sed. substratum-i	8.4	3.18	1.27	20.99	0.59	2.27	nd	20.99
6	AS30a	ossuary floor, red crust	3.85	1.19	nd	27.24	nd	21.19	nd	46.53
7	AS30a	ossuary floor, brown crust	6.16	2.58	1.74	49.68	0.4	24.76	nd	14.67
	Ossuary 6									
8	AS31a	ossuary wall, accretion rim	9.84	nd	nd	52.25	0.8	2.8	nd	34.31
9	AS31a	inner phosphatic zone (p)	6.55	nd	nd	42.92	nd	30.63	nd	nd
10	AS31a-1	outer quartzose lamella (q)	70.22	nd	nd	5.23	nd	nd	nd	24.55
11	AS31c	ossuary wall crust-osteon rim	10.07	0.11	nd	20.07	0.17	14.65	nd	54.63
12	AS31b	ossuary floor, Fe-rich fragment	3.61	nd	79.69	11.01	nd	5.7	nd	nd
13	AS31b	spore cluster in wood cell	nd	nd	nd	49.72	nd	30.74	nd	19.4
14	AS31b	wood cell wall	nd	nd	nd	44.58	nd	32,17	nd	22.73
15	AS31b	spheroid, germinated spore?	20.17	0.83	nd	36.1	nd	24.46	nd	18.44
16	AS31a	ossuary floor, Fe-rich fragment	1.37	nd	83.55	9.17	nd	5.91	nd	nd
17	AS31a	botryoid, outer lamellae (O)	2.97	nd	nd	29.42	nd	22.25	nd	45.36
18	AS31a	botryoid, fibers in core (i)	1.24	nd	nd	18.17	nd	13.67	nd	66.92
19	AS-X	Insect, interior skin fabric	0.34	1.4	nd	0.84	0.2	0.5	nd	96.72
	Ossuary 7									
20	AS47	hypha in biofilm	4.57	2.9	0.89	41.08	0.54	4.18	0.73	44.97
21	AS48	germinated spore in biofilm	1.89	2	0.93	41.48	nd	27.39	0.73	25.56
22	AS48	brown crust, spheroid in biofilm	3.46	2.65	1.07	39.48	nd	24.39	0.66	28.29
23	AS48	floor, brown crust, hypha tube	5.55	2.56	1.67	41.01	nd	16.34	0.68	32.2
	Ossuary 1									
24	AS40a	floor crust-germ. spore	27.15	0.81	1.07	30.5	0.31	16.5	nd	23.44
25	AS40e	floor crust	4.88	2.11	1.1	36.66	0.97	20.91	0.77	31.22
26	AS41a	Floor-carb. flowstone	2.39	1.28	1.28	54.99	0.38	0.8	nd	38.55
27	AS42a	ossuary wall-outer crust	1.72	1.16	0.91	45.28	nd	22.98	nd	27.96
	Nails									
28	Nail 1	Crystallites-magnetite	0.78	nd	35.8	nd	nd	nd	nd	63.48
29	"	crystallites, carb. substratum	0.37	nd	4.85	14.05	0.76	nd	nd	79.98
30	"	dark brown Fe-oxides	2.54	nd	23.57	0.51	0.36	nd	nd	73.01
31	"	red Fe-oxides	1.55	nd	27.1	0.36	0.28	nd	nd	70.7
32	"	FeO botryoid	1.36	nd	20.19	0.33	0.19	nd	nd	77.93
33	"	wood, cell wall	2.68	3.01	64.1	1.55	0.53	nd	nd	27.87
34	"	germinated spore in tracheid	4.98	0.8	57.6	2.23	0.47	nd	nd	33.92
35	"	micro-bone fragment	1.16	1.54	90.6	1.83	nd	nd	nd	4.87
36	Nail 2	fibrous crystalls cluster	1.17	0.57	7.99	14.9	0.37	0.57	nd	74.14
37	"	plumose crystalls cluster	0.04	0.62	20.75	12.14	0.3	0.23	nd	65.02

Continued

38	"	plumose crystalls cluster	0.95	nd	54.61	0.42	nd	nd	nd	44.02
39	"	micro-bone fragment	5.18	0.46	70.4	6.18	1.01	nd	nd	16.77
40	"	aerosol quartz grain	41.76	13.92	15.01	3.06	0.53	nd	nd	21.96
41	"	Talpiot Hill Rendzina soil	11.77	3.4	1.45	31.08	0.71	1.15	nd	nd

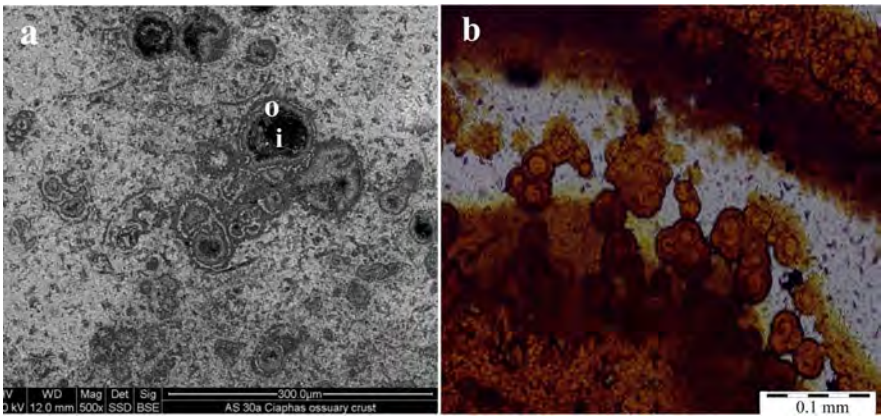

Figure 6. Botryoidal microstructures. (a) Clusters of spheroids resulting from microbial activity in bone debris. The spheroids are phosphatic botryoids, concentrically zoned with an opaque core rich in carbon (o - i, Table 1, **An. 17, 18**). (b) Laminated and botryoidal Fe-hydroxide in Nail 1 (Table 1, **An. 30 - 32**). Transmitted light optical microscope micrographs.

3.2. Carbonate Flowstone: Acccretion Fringes

Accretion fringes are minor but important microstructures in the ossuaries. They are seen as fine laminae mantling clasts of quartz and bone fragments in Ossuary 6 and also as carbonate mantles around fragments of laminated iron oxides of the nails. The microcrystalline fringes are ~0.05 to 0.1 mm (50 - 100 um) in diameter, in Ossuary 6 they consist of two discreet laminae (Figure 7(f)) both of calcite with up to 10% quartzose dust (Table 1, **An. 8 - 10**) and traces of clays (Al +/− Mg), Mg-salts and bone (P + Ca). The carbonate flowstone is clearly visible as the lumpy—outermost lamina (d) in Figure 2 and also as the white carbonate carapace covering segments of Nail 1 and Nail 2. The flowstone is important, besides providing us with important carbon-isotopic data, it seems to delineate an especially wet climatic period which affected the interior of all Caiaphas tomb ossuaries and the two unprovenanced nails at the same time. The carbonate fringes mantle quartz grains, bone fragments and other morphological elements in ossuaries and nails (Figure 7).

4. THE NAILS: Morphology and Mineralogy

We refer to the two nails studied as Nail 1 (white carbonate head) and Nail 2 (white carbonate lower body). The nails are 8 cm long with a slightly tapered end, they were purposely bent at an angle of 65˚—on Nail 1 and 75˚—on Nail 2 (Figure 8), a practice apparently linked to nails used in crucifixions. The white fragments attached to the Aba and Yehohanan nails (bottom right) are mostly

secondary phosphate minerals formed from the decay of bone phosphorus. The external crust of metallic iron of the nails is now entirely converted to micro-laminated orange to reddish-brown to almost black-colored iron hydroxides (**Figure 7(d)**). Some of the lamina are rich in concentrically zoned spheres (botryoids above) which, if organic in origin (**Table 1**, **An. 30 - 32**) may suggest that bacterial Fe (II) oxidation by (iron-eating) microorganisms (Casanova et al., 2010) may have played a role in the conversion of metallic iron to iron oxide. We emphasize that amongst the phosphatic floor debris of Ossuaries 6 and Ossuary 1 we found a number of fine chips of iron oxide with FeO concentrations reaching 83.5% (**Figure 3(b)** and **Table 1**, **An. 12, 16**).

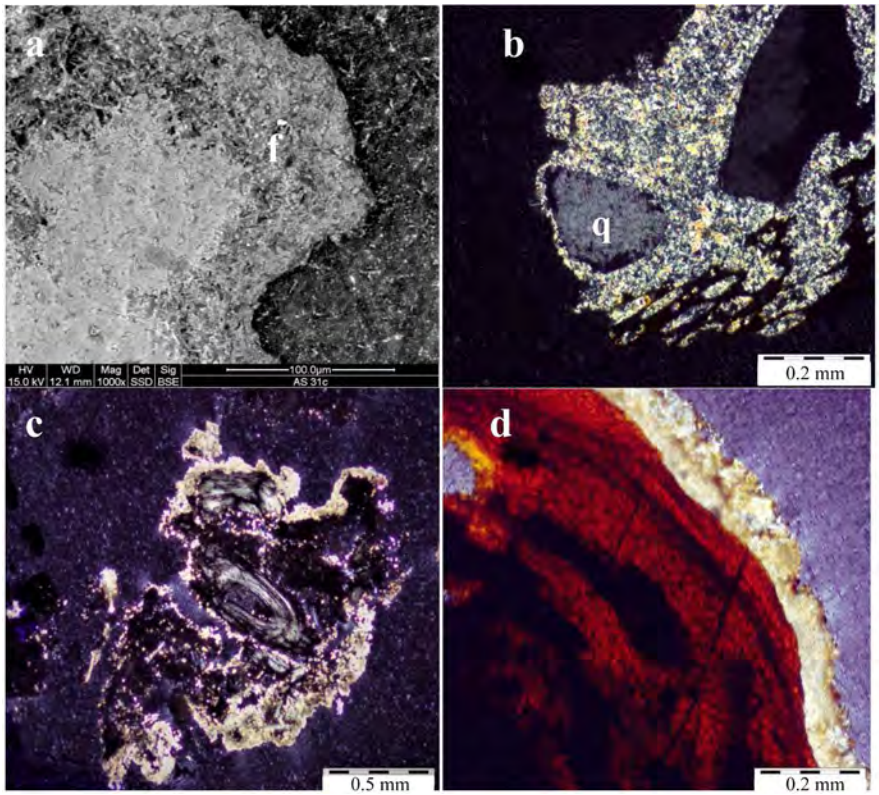

Figure 7. Accretion fringes of flowstone with quartzose aerosol. (a) Fringe (f) in Ossuary 6 wall crust and (b) mantling quartz grains (q) in floor rubble (one grain is black as it is in the extinction position), (c) fragment of bone osteon with concentric lamellae (**Figure 5(c)**) and (d) a fragment of microlaminated Fe-hydroxides from Nail 1. The color fringes are all carbonate flowstone ~80 - 250 μm thick, some (e. g. f) with a quartzose inner segment (a) SEM micrograph. (b - d) transmitted light optical microscope images.

Fine fragments of iron oxide and separately from flowstone carapace were scrapped off the nail surfaces and studied under the optical transmitted light microscope, SEM and by XRD. During oxidation of the nails, the metallic iron was converted to finely laminated brown to reddish colored iron hydroxides goethite (α goethite) and the uncommon lepidocrocite, a dimorphous form of goethite (γ goethite, **Figure 9**), both with the chemical composition FeO(OH). Although the amount of lepidocrocite is close to equal on the two nails the goe-

thite polymorph comprises ~44% on Nail 1 (white head) and ~67% on Nail 2. A small amount (~1.6%) of magnetite crystallites are present on Nail 1 but are not present on Nail 2 (Figure 10(a), Table 1 **An. 28, 29).** The magnetite is present in perfectly shaped rhombic dodecahedra and cubes ~4 μm in size; the crystallites define the final phase of iron oxide crystallization on the nails. In contrast to the hydroxides lepidocrocite and goethite the late-stage magnetite (Fe_3O_4) crystallized in what, at that time, was an anhydrous environment.

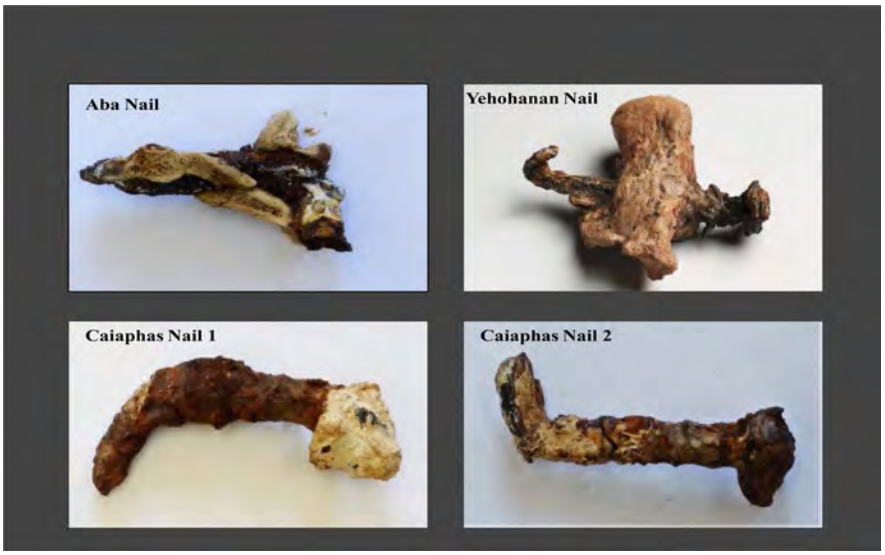

Figure 8. Nails used in crucifixions. Nail 1 is bent 65˚ and Nail 2 about 75˚ at the broken tapered end. Slivers of (light colored) bone are attached to the Aba nail and the Yehohanan Heel Bone nail. The white carapace on the Caiaphas nails is calcite ($CaCO_3$) flowstone. All the nails contain some adhered or perforated remains of bone tissue.

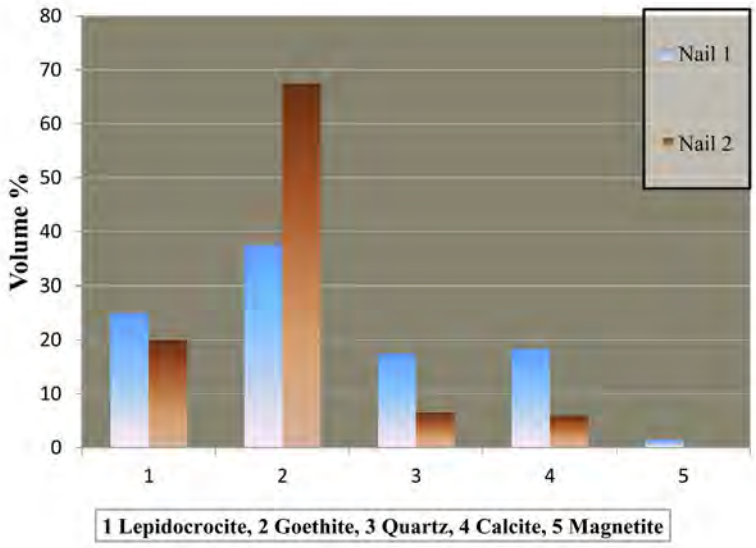

Figure 9. Column diagram for the main mineral constituents in the tomb Nails 1 and 2 (XRD determinations). Nail 1 was probably derived from Ossuary 1, Nail 2 from Ossuary 6.

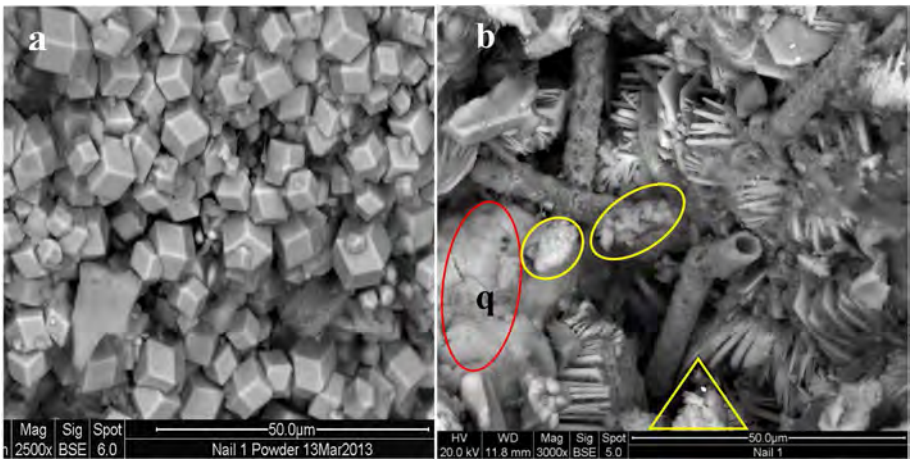

Figure 10. (a) Magnetite crystallites on Nail 1, the ~5 µm size idiomorphic cubes and dodecahedra represent the final stage of iron oxide crystallization on the nails. It postdates flowstone deposition. The formation of magnetite crystallites may possibly be linked to a type of microbial activity responsible for biofilms seen in 10(b). (b) Fungal filament tubes (hyphae) set in a mass of plumose lepidocrocite crystallites and aerosol quartz (q) in Nail 1. Three bundles (yellow marked) of small spores appear to be encapsulated in transparent (bacterial?) biofilms.

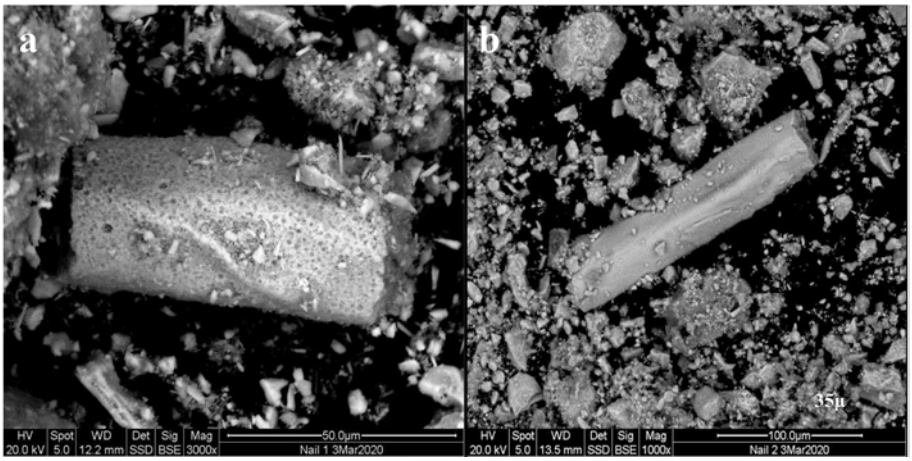

Figure 11. Micro-bone fragments in the rubble of Nail 1 (a) and Nail 2 (b). The bones are tiny and may be segments of what was spongy bone tissue in an osteon system (e.g. rod trabeculae, **Figure 5(a)**, **Figure 5(c)**). Both of what were phosphatic bone fragments are now entirely composed of Fe-hydroxides (**Table 1 An. 35, 39**).

5. The Wood: Micromorphologies and Determination of Wood Type

We were amazed to discover, even under low power SEM magnification, ~2 cm long fine slivers of wood accreted to both nails buried within quartzose sedimentary debris. Many of the wood cells are entirely filled with radiating fibers and blades of crystalline iron hydroxides (**Figure 13(a)**). In addition, we also found in the ferruginous debris and within the wood tracheids (cells), small—yet very pronounced amounts of organic materials *all of which we have also identi-*

fied in the tomb ossuaries. They include chips of micro-bone, fungal sporangia, at least two dominant forms of spores and related filament tubes such as sporangiophores and hyphae (**Figures 12-16**). Near concentrations of organic debris we have noted (SEM-EDX) an occasional pronounced increase (0.2% - 0.57%) in phosphorus concentration (e.g. **Table 1**, **An. 36, 37**), a feature especially noted on Nail 2. We attribute such anomalous phosphorus concentrations to the presence of bone tissue now, as shown above, in major part decayed or replaced by iron oxides (**Figure 11**, **Table 1** **An. 35, 39**). It is amazing how the organic components of the wood, including all the invasive and/or accreted biological species have, as the wood, been entirely converted to iron hydroxides. A similar phenomenon, a "pseudomorphous" replacement of coffin wood cells by iron corrosion products adjacent to iron bars inside an 8th century BC tomb at Gordion, Turkey, was observed by Blanchette and Simpson (1992). We consider such complete replacement of the wood organic components by iron hydroxides as a petrification process, in the sense that the mobile iron replacing the organic compounds was controlled by the wood and fungal microarchitecture on an atom by atom basis.

One of us (WHS) identified the wood to be that of a mature *Cedrus* (*Cedar*)—a genus of coniferous trees in the plant family Pinaceae. In the Mediterranean region Cedar occurs at altitudes of 1000 - 2200 m and although an important tree in the mountains of Lebanon (Cedrus Libani), Syria and Turkey it was a special and costly, perhaps even extraordinary, import into Roman period Palestine. The present identification is based on detailed SEM study of some well preserved morphological features which characterize Cedar wood. They include the width of latewood zones, decorated tori, rays of parenchyma cells with taxodioid pits, heterocellular rays and resin canals, features we show below (**Figure 13**, **Figure 14**, **Figure 16(a)**).

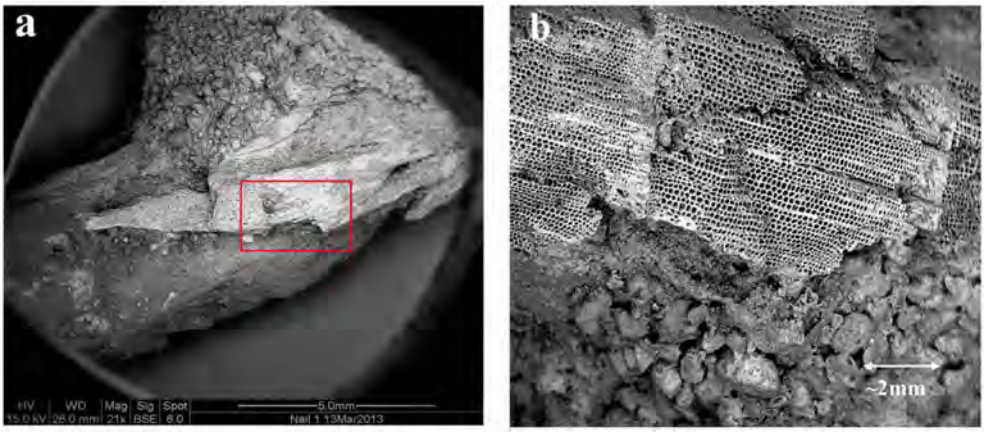

Figure 12. (a). Slivers of wood accreted to Nail 1 by Fe-hydroxides. Aerosol quartz (fine grains 150 - 300 μm in size) with a clayey dust veneer is filling gaps between wood and nail Fe-hydroxides. (b) Detail on wood, the fine black dots are a transversal view of tracheids—the cellular microstructure of wood. The entire wood sliver (left photo) is about 2 cm long.

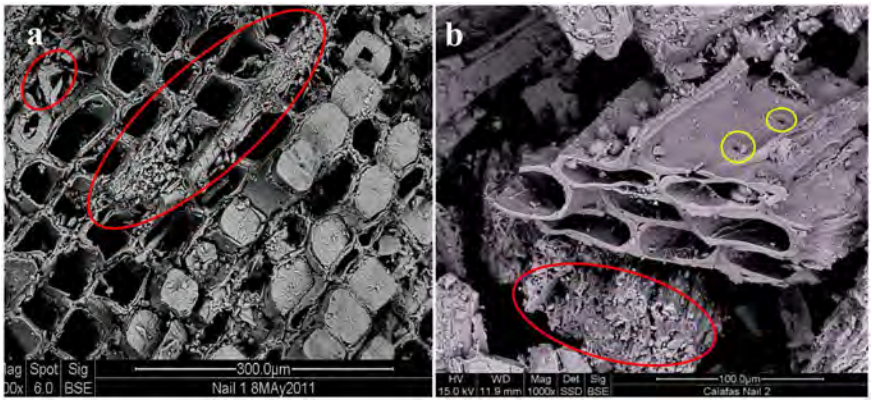

Figure 13. (a) Wood microfabric. Transverse view of wood sliver from Nail 1 reveals detail of tracheid cells many of which are entirely filled with radiating fibers of goethite (white). (b) Both transverse and tangential sections of tracheids. Large Sg spores inhabit a few cells some of which exhibit bordered pits (yellow markers). Many tracheids have suffered decay and total collapse (red markers) as a result of fungal attack and degradation processes. Fungal activity was either coeval with or postdates Fe-hydroxide crystallization inside the tracheids as some cells filled with crystallites are deformed.

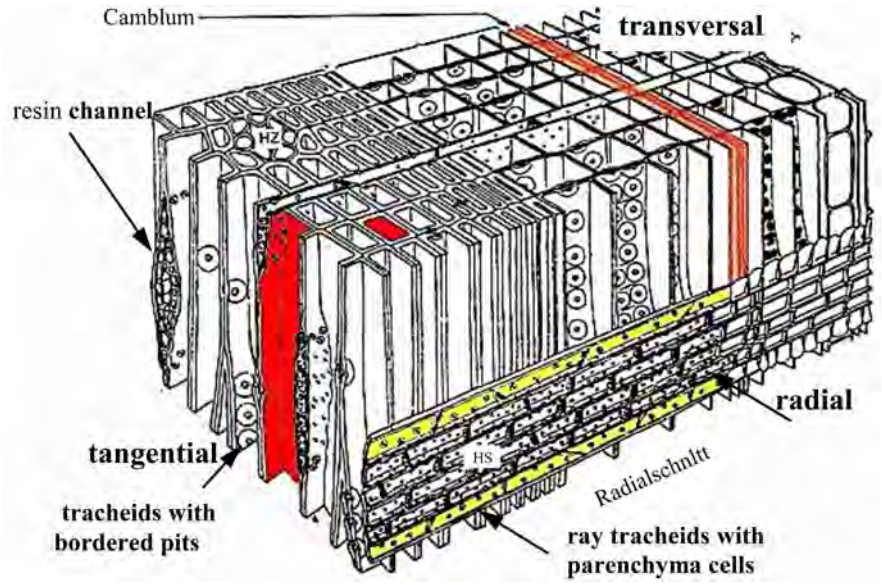

Figure 14. Model of wood cells with different perspectives of the main microstructural elements. Source: Timber Construction Material p. 31 after: "Magdefrau 1951".

6. Bioinfestation: Microfauna and Microflora

During our study of the Caiaphas tomb ossuaries and the two unprovenanced nails we discovered evidence of widespread microbial infestation accompanied by partial biodeterioration of organic components in both the ossuaries (bones) and also of the wood accreted to the nails (above). Bone and wood provided a choice habitat for microbial attack and both were colonized by what appears to be a single species but it is feasible that in view of the ~1900 year time span, more than a single generation and species of fungi is manifested. The fungal morphologies include (Figures 15-17) round to occasionally oval microstruc-

tures most of which constitute fungal sporangia. The sporangia are enclosures in which spores—the fungal reproductive cells—are formed and from which they eventually are forcefully expelled before proceeding to the next evolutionary step of germination. The sporangia and germinating spores often exhibit protrusions of filamentous tubes (sporangiophores or hyphae)—the main mode of vegetative growth of fungi which function as conductors transporting water and other nourishment from roots to leafs of growing plants. The spores when released from their housing into the air are dispersed by wind and water and can travel great distances from their source.

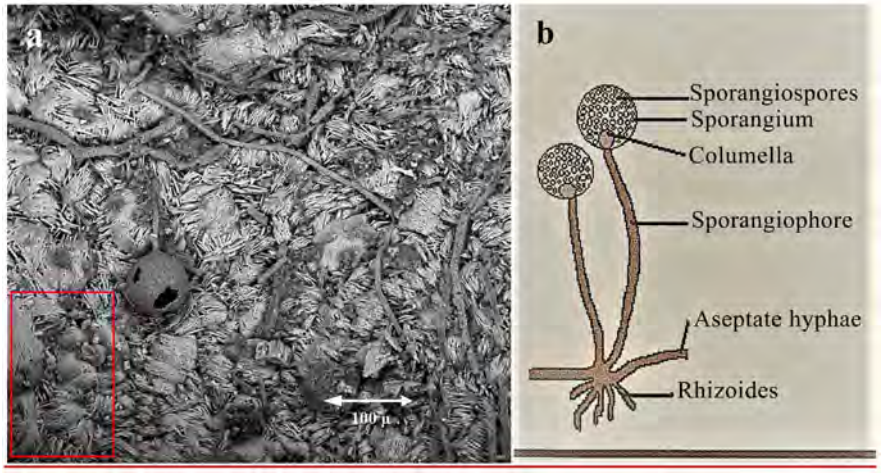

Figure 15. (a) Fungal sporangium with a protruding filament tube (sporangiophore). The surrounding crystalline matrix consists of bladed lepidocrocite +/− goethite and broken fungal hyphae. With the exception of a few fine grains of quartz (lower left) the whole mass is chemicaly iron hydroxide. (b) A model of the most basic of fungal morphologies. Source: http://www.fungionline.org.uk/.

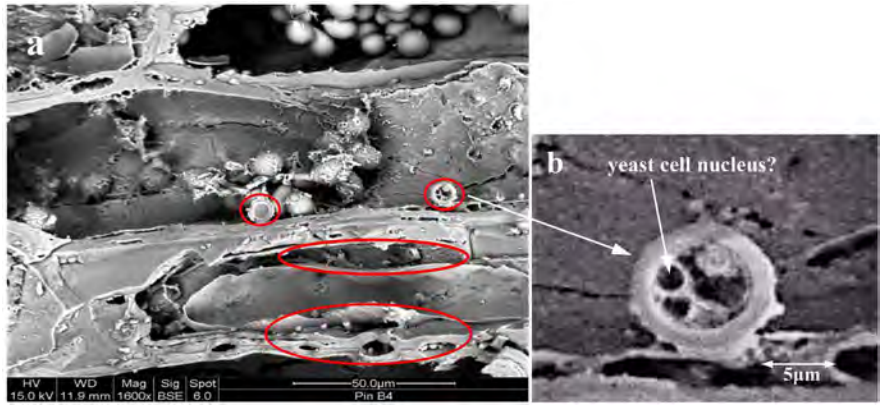

Figure 16. (a) Wood microfabric and microbial activity in Nail 2 wood tracheids (tangential section), note bordered resin pits some carrying discreet Ss spores and broken hyphae. Slightly conical Sg sphores (~8 - 10 µm diameter) some with protruding hyphae are clustered in what we interpret as resin channels (**Figure 14**) that carried plasma in the form of sugar or starches. Some spores (marked) have concentric laminae, perhaps as layers of wall material added during germination. Others (b) exhibit an internal microstructure markedly similar to yeast cells.

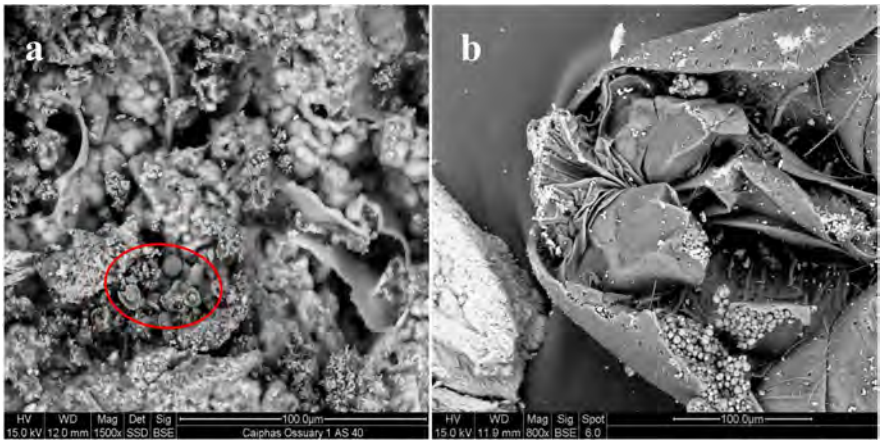

Figure 17. (a) Ossuary 1, degraded bone microfabric, the voids are filled with globular Ss spores. Enclosed spherical structures are foraminifera, one spheroid is an Sg spore or diatom (Table 1 **An. 24**). The bone microfabric may be trabecular spongiosa, a mixture of bone mineral and marrow. (b) Head (underside view) of an insect, possibly a Tube-Tailed Thrips. Although Thrips feed on fungal spores in the present case it seems that the spores had the advantage and colonized the insect's body. The insect is a late visitor as the body has retained all its carbon (Table 1, **An. 19**).

Fungal activity inside ossuaries will result in partial to complete degradation, or chemical breakdown, of bone microstructures and, if present, the wood cell network. In the latter case, decay attacks the primary cell wall components—the carbohydrates, lignin and cellulose, a process accompanied by the release of CO_2 (Figure 13, Figure 19 and Table 1, **An. 33**). We have observed two (but not only) principal varieties of spores in our materials (1) a group of small spores ~3 to ~4 μm (0.003 to 0.004 mm) in size and (2) a second group ~8 to ~10 μm in size, with some marked exceptions (e.g. Figure 19(b), Figure 20(a)) noted. We will herewith refer to the former as Ss (small) spores and the later as Sg (germinated) spores, the former (Ss spores) resemble a tightly clustered mass of globules or clusters of grapes, the latter (Sg spores) occur as individuals or small bunches of ~5 - 10, frequently pear-shaped bodies. The Ss spores are very much dominant inside the ossuaries where they have colonized the microstructures of bones but also other organic (e.g. insects, Figure 17(b)) morphologies. The Sg spores, although also present inside degraded bone microstructures, are ubiquitous inside the wood tracheids, which was clearly their much preferred habitat. Because of the close spacial relationship and presence of what appear to be transitional stages between the two spore groups (e.g. Figure 19 and Figure 20(a)) we reason that rather than what at first glance appear to be different fungal species they are one species in different stages of development leading to germination. We emphasize that some of the spore-like structures reveal an internal microfabric resembling yeast cells (Figure 16(b)). Spores are unicellular, but under favourable conditions, which involves an exogeneous supply of moisture, water and nutrients will germinate, a process that entails spore swelling and change in shape and finally extrusion of one or more germ-tubes (Figure 18(a),

Figure 19(a)). Microbial degradation is affected by amount of light, water and oxygen availabilty, it will take place as the hyphae spread through food and release enzymes that break food down into substances that the fungi can easily absorb. In Figures 15-20, we have tried to elucidate some of these processes and the range of fungal micromorphologies that we have encountered in the ossuaries and nails (Full explanations in: http://www.fungionline.org.uk/).

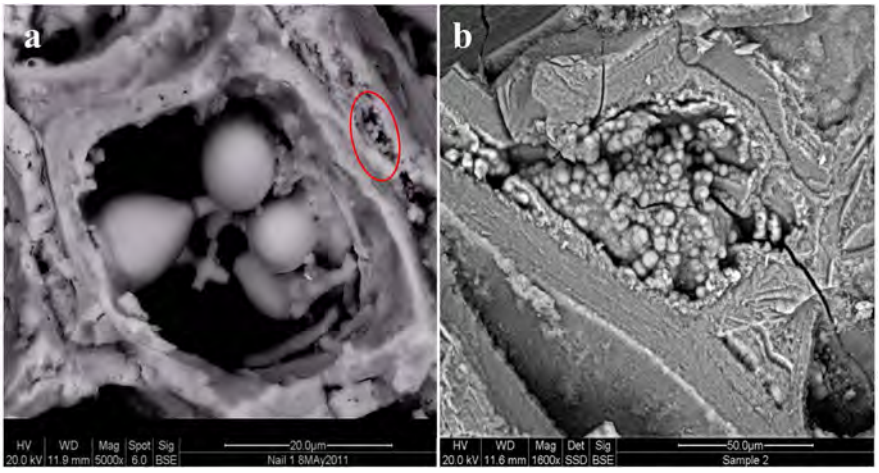

Figure 18. (a) Wood tracheids transversal sections in Nail 1 and (b) in a wood fragment in Ossuary 6. In (a) the cell is occupied by germinated-conical Sg spores, germ tubes protrude and bifurcate, they are attached to the cell walls from which nourishment is drawn. Small globular Ss spores in (b) have not germinated. The Sg spores in (a) and tracheid are compositionally Fe-hydroxide, in (b) spores and wood cell are bone apatite rich in P and Ca (Table 1, **An. 13, 14, 33, 34**).

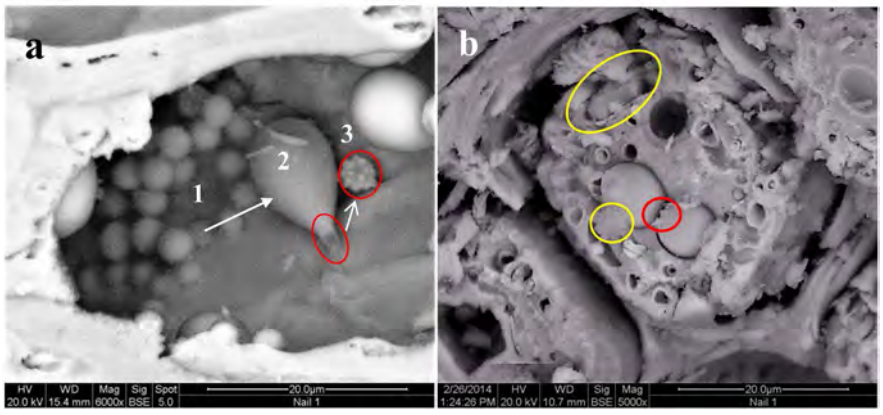

Figure 19. (a) The figure illustrates the link between the three principal morphological forms of what we view as evolving spores: (1) a cluster of small (Ss) spores, (2) a germinated Sg spore, it has swollen and is much larger than its predecessors, it is now cone-shaped with an emergent germ tube, (3) a small apical vesicular complex of fine cells (AVC) has broken off from the tube terminus. In (b) the full array of spore sizes is seen within a single tracheid, the spores range from ~2 μm to ~10 μm, they seem to be embedded in what was a soft tracheid resin. One large Sg spore shows an opening on the upper left surface (red marking). In yellow enclosures are spore clusters enveloped in biofilms (discussed below).

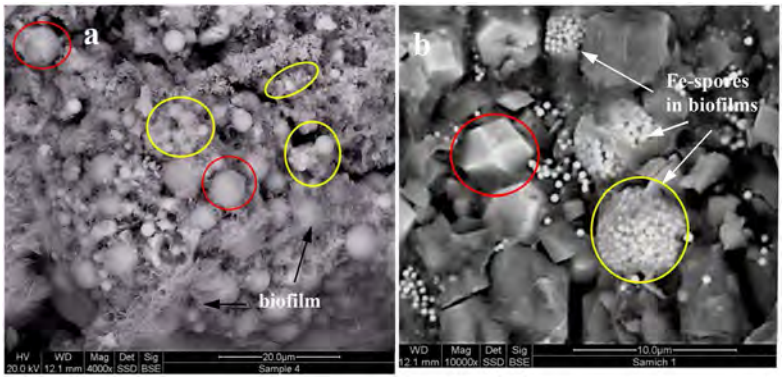

Figure 20. (a) Fungal chaos or fungal—bacterial coexistence in Ossuary 7. As in **Figure 19** (in wood) the full range of Ss, Sg (and bacterial?) spores (sizes < 1 μ to ~8 μ) is exhibited. Some spore bundles, and the bottom right area, are enclosed by a veil-like biofilm, perhaps due to late bacterial attack—or possibly in a symbiotic relationship with the fungus. (b) Bacterial biofilms inside the surface patina of a construction stone, shown for comparison. Some Fe-spheres (white, ~1 μm in diameter) are scattered but also coalesced inside biofilms. The process culminated in crystallization of idiomorphic pyrite dodecahedra (FeS_2 marked) and cubes. We point out that the latter are not unlike the magnetite crystallites in Nail 1 (**Figure 14(b)**). (**Figure 20(b)** from Shimron, A. E. 2012, unpublished report).

7. $\delta^{18}O$ and $\delta^{13}C$ Isotopes of Ossuary 6 and Nail 1 Speleothems

Surface rain waters percolate downward through soil and by reacting with CO_2 supplied by biological activity form carbonic acid (H_2CO_3). The acid reacts with the host rock and the water becomes saturated with respect to calcite forming $Ca(HCO_3)_2$ in solution. Should the water reach the open space of caves (or tombs) under certain conditions CO_2 degassing will take place and carbonate minerals will be deposited as speleothems or flowstone (stalactites, stalagmites). Chemically what takes place is the compound $Ca(HCO_3)_2$ breaks up to $CaCO_3$ (flowstone) + CO_2 + H_2O. In their study of some Israeli caves Bar-Matthews & Ayalon (2001, 2004) amongst others, have shown that the oxygen isotopic composition ($\delta^{18}O$) of speleothems reflects the temperature at the time of their deposition and also the $\delta^{18}O$ values of the water from which they were deposited. In another study, performed to evaluate the rain shadow effect on the amount of rainfall and speleothem growth, Vaks (et al., 2003) found that variations in the carbon isotopic composition ($\delta^{13}C$) of speleothems results from differences in the type of vegetation in the vicinity of the cave. In such a case, enrichment in the $\delta^{13}C$ (seen in lower negative values) of calcite speleothems usually reflects an increase in the contribution of C4-type plants (crop plants, saltbush, corn, annual summer plants) to the soil CO_2. We know that the sudden passage from the western to the eastern (rain-shadow) side of the Jerusalem mountain ridge is highlighted by an increase in temperature and evaporation rates, in addition to being accompanied by a sharp drop in rainfall from ~500 to 250 mm (Vaks et al., **Figure 1**). Notably, these features are also manifested by an increase in $\delta^{18}O$ and $\delta^{13}C$ (lower negative) vaues. On the basis of these data, it has been concluded

that the $\delta^{18}O$ and $\delta^{13}C$ isotopic composition of speleothems is dependent on environmental conditions.

The Ma'ale Efrayim Cave is located in the rain shadow on the eastern side of the central mountain ridge on which Jerusalem is located. The Soreq Cave is located in the rainier western side of the mountain ridge whereas the Jerusalem West Cave (Frumkin et al., 1999) lies close to the central part of the ridge, near the heart of the city. The Caiaphas family tomb lies about 7 km directly south of the Jerusalem West cave about halfway between central Jerusalem and Bethlehem. It is located on the east-facing slope of the Jerusalem mountain ridge, just within the western edge of the "rain shadow" desert region (ref. above). We show and compare our $\delta^{18}O$ and $\delta^{13}C$ values with data from flowstone collected from the caves above (**Table 2**, **Figure 21**). We note that the $\delta^{18}O$ and $\delta^{13}C$ values we obtained for Ossuary 6 and Nail 1 are (1) very similar and (2) considerably closer in magnitude than values obtained from the same speleothem for different periods in time in the caves above. The Nail 1 value is close to Jerusalem West cave present values. Isotopic $\delta^{18}O$ and $\delta^{13}C$ values oscillate frequently with time and up to 2.15‰ variation within a single annual growth band has been measured, consequently, the small difference in the isotopic values of Nail 1 and Ossuary 6 is insignificant and can be attributed to a slight difference in time of speleothem deposition. We conclude that our $\delta^{18}O$ and $\delta^{13}C$ values are 1) higher than almost all values for the last ~5000 years obtained for flowstone from Jerusalem area caves and 2) it appears that waters from an area rich in C4-type plants made a higher contribution to the Caiaphas tomb and Nail 1 isotopic values than those from other caves sampled. Such data make the Ossuary 6 and Nail 1 values unique.

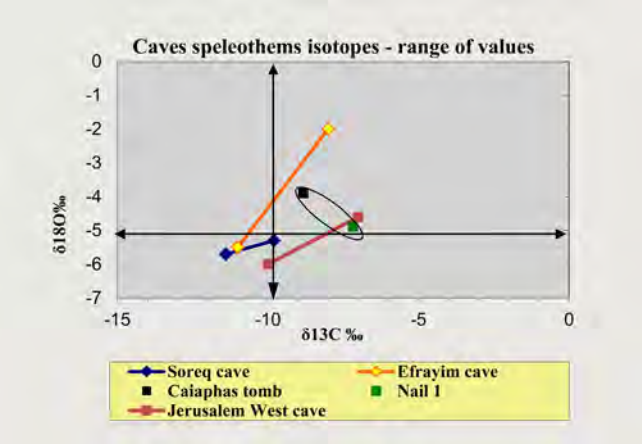

Figure 21. $\delta^{18}O$ and $\delta^{13}C$ isotope values for Ossuary 6 and Nail 1 with isotope values for speleothems from some Jerusalem area caves added for comparison. Jerusalem West data from Frumkin et al. (1999), Soreq and Efrayim caves data from Vaks (et al., 2003) and data for the Soreq cave from Bar-Matthews and Ayalon (2004). With the exception of one value for the Jerusalem West cave and one for the Efrayim cave the isotope values for Ossuary 6 and Nail 1 stand out as (1) being very similar and (2) higher (lower negative) from most other cave values in the Jerusalem area. With this in mind, the Ossuary 6 $\delta^{18}O$ is slightly heavier than is usual for Jerusalem (although within normal flluctuations) whereas the $\delta^{13}C$ is a common Holocene value for this area.

Table 2. $\delta^{18}O$ and $\delta^{13}C$ isotope values for flowstone from the Caiaphas tomb, Nail 1 and for the Soreq, Efrayim and Jerusalem West caves.

Isotopes	Soreq Cave	Efrayim Cave	Jerusalem West Cave	Caiaphas Tomb	Nail 1
	West Judea hills	Jordan Rift valley	West Jerusalem	East Jerusalem	Caiaphas tomb (?)
$d^{18}O$ ($\delta^{18}O$)	−5.7 to −5.3‰	−5.5 to −2.0‰	−6.0 to −4.6‰	−3.9‰	−4.89‰
$\delta^{13}C$ (range)	−11.4 to −9.8‰	−11.0 to −8.0‰	−10 to −7‰	−8.82‰	−7.17‰
Period/time represented	Last ~5000 years	67,000 to 24,000 yr B.P.	Last ~3000 years	1st century CE to present	1st century CE to present

8. Discussion

The Ossuaries: The IAA has not reported two nails found or missing from any excavation other than those from the Caiaphas tomb. Nonetheless, we have examined the possibility that the unprovenanced nails were derived from another tomb where bioactivity by species identical or similar to those in the Caiaphas tomb had taken place. For this and other objectives, we have sampled and studied the petrography and petrochemistry of materials from interiors of about 40 ossuaries collected from some 25 tombs in the Jerusalem area (Shimron et al., 2020, **Figure 1**). We can now conclude that we have not found any fungal or bacterial species or biodegradation of the type we observed in the Cft and on the two nails**,** in ossuaries from any other tomb. In addition, neither have we found evidence or any record of such profuse and continuous flooding of ossuaries from any of the other tombs that we have examined. We reason that a continuous abundance of water and colonization of the tomb by a unique fungal species makes the Cft and materials found therein so profoundly unique. Besides winter rains the amount of moisture in the Cft was influenced by periodic water overflow from the neighboring Hellenistic period aqueduct. Wall-parallel laminae of sediment and bone rubble with various degrees of bone degradation and decay are testimony that geological and biochemical processes were periodically active in the ossuaries. The stone boxes with bones, two with oxidizing iron nails with attached wood in standing pools of water must have been magnets for robust fungal activity. Bone degradation, wood decay and the character of the nails' Fe-oxidation products testify on the dependence of their immediate environment on the amount and pH of standing water. We have shown that changes in bone micro-architecture seen in fragments of phosphatic crusts attached to the walls and floors of the ossuaries exhibit various stages of degradation, decay and recrystallization to fluorapatite [$Ca_5(PO_4)_3F$] and hydroxyapatite [$Ca_5(PO_4)_3OH$]—the expected and thermodynamically stable phosphate minerals that form under ordinary cave conditions (Trueman et al., 2004 and **Table 1**).

Although Ossuary 6 was found in situ, its cover was removed by Byzantine-period tomb robbers only to be replaced shortly thereafter perhaps out of respect for the recognizable inscribed Caiaphas family name. The ossuary was not moved by robbers from its original site for the same reason and the only disturbance it may have suffered is the removal and immediate disposal of a nail

(Nail 2) found by excavators on the kokh floor near the ossuary. In the first excavation report the head excavator (Greenhut, 1992) notes that "one nail was found inside one of the ossuaries" while the other on the floor of Kokh IV (that is near Ossuary 6). In a subsequent report Greenhut (2004) however notes that one nail (Nail 1) was found in Ossuary 1. In the present work, we have assumed that the latter report is accurate and that indeed one of the two nails (Nail 2) was removed from Ossuary 6 during the robbers' incursion into the tomb whereas the second nail (Nail 1) spent its entire ~1900 year long history undisturbed inside Ossuary 1. We have summarized our main observations and elucidate the main links between the Cft ossuaries and the two nails in Table 3 below.

Table 3. Summary of the main events affecting Ossuaries 1, 6 and two unprovenanced nails.

Time-Period	Ossuary 6 (decorated)	Ossuary 1	Nail 2 (white cap) In Ossuary 6	Nail 1 (white body) In Ossuary 1
1st century CE	Bones placed in ossuary	Bones placed in ossuary	Nail 2 placed in Ossuary 6	Nail 1 placed in Ossuary 1
	Intrusion of moisture. Bone degradation	Intrusion of moisture. Bone degradation	Nail metallic iron oxidation	Nail metallic iron oxidation
	Incursion of water with aerosol and flooding of ossuaries. Brown base laminae deposited	Incursion of water with aerosol and flooding of ossuaries. Brown base laminae deposited	Fe-oxidation and crystallization of lepidocrocite. Fibrous goethite forms in wood cells.	Fe-oxidation and crystallization of lepidocrocite. Fibrous goethite forms in wood cells
1st century CE Start of fungal infestation?	Microbial (fungal) activity, formation of phosphatic crusts on floor and walls of ossuary. Phosphatic botryoids	Microbial (fungal) activity, formation of phosphatic crusts on floor and walls of ossuary. Phosphatic botryoids	Microbial activity in wood cells, germ. of Sg spores, cell decay. Lepidocrocite and goethite. Bacterial activity, Fe-botryoids	Microbial activity in wood cells, germ. of Sg spores, cell decay. Lepidocrocite and goethite. Bacterial activity, Fe-botryoids
4-5th century CE Byzantine incursion by tomb robbers	Ossuary uncovered, Nail 2 is removed from ossuary by tomb robbers and dumped on tomb floor. Ossuary lid is replaced	Ossuary moved from its kokh, lid is removed, ransacked by tomb robbers	Nail 2 is dumped on tomb floor. Fe-petrification of wood and fungi. Mostly *goethite* crystallizing on moist tomb floor at pH 7 or greater.	Fe-petrification of wood and fungi. *Lepidocrocite* is now the main Fe crystallizing (at pH 5 - 6.3) on ossuary floor.
The "Wet Event" inside the Cft	Deposition of flowstone crusts. $CaCO_3$ accretion rims	Deposition of flowstone crusts. $CaCO_3$ accretion rims	Deposition of flowstone crusts, $CaCO_3$ accretion rims	Deposition of flowstone crusts, $CaCO_3$ accretion rims
19th-20th century (bacterial activity?)	Bone degradation	Bacterial attack on Ossuary 7 fungal colony. Formation of biofilms in Ossuary 7 and Nail 1.	Bone degradation	Bacterial attack on Nail 1 fungal colony. Formation of biofilms and biocrystallation of magnetite above flowstone laminae

The Nails: The two iron oxydation products we have identified are goethite [α-FeO(OH)] and lepidocrocite [γ-FeO(OH)]—the less stable and infrequently encountered polymorph of goethite. The reddish brown lepidocrocite (e.g. **Figure 6(d)**) crystallizes preferably when iron oxidizes in water under hydromorphic conditions in an anaerobic environment (Ross & Wang, 1982; Schwertmann & Taylor, 1972), but it has also been identified in association with biotic reactions that form iron-oxides (Schieber & Glamoclijia, 2007). Its growth is in-

fluenced by a number of factors amongst which are a preferred pH between 5 and 7 and the presence of elements like phosphorus (Cumplido et al., 2000). Hydromorphic soils have a notably low pH of ~4.5 - 5, they are typical of marshes and bogs, a situation not unlike that prevailing in standing pools of water inside a tomb, or an ossuary with degrading and decaying bones infested by a fungal colony. The rubble in Ossuary 6 contains 0.8% and in Ossuary 1 and Ossuary 7 0.2% sulphur with locally up to 3% present. Such acidifying material lowers the pH of the waters which must already have been de-oxygenated by microorganisms feeding on organic material. In this manner, conditions were generated, in the tomb and ossuaries in which iron-oxidizing organism (which prefer to colonize in the transition zone between the anaerobic and aerobic environments) thrive.

Although the two nails contain close to the same amount of lepidocrocite (~20% and 24%, **Figure 9**) the amount of goethite in Nail 2 is close to double that in Nail 1. This fact indicates that at some point in their history the geochemical setting of the nails must have changed in a manner that promoted the crystallization of goethite rather then lepidocrocite on Nail 2. Such a change in the geochemical mileu would have taken place when Nail 2 was removed from its Ossuary 6 habitat and dumped on the tomb floor by robbers during the Byzantine (4^{th}-6^{th} century CE) period. Conditions of light, temperature, pH and amount of water must all have changed for Nail 2 at this time. Any major influx of fresh water into the tomb would have resulted in improved oxygenation and a rise in the pH of tomb moisture. It is precisely this kind of change that is now manifested by the considerable dominance of goethite over lepidocrocite on Nail 2, an indication that their evolutionary paths must have diverged at about this time. Casanova (et al., 2010) showed that at pH 7 both lepidocrocite and goethite may form by Fe (II)-oxidizing bacteria whereas at pH lower than 6 lepidocrocite will be the favored iron oxide (a chemical condition also favouring yeast fungi). In such a case goethite, which is more abundant on Nail 2, crystallized in moisture with a pH near neutral or alkaline (pH 7 or higher). Such a change would have taken place had Nail 2 been removed from what must have been its initial hydromorphic-hypoxic environment (e.g. Schwertmann & Taylor, 1972) inside Ossuary 6 and transferred to a better oxygenated chemical environment on the tomb floor. Such an explanation is consistent with the archaeological findings and mineralogy of the nails. Evidence of a late change in the microbial setting of the nails is indicated by the presence of a small amount of the anhydrous iron oxide magnetite (Fe_3O_4, **Figure 10(b)**). Identified by SEM and XRD on Nail 1 these amazing ~5 μm size idiomorphic crystallites occur in clusters covering what is late-crystallized flowstone carbonate (e.g. **Figure 6**, **Figure 10(b)**, **Figure 20(b)**). The presence of such magnetite implies crystallization under hypoxic or anaerobic conditions during which the Fe-hydroxides can be further oxidized by organisms to form crystalline magnetite (Kirschvink et al., 1992; Lowenstam, 1981) which, it appears, became the thermodynamically more stable phase. The

magnetite clearly designates the final phase of iron oxide crystallization under what must have been anhydrous, possibly toxic, conditions.

Bioinfestation: The fungal spores must have arrived in the Caiaphas tomb mixed with atmospheric (aerosol) dust with quartz and clayey soil particles ubiquitous inside the ossuaries and also on the nails. The infiltration into the ossuaries of fine sediment carrying spores most likely took place during the intrusion of large amounts of water which periodically flooded the tomb. Fungi are heterotropic organisms which cannot produce their own food instead they take nutrition from other organic sources such as bone or wood. Living bone consists of three major components, organic matter (mainly protein), mineral in the form of calcium phosphate (apatite), and water. Wood on the other hand consists primarily of cellulose—a form of carbohydrates, the primary target of fungi which metabolize the wood, resulting in carbon dioxide being released back into the atmosphere.

Some spore-forming bacteria can form highly organized multicellular communities referred to as biofilms (also called slime). Biofilms are one of the more extraordinary morphologies we discovered in the rubble of Ossuary 7 and also Nail 1. They are an important form of microbial growth occurring as complex cell populations primarily constructed of yeast-form and hyphal cells (e.g. **Figure 16(b)**). Their formation is a sequential process which involves attachment to a subsurface, proliferation of the yeast cells over the surface and finally extrusion of hyphae (Fanning & Mitchell, 2012). We reason that the biofilms that invaded Ossuary 7 (the broken and repaired ossuary) and Nail 1 (**Figure 10**, **Figure 11**, **Figure 20**) may have been in an amiable, perhaps symbiotic relationship with the neighbouring fungi, if so presenting us with an amazing example of a bacterial-fungal interaction (BFI). Bastias (et al., 2019) for example, have shown that many bacteria generate such a symbiotic relationship with plant-eating fungi. In this respect, we question the possibility that the biofilms acted as a kind of *umbilical cord* between the Ss and Sg groups of spores (see encircled in **Figure 20(a)**, right of center).

Based on our collective data above involving the full range of fungal infestation phenomena we reason that the fungal species that colonized the Cft are of the Yeast Kingdom of which at least 1500 species have been recognized. Similar to our unusual range of spore sizes and unlike in most fungal species, yeast spore sizes are known to vary greatly even within a single species, with the 3 - 4 μm diameter (our Ss spores?) most common (e.g. Lema et al., 2012). Many yeast species (e.g. Saccharomyces cerevisiae) convert carbohydrates to carbon dioxide and alcohol during the fermentation process and the products of this process have been used in baking and production of alcohol for thousands of years, the fungi in the Caiaphas tomb may be testimony to just that. Although our fungi lack the "budding" morphology of Saccharomyces, we reason they may be a close variant of this species. A potential source of yeast fungi in the Caiaphas tomb could have been the family of the high priest Caiaphas (1st century CE)

whose home with its kitchens and wine cellar must have been near the family tomb. A possible alternative, or additional source of the yeast fungus could have been, some 1900 years later, the British headquarters during the Mandate period in early 20th century Palestine. This imposing and still existing structure on the Hill of Evil Council was constructed next to the ancient aqueduct (**Figure 1**), almost certainly an important source of water to Government House. We suggest that the yeast fungus may have been widely used not only in the Caiaphas family household but also ~1900 years later in the British Government House kitchens for the production of baked goods and alcohol. If so, the aqueduct whose ~60 km route from near Bethlehem to Jerusalem's Temple Mount may have been an important source of not only water for the Temple but also the carrier of what appears to be a very special fungal species into the tomb of the Caiaphas family. We had communicated with a number of scientists in the field of fungal biology regarding the complex fungal species here discussed and would like to quote from a recent mail exchange with R. Blanchette, Professor of Plant Pathology at the University of Minnesota. We quote "*You have put together some very interesting information. These observations are very different from the type of decay and fungi that we have found in various tombs and dry environments. It is amazing you are able to get this information from just a few minute segments of wood and bone adhering to the nails*".

9. Conclusion

In spite of the little material available to us for study, we have been able to determine that the long chain of sedimentary, geochemical and microbial events which affected the interior of the Caiaphas tomb ossuaries and the two nails were identical through a major part of their ~1900 year history (**Table 3**). The various components of fungi although much phosphatized, or petrified by iron oxides, have retained their original morphologies and are thus recognizable amongst the degraded bone debris but also on the wood fragments accreted to the nails. We cannot comment on the possible significance, if any, of the wood accreted on the nails being cedar (Cedrus Libani). Cedar did not grow in Early Iron age Palestine where it was a rare and expensive import which, according to the Old Testament, was used in contruction of the Temple in Jerusalem (circa 970 to 931 BCE). Since cedar rejects wood rot some of its timber was also used in the construction of what is referred to as the "Jesus Boat". Although this, now excavated, small fishing vessel sank in the Sea of Galilee in the 1st century CE no implications have been made that it had any historical connection with Jesus of Nazareth. Reuven (2013) attempted to show that some wooden beams of cedar may have been used in construction on the Herodian period (1st century CE) Temple Mount in Jerusalem—the period of Caiaphas' rule.

Due to the lack of any evidence to support the hypothesis, we contest the proposal that the nails found in the Caiaphas tomb (Greenhut, 2004; Rahmani, 1961) were used for carving the decorative motives or were used for inscribing

the names on the ossuaries. Besides the problematic morphology of the nails we also take into consideration that inside one of the skulls in the tomb a coin was found, this may perhaps be attributed to a known pagan practice whereby the coin was meant as a payment to Charon—the ferryman of the Underworld. Thus far only one other nail has ever been found inside an ossuary (the Yehohanan Heel Bone nail, **Figure 8** above, Tsaferis, 1985) and that nail has been the only recorded archaeological artifact specifically identified with crucifixion. The presence in a burial context of what appear to be two crucifixion nails in the tomb of Caiaphas may, as the coin above, be more than a simple curiosity, rather they may be related to the fact that both Jewish and other sources identify nails used in a crucifixion as amulets possessing magical properties (ref. above). It follows that the presence of two nails with slivers of accreted cedar wood containing trace remains of bone tissue, present in two different ossuaries in the tomb of Caiaphas, suggests that, although neglected, these rare artifacts were an important issue in the family of the high priest. In consequence of the full range of observations above we feel confident in concluding that 1) the nails that we sampled are the missing nails from the Caiaphas family tomb and 2) these nails were, very probably, used in a crucifixion.

Acknowledgements

We thank Dr. S. Freeman of the Volcani Institute of Agricultural Research, and Dr. R. Engesser of the Swiss Federal Institute for Forest, Snow and Landscape Research who helped in our efforts at identifying some of the fungal and bacterial morphologies. Professor R. A. Blanchette University of Minnesota examined some of the SEM micrographs and was able to provide tremendous assistance especially regarding the possible fungal species we have dealt with above. Dr. V. Uvarov assisted in the processing of some of the XRD analyses on nail samples carried out at the Center for Nanoscience and Nanotechnology at the Hebrew University. Special thanks go to Prof. A.R. Philpotts, University of Connecticut (ret.) for his constructive comments made to an earlier version of the present manuscript. Professor K. T. Kilty read and improved the manuscript's present format. Professor I. Herskovitz of the Medical Faculty Dept. of Anthropology Tel Aviv University introduced us to the nails, and in spite of the destructive process involved, very kindly permitted us to scrape off small amounts of material from both nails for study. Professor A. Frumkin, Dept. of Earth and Planetary Sciences, Hebrew University, and Dr. A. Ayalon of the Geological Survey of Israel made minor corrections in the $\delta^{18}O$ and $\delta^{13}C$ data table and offered suggestions regarding the interpretation of the values. Very special thanks go to Professor J. D. Tabor, previously chair of Religious Studies at the University of North Carolina, Charlotte and journalist and researcher S. Jacobovici, without their ideas and vision regarding certain contested archaeological finds linked to early Christianity in Jerusalem this project would be a non-starter. To you all and others we may have unintentionally neglected to mention, our deep gratitude.

Conflicts of Interest

The authors declare no conflicts of interest regarding the publication of this paper.

References

Bar-Matthews, M., & Ayalon, A. (2001). *Carbonate Cave Deposits (Speleothems) as Paleoclimate, Paleohydrological and Paleoseismic Indicators*. Report GSI/41/01.

Bar-Matthews, M., & Ayalon, A. (2004). Speleothems as Palaeoclimate Indicators, a Case Study from Soreq Cave Located in the Eastern Mediterranean Region, Israel. In R. W. Battarbee, F. Gasse, & C. E. Stickley (Eds.), *Past Climate Variability through Europe and Africa* (pp. 363-391). Dordrecht: Springer. https://doi.org/10.1007/978-1-4020-2121-3_18

Bastias, D. A., Johnson, L. J., & Card, S. D. (2019). Symbiotic Bacteria of Plant-Associated Fungi: Friends or Foes? *Current Opinion in Plant Biology, 56,* 1-8. https://doi.org/10.1016/j.pbi.2019.10.010

Blanchette, R. A., & Simpson, E. (1992). Soft Rot and Wood Pseudomorphs in an Ancient Coffin (700 BC) from Tumulus MM at Gordion, Turkey. *IAWA Bulletin n.s., 13,* 204-213. https://doi.org/10.1163/22941932-90001269

Casanova, P. L., Haderlain, S. B., & Kappler, A. (2010). Biomineralization of Lepidocrocite and Goethite by Nitrate-Reducing Fe(II)-Oxidizing Bacteria: Effect of pH, Bicarbonate, Phosphate, and Humic Acids. *Geochimica et Cosmochimica Acta, 74,* 3721-3734. https://doi.org/10.1016/j.gca.2010.03.037

Cumplido, J., Barron, V., & Torrent, J. (2000). Effect of Phosphate on the Formation of Nanophase Lepidocrocite from Fe (II) Sulfate. *Clays and Clay Minerals, 48,* 503-510. https://doi.org/10.1346/CCMN.2000.0480502

Fanning, S., & Mitchell, A. P. (2012). Fungal Biofilms. *PLOS Pathogens, 8,* e1002585. https://doi.org/10.1371/journal.ppat.1002585

Frumkin, A., Ford, D. C., & Schwarcz, H. P. (1999). Continental Oxygen Isotopic Record of the Last 170,000 Years in Jerusalem. *Quaternary Research, 51,* 317-327. https://doi.org/10.1006/qres.1998.2031

Greenhut, Z. (1992). Burial Cave of the Caiaphas Family. *Biblical Archaeological Review, 18,* 29-36.

Greenhut, Z. (2004). *Discovery of the Caiaphas Family Tomb*. Jerusalem Perspective Online, Jan. 1. http://www.jerusalemperspective.com

Hachlili, R., & Killebrew, A. (1983). *Was the Coin-on-Eye Custom a Jewish Burial Practice in the Second Temple Period*? BA 147-153. https://doi.org/10.2307/3209825

Jacobovici, S. (2014). *Biblical Conspiracies Series, Nails of the Cross, 2014*.

Kirschvink, J. L., Kobayashi-Kirschvink, A., & Woodford, B. J. (1992). Magnetite Biomineralization in the Human Brain. *Proceedings in the National Academy of Sciences* (Vol. 89, pp. 7683-7687). https://doi.org/10.1073/pnas.89.16.7683

Lema, K. A., Willis, B. L., & Bourne, D. G. (2012). Corals Form Characteristic Associations with Symbiotic Nitrogen-Fixing Bacteria. *Applied and Environmental Microbiology, 78,* 3136-3144. https://doi.org/10.1128/AEM.07800-11

Lowenstam, H. A. (1981). Minerals Formed by Organisms. *Science, 211,* 1126-1131. https://doi.org/10.1126/science.7008198

Reuven, P. (2013). Wooden Beams from Herod's Temple Mount: Do They Still Exist? *Bibllical Archaeology Review, 39,* 40-47.

Rahmani, L. (1961). Jewish Rock-Cut Tombs in Jerusalem. *Atiqot, 3,* 93-120.

Ross, J. G., & Wang, C. (1982). Lepidocrocite in a Calcareous, Well-Drained Soil. *Clays and Clay Minerals, 30,* 394-396. https://doi.org/10.1346/CCMN.1982.0300511

Schieber, J., & Glamoclija, M. (2007). Microbial Mats Built by Iron Bacteria: A Modern Example from Southern Indiana. In J. Schieber et al. (Eds.), *Atlas of Microbial Mat Features Preserved within the Clastic Rock Record* (pp. 233-244). Amsterdam: Elsevier.

Shimron, A. E., Shirav, M., Kilty, K. T., Halicz, L., Pedersen, R. B., & Furnes, H. (2020). The Geochemistry of Intrusive Sediment Sampled from the 1st Century CE Inscribed Ossuaries of James and the Talpiot Tomb, Jerusalem. *Archaeological Discovery, 8,* 92-115.

Schwertmann, U., & Taylor, R. M. (1972). The Transformation of Lepidocrocite to Goethite. *Clays and Clay Minerals, 20,* 151-158. https://doi.org/10.1346/CCMN.1972.0200306

Tabor, J. D., & Jacobovici, S. (2012). *The Jesus Discovery*. New York: Simon and Schuster.

Toynbee, J. M. C. (1971). *Death and Burial in the Roman World*. London: Johns Hopkins University Press.

Trueman, C. et al. (2004). Mineralogical and Compositional Changes in Bones Exposed on Soil Surfaces in Amboseli National Park, Kenya: Diagenetic Mechanisms and the Role of Sediment Pore Fluids. *Journal of Archaeological Science, 31,* 721-739. https://doi.org/10.1016/j.jas.2003.11.003

Tsaferis, V. (1985). Crucifixion—The Archaeological Evidence. *Biblical Archaeological Review, 11,* 44-53.

Vaks, A. et al. (2003). Paleoclimate Reconstruction Based on the Timing of Speleothem Growth and Oxygen and Carbon Isotope Composition in a Cave Located in the Rain Shadow in Israel. *Quaternary Research, 59,* 182-193. https://doi.org/10.1016/S0033-5894(03)00013-9

Archaeological Discovery, 2020, 8, 288-294
https://www.scirp.org/journal/ad
ISSN Online: 2331-1967
ISSN Print: 2331-1959

The Ancient Legend about Surt and the Novel Concept of Methane Venting Tectonics (MTV)

Nils-Axel Mörner[1], Ciara Duffy[2]

[1]Paleogeophysics & Geodynamics, Stockholm, Sweden
[2]Point Cook, Victoria, Australia
Email: morner@pog.nu

How to cite this paper: Mörner, N.-A., & Duffy, C. (2020). The Ancient Legend about Surt and the Novel Concept of Methane Venting Tectonics (MTV). *Archaeological Discovery, 8,* 288-294.
https://doi.org/10.4236/ad.2020.83016

Received: June 24, 2020
Accepted: July 13, 2020
Published: July 16, 2020

Abstract

We merge the concept of methane venting tectonics and the old legend about Surt, the giant of fire, living in the underground and having a burning sword. Due to the tumbling and collisions between blocks thrown up in the air by the explosive methane venting forces, ignition is likely to have set the methane on fire; i.e. huge burning columns of tens to hundreds of metres height. Such events occurred in east-central Sweden at about 3000 BP. The Bronze Age people are likely to have understood it as Surt pushing up his sword of fire from the underground. The legends of Surt, the Fenris Wolf, the Midgårds Serpent and the Ragnarök apocalypse, all seem to owe their origins to the violent geodynamic activity along the east-central part of Sweden at about 3000 BP. We may therefore speak about an ancient "Svenonian mythology", which precedes the Norse mythology of the Edda by about 2000 years.

Keywords

Nordic Mythology, Surt the Giant of Fire in the Underground, Methane Venting Tectonics, The Fenris Wolf, Ground Shaking, The Ragnarök Apocalypse, The 3000 BP Events

1. Introduction

Explosive methane venting in the crystalline bedrock was first reported by Mörner (2003) and further discussed in subsequent papers (Mörner, 2011, 2013) Because the explosive methane venting leads to extensive bedrock deformation, the process became known as Methane Venting Tectonics (abbreviated MVT). The first general presentation of the concept of Methane Venting Tectonics came in 2017 (Mörner, 2017a, 2017b). So far, the work of the first author (NAM).

The second author (CD) happened to come across the presentation of the

MVT concept (Mörner, 2017a), and made an intuitive association with the action of the giant Surt in Nordic mythology. This led to the present study: the merging of the two concepts.

2. Methane Venting Tectonics

Methane can occur in two stages in nature; as methane gas and as methane hydrate (also termed methane ice because it is a solid). The stage is defined by temperature and pressure, and the boundary between the two stages is a phase boundary. The volumetric change from hydrate to gas is as 1:168 (room temperature conditions), which implies that a sudden change from methane hydrate in the subsurface to methane gas may generate explosive venting.

The conditions for accumulation of methane hydrate in crystalline bedrock in Sweden are: 1) methane degassing (measured in drill-holes, (Mörner, 2011, 2017a) and observed as carbonate precipitates in the varved clay (Mörner, 2003, 2017b), 2) pre-existing fractures and voids in the rock (well recorded), 3) presence of water (in the fractures and voids), 4) a geothermal gradient allowing the formation of methane hydrate (Figure 1a in Mörner, 2017a) and 5) major changes in temperature and pressure in association with the waxing and waning of ice caps of the Quaternary Ice Ages (Figure 1b in Mörner, 2017a). The sudden transformation from solid methane hydrate (ice) to methane gas at a very much increased volume forcing the gas to vent can be triggered by long-term changes in temperature and pressure (glacial isostatic uplift) or by sudden pressure impulses from earthquakes Mörner, 2003; Figure 3 in Mörner, 2017a).

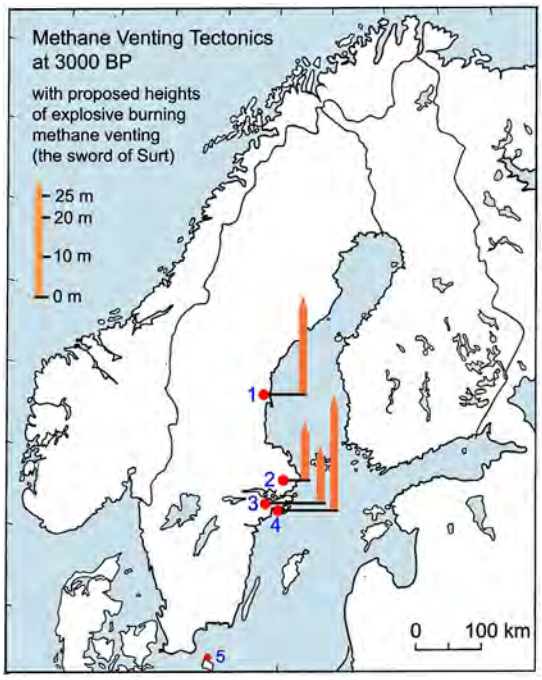

Figure 1. Site of methane venting tectonics at about 3000 BP (i.e. in the middle of the Bronze Age) with minimum estimate of the height of the corresponding venting gas columns. Heights of the flames may be up to 10 times higher, however.

Mörner (p. 106 in Mörner, 2003, Figure 7 in Mörner, 2017a, Mörner, 2016a) presented a model of methane venting tectonics, which illustrate the underground phase transition and the explosive gas venting forcing huge bedrock blocks to be thrown up into a 20 - 25 m high cone of detached blocks. There are also cases when the old glacially polished bedrock surface has been fractured into loose dislocated blocks moved or thrown out of position due to ground shaking and/or methane venting tectonics.

Methane venting tectonics (MVT) occurred frequently during the deglaciation period when isostatic uplift changed the underground pressure and when paleoseismic activity was strong both in magnitude and frequency. Ten sites are described from Sweden and two from Finland from the deglacial time (Mörner, 2017a, 2017b). Four additional sites date from about 3000 BP (**Figure 1**), however, and will be discussed below.

Site 1 (Skålboberget) refers to a 20 m high cone of angular block torn out of the original bedrock position (Mörner, 2003, 2017a, 2017b). The largest blocks (on the order of hundreds of tons) are at the top of the cone. The venting of methane is recorded in the incorporation of dead carbon in the C14-dates, and ^{13}C values indicating anaerobic oxidation of methane and iron sulphide reduction (Mörner, 2017a). The deformation generated a tsunami wave of a height of about 12 m (Mörner, 2016b).

Site 2 (Tolan in Upplands-Väsby) refers to a heavily deformed glacially polished surface in glacially stoss-side position. Huge bedrock blocks were torn loose and thrown up to 50 m away, landing on former beach material from the time of emergence at about 5000 BP. The area seems struck both by seismic ground shaking and methane venting tectonics. Besides, a high-amplitude tsunami wave invaded a nearby lake basin at about 3000 BP. When this site was investigated in 2018-2019, it occurred to one of us (NAM) that the blocks thrown 40 - 50 m away, must have generated sparks when landing on other blocks, and those sparks might have ignited the methane gas. If so, the burning methane would have taken the form of light columns coming out of the ground. So, when the second author (CR) proposed the action of Surt, things fell together that the burning methane column might be the burning sword of Surt. Many stones at this site are scorched by fire. But it is impossible to know if this originates from burning methane venting or from later action by people.

Site 3 (Marviken) refers to a fracture valley where faulting, earth sliding, methane venting and a tsunami were recorded and dated at about 3000 BP (Mörner, 2003, 2009, 2017a; Mörner & Strandberg, 2009). Methane venting tectonics was documented at 3 separate points (Figure 5 in Mörner, 2017a). The valley sides are full of fracture marks and angular blocks (even a Bronze Age grave mound was deformed). Therefore, it seems quite relevant that the origin of the word "Marviken" originates from "*mardher*", an ancient name for "fractured" going back to the late Bronze Age (Mörner & Strandberg, 2009).

Site 4 (Kvarnberget) refers to a 25 m high cone of huge angular blocks with

gigantic blocks at the top (Mörner, 2017a, 2017b; Mörner & Sjöberg, 2011). The shape, size and block organization was found (Figure 6 in Mörner, 2017a) to indicate "*very strong venting forces concentrated to a venting tube* (*or chimney*)". The deformation is linked to a huge delta at +15 m (p. 25 in Mörner, 2017b), which implies an age of about 3000 BP.

3. Surt: The Giant of Fire

In the Nordic mythology, *Surt* was a giant and the ruler of fire (**Figure 2**). He lived in the underground together with the other giants of fire. He had a sword of fire, shining stronger than the Sun and being superior to all other weapons. At the doomsday *Ragnarök*, Surt lead the giants of fire against the gods in Asgård.

The Sun and the Moon were devoured by wolves, the *Fenris Wolf* escaped from his chains within the mountains, and the giant *Midgård Serpent* appeared in the sea. The stars fell, the ground trembled violently from earthquakes and the bedrock fractured into pieces—this was Ragnarök, the end of the World.

In the battle between the Gods and the giants and monsters, Surt swings his sword that shines and sparks long distances.

According to Simek (2007), this legend is ancient, but became included in the Norse mythology, when Iceland was settled by Norwegian Vikings and they experienced volcanism for the first time. Therefore, not until the discovery of explosive methane venting tectonics in Sweden (Mörner, 2003) was there any reasons to propose the interpretation here presented. The high paleoseismic activity recorded in the Late Holocene (Mörner, 2003, 2009), however, lead to the proposal that the legend of the Fenris Wolf, in fact, originated from about 3000 BP (Mörner, 2007).

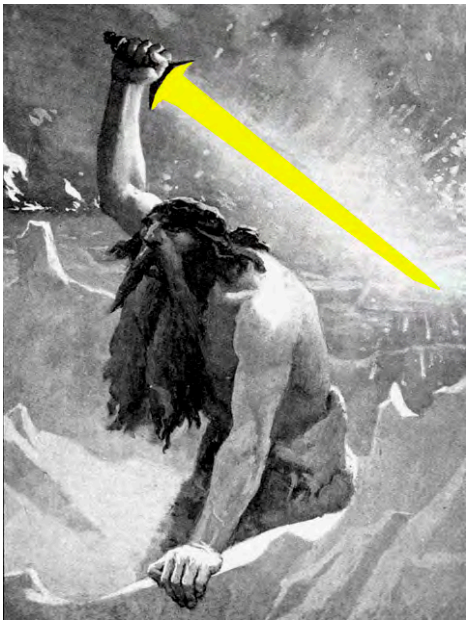

Figure 2. The giant Surt of the underground with his gigantic sword of fire (modified from classical illustration by J. C. Dollman).

4. Merging the Concept of Methane Venting Tectonics and the Legend of Surt

The concept of methane venting tectonics is young; proposed in 2003 (Mörner, 2003) and presented as operating process in 2017 (Mörner, 2017a). The legend of Surt is old. According to the Icelandic Edda (Sturlasson, 1220) it is a part of the Asa Creed held by the Vikings.

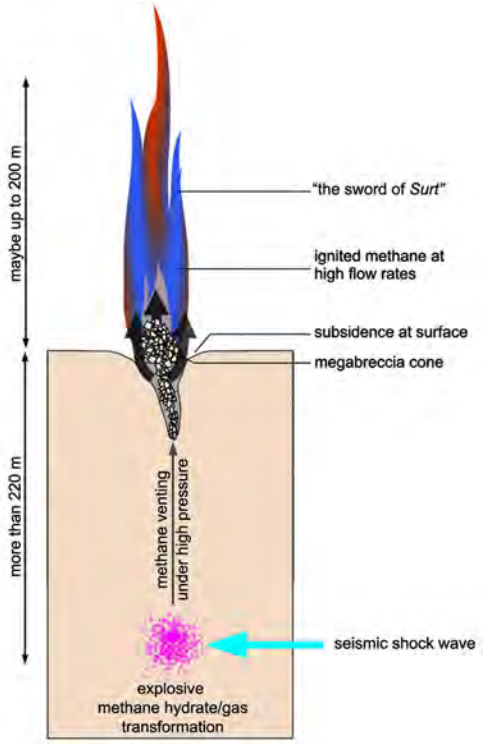

Figure 3. Schematic illustration of the concept of methane venting tectonics (Sites 1 - 4), and the proposed burning flames of methane gas reaching high up in the air, by the locals understood in terms of Surt pushing up his sword of fire from the underground.

According to others (Simek, 2007; Mörner, 2007; Scott Littleton, 1964) certain parts of the proposed Asa Creed may, in fact, be much older. The legend about the Fenris Wolf (shaking the mountains so that they fracture and collapse) has been ascribed to the violent seismo-tectonics recorded in the Bronze Age (Mörner, 2007). The Midgård Serpent occurs on a rock-carving from the Bronze Age (point 5 in **Figure 1**) and must hence have a similar age (Mörner, 2020). The legend about the end of the World (Ragnarök) seems to fit perfectly well with the violent seismo-tectonics and methane venting tectonics observed at about 3000 BP (Mörner, 2020). We now propose that the legend of Surt should have a similar age and origin.

Surt was the leading fire-giant living in the underground. His sword was made of fire. It was huge and frightening, and shining over long distances.

The methane venting at methane venting tectonics events implied "*very*

strong venting forces concentrated to a venting tube (*or chimney*)". When burning (due to stone-to-stone sparking), the columns (tubes or chimneys) must have exceeded the cones high up in the sky like gigantic swords from the underground; a magnificent view but also a most frightening view (**Figure 3**). The interpretation of a giant pushing up his burning sword from the underground seems very close and logical. This is our proposal, and it implies that even the legend of Surt emanates from actual earth processes dating back to about 3000 BP.

5. Conclusion

The legend of the giant Surt with his burning sword has an origin far older than the Norse mythology of Viking time. We demonstrate that it originates from the mid Bronze Age when violent methane venting tectonics occurred in east-central Sweden at about 3000 BP.

When the huge pillar of explosive methane venting in flames emerged out of the ground, it was understood in terms of a giant (which of course must be Surt) sticking up his burning sword from the underground.

This means that the legend of Surt becomes 2000 years older than generally assumed. But he is not alone; the Fenris Wolf (Mörner, 2007), the Midgård Serpent (Mörner, 2020) and the idea of Ragnarök (Mörner, 2007, 2020) are already there.

Even if there might be similarities in old Indo-European mythology, what we are talking about all go back to local people's personal observations in the field of events that occurred at 3000 BP in east-central Sweden, or what we generally call "Svealand" (termed "Svenonian" by Tacitus, AD 79, and "Svitjod" in Icelandic sagas).

Therefore, it seems, we have to start speaking about "*the Svenonian Mythology*" originating in the violent geodynamic processes in the mid Bronze Age at about 3000 BP.

By merging the legend of Surt with the concept of methane venting tectonics, the idea that the tumbling of stones and block at the explosive venting may have ignited the methane gas has become strongly supported; as illustrated in **Figure 3**.

Acknowledgements

We are indebted to Brendan Duffy for insisting on high flames into the sky as illustrated in **Figure 3**, the upper part of which was drawn by him. We acknowledge constructive linguistic check by Dr. Pamela Matlack-Klein. We declare no competing interest and no funding to declare.

Conflicts of Interest

The authors declare no conflicts of interest regarding the publication of this paper.

References

Mörner, N.-A. (2003). Paleoseismicity of Sweden—A Novel Paradigm. *16th International*

INQUA Congress, Reno, Nevada, 1-320.

Mörner, N.-A. (2007). The Fenris Wolf in the Nordic Asa Creed in the Light of Paleoseismics. *Geological Society, London, Special Publications, 273,* 117-119. https://doi.org/10.1144/GSL.SP.2007.273.01.10

Mörner, N.-A. (2009). Late Holocene Earthquake Geology in Sweden. *Geological Society, London, Special Publications, 316,* 179-188. https://doi.org/10.1144/SP316.11

Mörner, N.-A. (2011). Plaeoseismology: The Application of Multiple Parameters in Four Case Studies in Sweden. *Quaternary International, 242,* 65-75. https://doi.org/10.1016/j.quaint.2011.03.054

Mörner, N.-A. (2013). Patterns in Seismology and Palaeoseismology, and Their Application in Long-Term Hazard Assessments—The Swedish Case in View of Nuclear Waste Management. *Pattern Recognition in Physics, 1,* 75-89. https://doi.org/10.5194/prp-1-75-2013

Mörner, N.-A. (2016a). Methane Venting and Methane Venting Tectonics. *13th International Conference on Gas in Marine Sediments (GIMS13)*, Tromsø, 19-22 September 2016, Abstracts. https://www.researchgate.net/publication/308306076

Mörner, N.-A. (2016b). Tsunamis in Sweden: Occurrence and Characteristics. In M. Mokhtari (Ed.), *Tsunami* (Chap. 6, pp. 115-133). London: InTech. https://doi.org/10.5772/63956

Mörner, N.-A. (2017a). Methane Hydrate in Crystalline Bedrock and Explosive Methane Venting Tectonics. *Earth-Science Reviews, 169,* 202-212. https://doi.org/10.1016/j.earscirev.2017.05.003

Mörner, N.-A. (2017b). Methane Hydrate in Crystalline Bedrock and Explosive Methane Venting Tectonics. *Earth-Science Reviews, 169,* 202-212. https://doi.org/10.1016/j.earscirev.2017.05.003

Mörner, N.-A. (2020). The Kaali Impact, Coincidental Deformations and Tsunamis, and Ancient Legends. *10th International INQUA Meeting on Paleoseismology, Active Tectonics and Archeoseismology (PATA)*, Hornitos, Chile, 8-12 November 2020, Extended Abstracts, 1-4. (In press)

Mörner, N.-A., & Sjöberg, R. (2011). Excursion Guide. *The 2nd International Conference on Granite Caves*, Sweden, June 2011, Speleo Publication 12, 28 p.

Mörner, N.-A., & Strandberg, S. (2009). Marviken. Geologiskt baserad namntolkning. Saga och Sed, Kungl. Gustav Adolfs Akademiens Årsbok 2009, 179-184.

Scott Littleton, C. (1964). The Comparative Indo-European Mythology of George Dumézil. *Journal of Folklore Institute, 1,* 147-166. https://doi.org/10.2307/3813900

Simek, R. (2007). *Dictionary of Northern Mythology*. Woodbridge, England: Boydell & Brewer.

Sturlasson, S. (1220). Den Prosaiska Eddan (Snorre's Edda): Codex Upsaliensis, DG 11. Den Poetiska Eddan. Codex Regius, Det Kongl. Bibl. Köpenhavn.

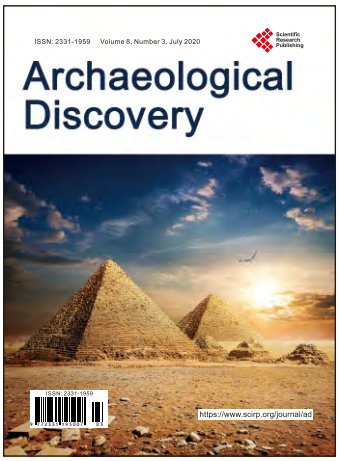

Call for Papers

Archaeological Discovery

ISSN Print: 2331-1959 **ISSN Online: 2331-1967**

https://www.scirp.org/journal/ad

Archaeological Discovery (AD) is an international journal dedicated to the latest advancement in the study of Archaeology. The goal of this journal is to provide a platform for scientists and academicians all over the world to promote, share, and discuss various new issues and developments in different areas of Archaeological studies.

Subject Coverage

All manuscripts must be prepared in English, and are subject to a rigorous and fair peer-review process. Accepted papers will immediately appear online followed by printed hard copy. The journal publishes original papers covering a wide range of fields but not limited to the following:

- Aerial Archaeology
- Archaeological Method and Theory
- Archaeological Science
- Archaeometry
- Art Archaeology
- Environmental Archaeology
- Ethnoarchaeology
- Experimental Archaeology
- Field Archaeology
- Geoarchaeology
- Historical Archaeology
- Island and Coastal Archaeology
- Lithic Studies
- Maritime Archaeology
- Prehistoric Archaeology
- Religious Archaeology
- Social Archaeology
- Underwater Archaeology
- World Archaeology
- Zooarchaeology

We are also interested in: 1) Short reports — 2-5 page papers in which an author can either present an idea with a theoretical background but has not yet completed the research needed for a complete paper, or preliminary data; 2) Book reviews — Comments and critiques, special peer-reviewed issue for colloquia, symposia, workshops.

Website and E-Mail

https://www.scirp.org/journal/ad **E-mail: ad@scirp.org**

What is SCIRP?

Scientific Research Publishing (SCIRP) is one of the largest Open Access journal publishers. It is currently publishing more than 200 open access, online, peer-reviewed journals covering a wide range of academic disciplines. SCIRP serves the worldwide academic communities and contributes to the progress and application of science with its publication.

What is Open Access?

All original research papers published by SCIRP are made freely and permanently accessible online immediately upon publication. To be able to provide open access journals, SCIRP defrays operation costs from authors and subscription charges only for its printed version. Open access publishing allows an immediate, worldwide, barrier-free, open access to the full text of research papers, which is in the best interests of the scientific community.

- High visibility for maximum global exposure with open access publishing model
- Rigorous peer review of research papers
- Prompt faster publication with less cost
- Guaranteed targeted, multidisciplinary audience

Scientific Research Publishing

Website: https://www.scirp.org

Subscription: sub@scirp.org

Advertisement: service@scirp.org